In Vivo MRI-Based Three-Dimensional Fluid-Structure Interaction Models and Mechanical Image Analysis for Human Carotid Atherosclerotic Plaques

A Dissertation

Submitted to the Faculty

of the

WORCESTER POLYTECHNIC INSTITUTE

in Partial Fulfillment of the Requirements of the

Degree of Doctor of Philosophy

by

Xueying Huang
May 2009

Approved by

Professor Dalin Tang, Dissertation Advisor, Committee Chair
WPI Department of Mathematical Sciences

Professor Zhikun Hou, Committee Member
WPI Department of Mechanical Engineering

Professor Mayer Humi, Committee Member
WPI Department of Mathematical Sciences

Professor Roger Y. Lui, Committee Member
WPI Department of Mathematical Sciences

Professor Homer F. Walker, Committee Member
WPI Department of Mathematical Sciences

Abstract

Introduction. Atherosclerotic plaque rupture may occur without warning leading to severe clinical events such as heart attack and stroke. The mechanisms causing plaque rupture are not well understood. It is hypothesized that mechanical forces may play an important role in the plaque rupture process and that image-based computational mechanical analysis may provide useful information for more accurate plaque vulnerability assessment. The objectives of this dissertation are: a) develop *in vivo* magnetic resonance imaging (MRI)-based 3D computational models with fluid-structure Interactions (FSI) for human atherosclerotic carotid plaques; b) perform mechanical analysis using 3D FSI models to identify critical stress/strain conditions which may be used for possible plaque rupture predictions.

Data, Model, and Methods. Histological, *ex vivo*/ *in vivo* MRI data of human carotid plaques were provided by the University of Washington Medical School and Washington University Medical School. Blood flow was assumed to be laminar, Newtonian, viscous and incompressible. The Navier-Stokes equations with arbitrary Lagrangian-Eulerian (ALE) formulation were used as the governing equations for the flow model. The vessel and plaque components were assumed to be hyperelastic, isotropic, nearly-incompressible and homogeneous. The nonlinear Mooney-Rivlin model was used to describe the nonlinear properties of the materials with parameter values chosen to match available experimental data. The fully-coupled FSI models were solved by a commercial finite element software ADINA to obtain full 3D flow and stress/strain distributions for analysis. Validation of the computational models and Adina software were provided by comparing computational solutions with analytic solutions and experimental data.

Several novel methods were introduced to address some fundamental issues for construction of *in vivo* MRI-based 3D FSI models: a) an automated MRI segmentation technique using a

Bayes theorem with normal probability distribution was implemented to obtain plaque geometry with enclosed components; b) a pre-shrink process was introduced to shrink the *in vivo* MRI geometry to obtain the no-load shape of the plaque; c) a Volume Component-Fitting Method was introduced to generate a 3D computational mesh for the plaque model with deformable complex geometry, FSI and inclusions; d) a method using MRI data obtained under *in vitro* pressurized conditions was introduced to determine vessel material properties.

Results. The effects of material properties on flow and wall stress/strain behaviors were evaluated. The results indicate that a 100% stiffness increase may decrease maximal values of maximum principal stress (Stress-P_1) and maximum principal strain (Strain-P_1) by about 20% and 40%, respectively; flow Maximum-Shear-Stress (FMSS) and flow velocity did not show noticeable changes. By comparing *ex vivo* and *in vivo* data of 10 plaque samples, the average axial (25%) and inner circumferential (7.9%) shrinkages of the plaques between loaded and unloaded state were obtained. Effects of the shrink-stretch process on plaque stress/strain distributions were demonstrated based on six adjusted 3D FSI models with different shrinkages. Stress-P_1 and Strain-P_1 increased 349.8% and 249% respectively with 33% axial stretch. The effects of a lipid-rich necrotic core and fibrous cap thickness on structure/flow behaviors were investigated. The mean values of wall Stress-P_1 and Strain-P_1 from lipid nodes from a ruptured plaque were significantly higher than those from a non-ruptured plaque (112.3 kPa, 0.235 & 80.1 kPa, 0.185), which was 40.2% and 26.8% higher, respectively ($p<0.001$). High stress/strain concentrations were found at the thin fibrous cap regions. These results indicate that high stress concentrations and thin fibrous cap thickness might be critical indicators for plaque vulnerability.

Conclusion. *In vivo* image-based 3D FSI models and mechanical image analysis may have the potential to provide quantitative risk indicators for plaque vulnerability assessment.

Acknowledgements

I would like to express my deepest gratitude to Professor Dalin Tang, my advisor, for his constant help, encouragement, guidance, and thoughtful advice during my study at Worcester Polytechnic Institute. Without his help and support, this dissertation would never have been completed.

I sincerely thank the members of my dissertation committee: Professors Zhikun Hou, Mayer Humi, Roger Y. Lui, Homer F. Walker, and Dalin Tang, for their valuable guidance and support.

My sincere appreciation is extended to my *ex*-advisor and friend, Professor Chun Yang (Beijing Normal University, P.R. China), who is the first professor to introduce me to such an interesting and challenging field, for her professional and personal advice and help. I would like to thank Professor Tang's collaborators who provided data for this research. Histological, *ex vivo*/*in vivo* MRI data of human carotid plaques were provided by Professor Chun Yuan's group (Chun Yuan, Thomas S. Hatsukami, Gador Canton, Li Dong, Fei Liu, Marina Ferguson) from University of Washington Medical School and Professors Pamela Woodard and Jie Zheng's group (Pamela Woodard, Jie Zheng, Dongsi Lu, Gregorio A. Sicard) from Washington University Medical School. *In vitro* experimental data were provided by Professor David Ku (Georgia Institute of Technology) and Professor Shunichi Kobayashi (Shinshu University, Japan). Dr. Zhongzhao Teng provided much help in model construction and automation techniques. My appreciation also goes to many professors, staff, and my fellow graduate students in the Mathematical Sciences Department for their help and friendship.

Finally, I would like to give a special thank-you to my parents for their constant love, understanding and support.

Table of Contents

Part I. Introduction

Part II. MRI Data Preparation and 3D Geometry Reconstruction

Part III. FSI Models, Solution Methods and Validations

Part IV. Results

Part V. Discussion and Conclusion

List of Figures

List of Tables

List of Diagrams

Part I.

Introduction

1. Problem Statement and Objectives

1.1 Problem Statement and Objectives

Cardiovascular disease (CVD) is the leading cause of death in the United States and is becoming the leading cause of death worldwide [1]. Nearly 2400 Americans die of CVD each day, an average of 1 death every 37 seconds [1]. Atherosclerotic plaque rupture is the primary cause of heart attack and stroke and may occur without any warning. Present diagnosis is based on the morphological information from medical images such as magnetic resonance imaging (MRI), computer tomography (CT), ultrasound, *etc*. However, current screening and diagnostic methods are insufficient to identify the victims before the event occurs.

Atherosclerotic plaque rupture is a complex procedure which involves many factors: plaque composition and morphological conditions (thin plaque cap, large lipid core, *etc.*), biomechanical forces, localization, vessel remodelling, blood conditions (cholesterol, sugar, *etc*.), chemical environment (lipid-lowering drugs to reduce rupture risk), lumen surface (inflammation) and stenoses, and structural composition [15, 22-24, 26, 28]. It has been hypothesized that mechanical forces play an important role in the plaque rupture process and should be taken into consideration for plaque vulnerability assessment. The objectives of this dissertation are: a) develop *in vivo* magnetic resonance imaging (MRI)-based 3D computational models with fluid-structure interactions (FSI) for human atherosclerotic carotid plaques; b) perform mechanical analysis using 3D FSI models to identify critical stress/strain conditions which may be used for possible plaque rupture predictions. Computational models will be combined with Magnetic Resonance Imaging (MRI) and pathological analysis to analyze vulnerable carotid atherosclerotic plaques, to quantify the effects of material properties and shrink-stretch process on plaque stress/strain distributions, and to quantify critical blood flow and plaque stress/strain conditions under which plaque rupture is likely to occur. Specific aims to achieve these objectives are given in next section.

1.2 Specific Aims

Aim #1: Obtain accurate human carotid atherosclerotic plaque morphology, material properties and shrinkage data which are needed for computational model construction. A segmentation method using Bayes theorem with normal probability distribution will be introduced to quantify plaque morphology. MR imaging for plaque samples under pressurized conditions will be used to determine effective vessel/plaque material properties as well as to provide validation for computational models. *In vivo* and *ex vivo* MRI data will be compared to quantify human carotid artery shrinkage between *in vivo* and *ex vivo* state. The MRI data in this dissertation were provided by Dr. Yuan's group at Washington University and Dr. Zheng's group at the University of Washington.

Aim #2: Develop 3D *in vivo* MRI-based computational models with fluid-structure interactions (FSI) to perform plaque mechanical analysis and assessment. The computational model with fluid-structure interactions will be constructed based on patient-specific *in vivo* MR images. A shrink-stretch process for *in vivo* MRI-based human carotid artery models will be introduced to address the computational starting state issue. The *in vivo* plaque geometry will be shrunk with obtained shrinkage data to get the geometry at no-load condition, which will be used as the starting geometry of the model. Axial stretch and pressure conditions will then be imposed to obtain the *in vivo* plaque morphology with proper initial conditions.

Aim #3: Perform mechanical analysis for plaque vulnerability assessment using the 3D FSI models developed in Aim 2. Using a series of 3D FSI models developed in Aim #2 based on patient-specific atherosclerotic plaque data, mechanical analysis will be performed to identify critical stress/strain and flow conditions which may be related to plaque venerability. Correlations between critical plaque stress/strain conditions (model output variables which include flow and plaque stress/strain variables) and vessel mechanical properties, shrink-stretch procedure, plaque morphology, and composition, will be identified.

The inter-connections of the three aims are described by the following flowchart:

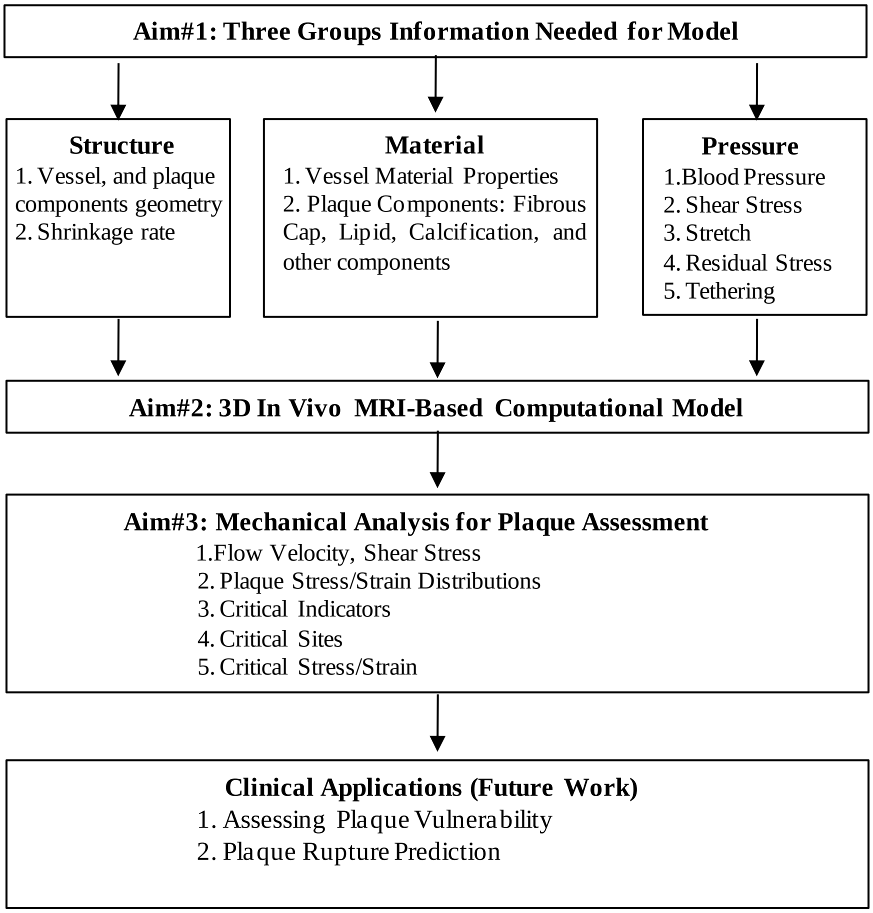

Diagram1.1 A flowchart showing the organization of this dissertation.

1.3 Outline of the Dissertation

The dissertation is organized into the following four parts:

Part I. Introduction. In this part, we begin by describing the problem and stating the objectives and specific aims. A review of the background of cardiovascular disease (CVD) was given which covers carotid atherosclerosis, the progression of plaque, and current non-invasive imaging methods. A literature review for the field of vulnerable atherosclerotic carotid plaque analysis and image-based computational modeling was provided.

Part II. MRI Data Preparation and 3D Geometry Reconstruction. Chapter 3 focuses on multi-contrast MRI image segmentation to obtain plaque morphology data. An automated segmentation method using Bayes theorem with normal probability distribution is introduced in this chapter. Chapter 4 presents the details of 3D geometry reconstruction and mesh generation process which was performed in ADINA computing environment. The geometry structure consists of points, lines, surfaces and volumes. The key here is the proper division of each physical object into many component-fitting computational volumes so that the proper mesh can be generated. This step has a strong influence on the element shape and convergence of the model.

Part III. FSI Models, Solution Methods and Validations. In Chapter 5, we introduce the 3D FSI model for carotid atherosclerotic plaques which includes solid models for the arterial material and the plaque components and fluid models for the blood flow through the artery. The solution method is presented in Chapter 6. In Chapter 7, validation for the computational models and ADINA software were provided by comparing the numerical results with analytic solution and experimental data.

Part IV. Results. In Chapter 8, results are presented for human carotid artery vessel material properties determined using MRI images obtained under in vitro pressurized conditions and least squares approximation method. Effects of material properties on flow and wall stress/strain behaviors were quantified using 3D MRI-based FSI models. Chapter 9 is dedicated to quantifying human carotid artery shrinkage between *in vivo* and *ex vivo* states using patient-specific *ex vivo*/*in vivo* MRI images and demonstrating the effects of shrink-stretch process with different axial/radial shrinkage on critical flow and plaque stress/strain conditions. In Chapter 10, the correlations between critical plaque stress/strain conditions and plaque composition and fibrous cap thickness were identified.

Part V. Discussions and Conclusions. Discussions and conclusions are given in Chapters 11&12.

2. Background and Review

2.1 Cardiovascular Disease (CVD)

Cardiovascular disease (CVD) is the first leading cause of death in the United States, accounting for more than 35% of all deaths, or 1 of every 2.8 deaths in the United States. Nearly 2400 Americans die of CVD each day, an average of 1 death every 37 seconds [1]. A large number of victims of coronary heart disease, which accounts for the majority of CVD, who are apparently healthy die suddenly without prior symptoms.

2.2 Carotid Atherosclerosis

The common carotid artery (CCA) is an artery that supplies the head and neck with oxygenated blood; it splits into two branches: the internal carotid artery (ICA), which provides oxygen-rich blood to the brain, and the external carotid arteries (ECA), which brings blood to the face (Fig. 2.1).

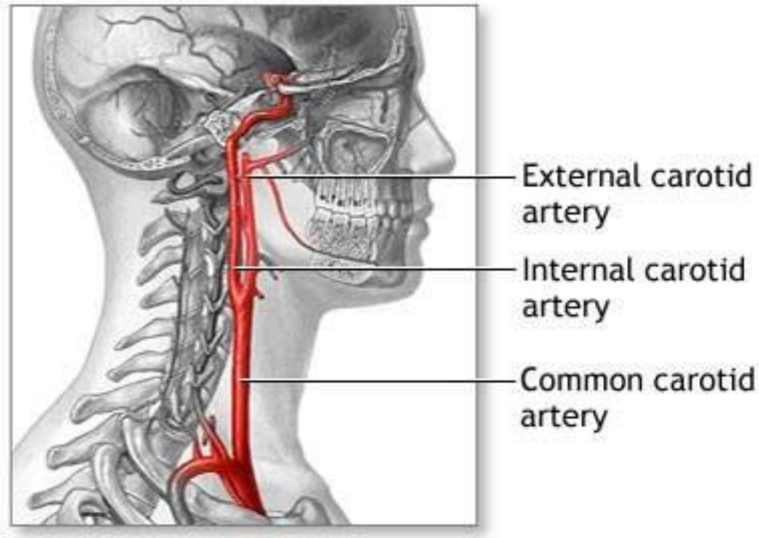

Figure 2.1. Anatomy of the carotid artery. There are four carotid arteries, with a pair located on each side of the neck. This includes the right- and left-internal carotid arteries (ICA), and the right- and left-external carotid arteries (ECA) [50].

Atherosclerosis is a general term for the thickening and hardening of arteries. The atherosclerotic plaque in the ICA may lead to narrowing, stiffening, and irregularity of the artery's lumen, preventing proper blood flow to the brain [2].

The carotid arteries are normally smooth and unobstructed on the inside, but as age increases, a fatty substance, cholesterol, cellular waste products, calcium and fibrin (a clotting material in the blood) can build up in the inner lining of an artery (Fig. 2.2 (b)). The build-up is called plaque and may progress over a long period of time (30-50 years or longer). At the initialization phase, the plaques are small and stable. When the plaque progression process continues, the carotid arteries may become narrowed. The sequence of events leading to plaque formation is very complex and probably involves many factors including mechanical factors, the chemical environment, and the interactions of several processes. The plaque may develop into an unstable plaque such as a plaque consisting of a large fatty lipid or a lipid core covered by a thin fibrous cap (Fig. 2.2 (d)). The focuses of our research are mechanical analysis and rupture risk (vulnerability) assessment for advanced plaques.

(a) Normal artery (b) A plaque builds up.

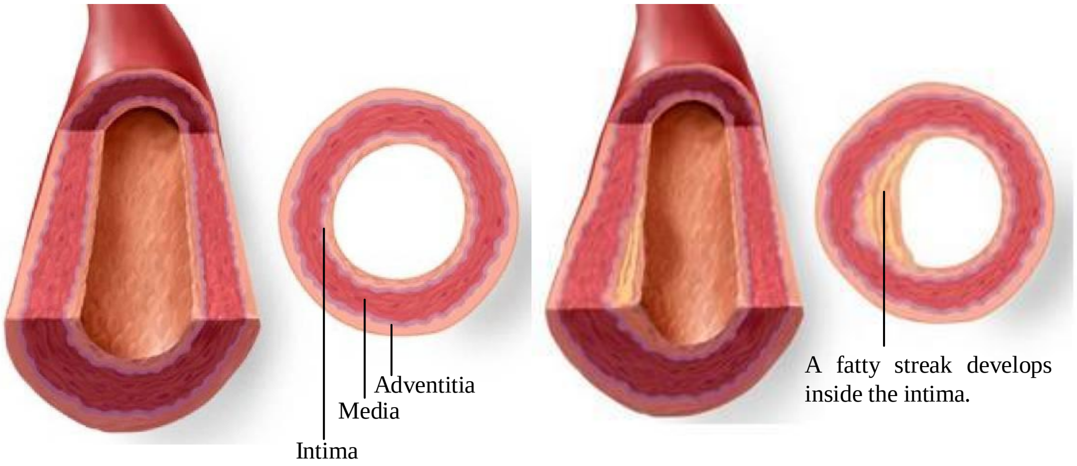

(c) A plaque develops. (d) Comparisons of unstable and stable plaque

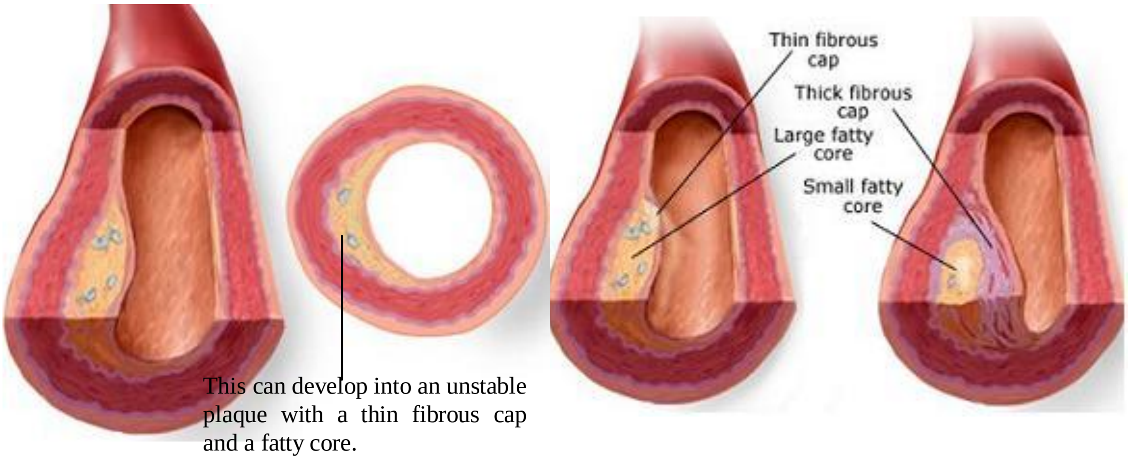

Figure 2.2. Diagrams showing atherosclerosis and atherosclerosis plaque. (a) normal artery showing three distinct layers of blood vessel; (b) the plaque builds up in the inner lining of the artery; (c) the plaque can develop into an unstable plaque with a thin fibrous cap and fatty core; (d) comparisons of stable and unstable plaques, the unstable plaque can evolve into an unstable plaque with a thin fibrous cap (left) and fatty core or a stable plaque with a thick fibrous cap (right) [2].

2.3 Vulnerable Plaques

Atherosclerotic plaques may rupture (Fig. 2.3) without warning and cause acute cardiovascular syndromes such as a heart attack or stroke [49].

(a) An unstable plaque.

(b) Plaque rupture occurs.

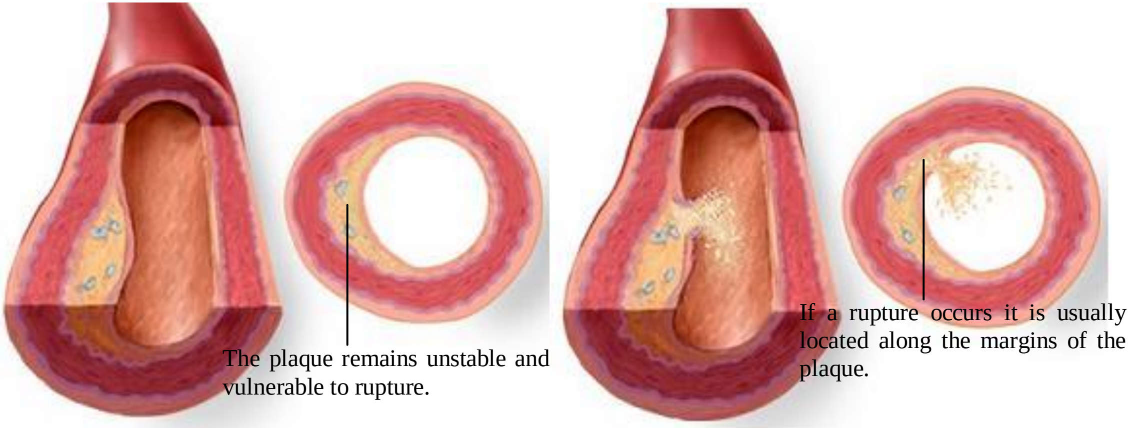

The plaque remains unstable and vulnerable to rupture.

If a rupture occurs it is usually located along the margins of the plaque.

(c) Plaque rupture causes blood clots.

(c) Blood clots block the artery.

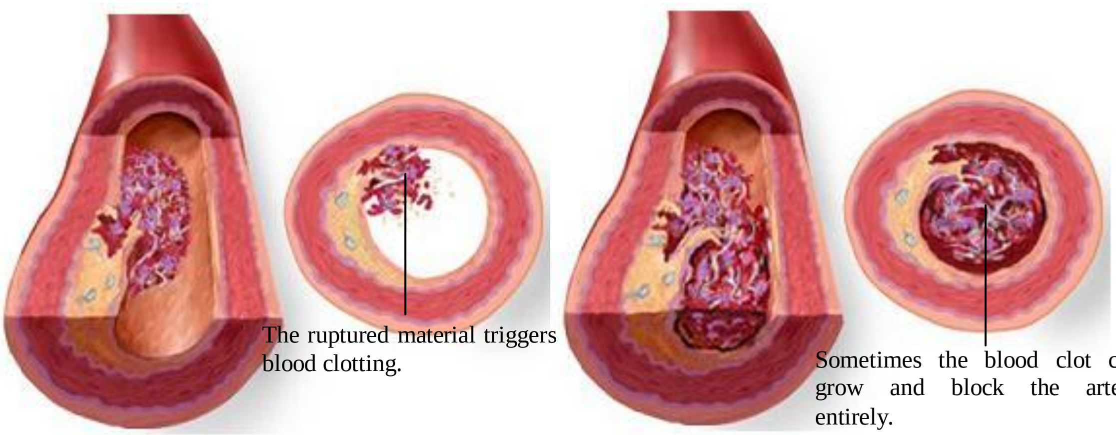

The ruptured material triggers blood clotting.

Sometimes the blood clot can grow and block the artery entirely.

Figure 2.3. Diagrams showing the plaque rupture: (a) an unstable plaque with thin fibrous cap; (b) the plaque remains unstable and vulnerable to rupture (It is usually located along the margins of the plaque); (c) plaque ruptures cause blood clots; (d) sometimes the blood clot can grow and block the blood flow to the heart and brain, causing a heart attack or stroke [2].

Fuster (2002) stated the definition of a vulnerable plaque: “A plaque that is documented to have a high likelihood of becoming disrupted and forming a thrombogenic focus. The thrombus could produce immediate disease onset or rapid, symptomatic, angiographic progression.” The risk of plaque rupture is believed to depend on plaque composition, morphology, biomechanical force, localization, vessel remodelling, blood conditions (cholesterol, sugar, etc), chemical environment, lumen surface (inflammation) and stenoses, and structural composition [15, 22-24, 26, 28]. Three major determinants of a plaque’s vulnerability to rupture are considered [25]:

- **a)** The size and consistency of the lipid-rich core.
- **b)** The thickness and density of smooth muscle cells and collagen content of the fibrous cap overlying the core.
- **c)** Active inflammatory and immunological processes within the fibrous cap.

However, the extent to how well these factors predict plaque vulnerability and risk of rupture is unknown. The mechanism through which the plaque rupture occurs is not well understood [9, 12, 14, 25].

2.4 Non-Invasive Visualization of Carotid Atherosclerotic Plaques

Among imaging modalities, the two most promising non-invasive imaging methods that have been used to study carotid atherosclerotic plaques are magnetic resonance imaging (MRI) and computed tomography (CT). Both are capable of identifying the morphological features such as luminal diameter and stenosis, wall thickness, and differentiate different tissue types [15, 74]. Modern CT scanners have shown high sensitivity for the detection of calcified plaques and reliable assessment of vessel wall thickness [13, 51]. However, they are not able to fully characterize the composition of the atherosclerotic plaque in the vessel wall and provide such detailed information on plaque composition as MRI can [74].

High-resolution magnetic resonance imaging (MRI) has been emerged as the potential leading non-invasive *in vivo* imaging modality for atherosclerotic plaque characterization [15, 55, 25, 84-85]. Yuan, Cai et al. developed multi-contrast techniques to improve the quality of MR images and to better differentiate various components of the plaque [86-88]. Human carotid, aortic, and coronary specimens were studied with *ex vivo* multi-contrast MR (T1-, proton density- and T2-weighted) and compared with histology [25, 46, 56, 83, 88]. The results of these studies indicate that MRI can characterize plaques with a high level of sensitivity and specificity.

Atherosclerotic plaque characterization by MRI is based on the signal intensities (preliminary finds are summarized in Table 2.1) and morphological appearance of the plaque on T1W, PDW, and T2W images. Calcium deposits are defined as hypointense regions within the plaque on T1W, PDW, and T2W images. Lipid components are defined as hyperintense regions with the plaque on both T1W and PDW images, and as hypointense on T2W images. Fibrocellular components are defined as hyperintense regions of the plaque on T1W, PDW, and T2W images. Calcification and fibrocellular tissue are readily identified. Lipid core is also identifiable. However, thrombus was the plaque component for which MRI had the lowest sensitivity [25].

	T1W	PDW	T2W
Calcium	Very hypointense	Very hypointense	Very hypointense
Lipid	Hyperintense	Hyperintense	Hypointense
Fibrocellular	Very hyperintense	Very hyperintense	Very hyperintense
thrombus	Very hyperintense	Hyperintense	Variable

Table. 2.1. Plaque characterization with Magnetic Resonance. T1W is T1-weighted; T2W is T2-weighted; PDW is proton density weighted [25].

In addition to MRI's abilities to define the vessel lumen and wall, and characterize atherosclerotic plaque, MRI is perhaps the most powerful technique available for imaging blood velocities *in vivo*. It has been demonstrated that phase contrast MRI (PC-MRI) can accurately measure time-varying velocities under uniform flow conditions [16]. However, in practice, such an "imaging only" approach has been successfully applied only to relatively straight vessels, owing to the implicit assumption of uniform flow that underlies most *in vivo* velocimetry techniques [58].

2.5 Review of Image-based Computational Models

Development in medical image technology has led to impressive progress in image-based computational modeling which adds a new dimension (mechanical analysis) to atherosclerotic plaque image analysis. Mechanical forces play an essential role in plaque progression and rupture. Plaque itself would not rupture if no forces were acting on it. However, as of now, the mechanisms governing plaque progression and causing plaque rupture are not fully understood. The computational models to perform mechanical analysis have been proposed to investigate plaque rupture and assess plaque vulnerability.

2.5.1 3D Structure-only Models

Few 3D structure-only papers for atherosclerotic plaque mechanical analysis can be found in the current literature. Holzapfel et al. developed a multi-layer anisotropic 3D model for eight distinct arterial components (adventitia, non-diseased media, non-diseased intima, diseased media, fibrous cap, lipid pool, calcification, and fibrotic part) associated with specific mechanical responses based on a human stenotic post-mortem artery's in vitro MRI [31].

Mechanical tests were conducted to provide a fundamental basis for the formulation of large strain constitutive laws. The investigated arterial components are assumed to be (nearly) incompressible fiber-reinforced composites, which are strongly nonlinear anisotropic responses and undergo large strains. The artery is fixed axially at one end, while the other end is exposed to displacements according the axial in situ prestretch. The 3D finite-element material model was solved by ABAQUS V5.8 to analyze the balloon-artery interactions during balloon expansion and stent deployment. The multi-layer anisotropic model was compared with some simplified models (neglecting axial in situ pre-stretch, assuming plane strain states, and isotropic material responses), and maximum stress deviations of up to 600% were found. Their findings suggest that model simplifications need to be carefully justified. Computational predictions may be different from different models and should be interpreted with extreme caution.

2.5.2 3D Fluid-only Models

In a series of papers, Long et al. combined computational fluid dynamics (CFD) techniques and MRI processing together to perform patient-specific flow analysis based on *in vivo* MRI images from real patients [44]. In addition to the realistic vascular geometry, the real-time measure velocity data obtained with MR CINE-PC technique was necessary. The numerical solutions were carried out using a user-enhanced commercial, finite volume-based program CFX4.2. Their results showed that geometry of the carotid bifurcation was highly complex, involving helical curvature and out-of-plane branching. These geometrical features resulted in patterns of flow and wall shear stress significantly different from those found in simplified planar carotid bifurcation models. Comparisons between the predicted flow patterns and MR measurement demonstrated good quantitative agreement. Steinman introduced a novel method to construct a tubular model of the carotid artery using measured diameter and wall thickness [58]. Along with time-varying inlet/outlet flow rates measured via PC MRI, the lumen boundary was used as input for computational fluid dynamic (CFD) simulation. Their results show good agreement between simulated and measured velocities, and demonstrate a correspondence between wall thickening and low and oscillating shear at the carotid bulb. However, a quantitative general relationship between wall shear stress (WSS) and wall thickness was not found [59]. Frieke et al. proposed a whole-blood viscosity modelling to investigate the effects of non-Newtonian blood viscosity, variations in flow rate, and vessel diameter on wall phenomena in a carotid bifurcation model. The flow was simulated by means of the finite element method. The viscosity was modelled by adapted Carreau-Yasuda model, and is a function of shear rate. The results indicate that flow increases have a large effect on the WSS. Low plasma viscosity was associated with a low WSS, which implies a contradiction, because both high WSS and low plasma viscosity are thought to be indicators for a healthy system. Maximum WSS oscillations were found at the edges of the recirculation region [8].

2.5.3 3D Fluid-Structure Interactions Models

Tang and his group began developing fluid-structure interactions (FSI) models starting in the early 1990’s. Their earlier works were based on in vitro experimental models developed by Ku, Kobayashi et al [41, 65]. They introduced a series of experiment-based FSI models of blood to investigate the wall deformation, stress and strain distribution, and flow properties of blood flow in carotid arteries with symmetric and asymmetric stenoses. The Navier Stokes equations were used as the governing equations for the fluid and the elastic properties of the stenotic tubes were determined experimentally. ADINA was selected to solve the models. Their results revealed that the behaviors of the 3D flow and stress/strain distributions are very different from those of 2D models. Experimental data for a silicone tube with a 78% stenosis by diameter was used to derive the stress/strain relationship and flow properties. Stenosis severity and asymmetry have considerable effects on critical flow conditions and stress/strain distributions [60, 66]. They also introduced a numerical method using generalized finite differences to solve a nonlinear axisymmetric FSI model with a free moving boundary. This method was used to study unsteady viscous flow in collapsible stenotic tubes simulating blood flow in stenotic carotid arteries. The elastic properties of a tube wall are determined experimentally using a Polyvinyl Alcohol (PVA) hydrogel artery stenosis model. Their results indicate that severe stenoses cause cyclic pressure changes between positive and negative values at the throat of the stenosis, cyclic tube compression and expansions, and shear stress changing directions in the region just distal to the stenosis under unsteady conditions. Computational and experimental results are compared and reasonable agreement is found [61].

Many other authors also developed 3D FSI models. Zhao et al. introduced image-based computational fluid-structure interactions (FSI) models to quantify fluid shear stress and mechanical wall stress in normal subjects in a clinical setting, and to define regions of low wall shear stress and high mechanical stress. The fluid /wall modelling was solved by integrating a fluid dynamics code CFX (CFX4, 1995) and a solid mechanics code ABAQUS (ABAQUS5.5, 1996). Their results revealed that some regions of the artery wall are exposed simultaneously to low wall shear stress and high mechanical stress and that these regions correspond to areas where atherosclerotic plaque develops [89]. Younis et al. use FSI models to investigate inter-individual variations in flow dynamics and wall mechanics at the carotid artery bifurcation, and its effects on atherogenesis, in three healthy humans. The blood was treated as laminar, Newtonian and incompressible fluid. The arterial response is modelled using the standard lagrangian formulation for large displacements and large strains [3]. The models were solved by ADINA [82]. Kaazempur-Mofrad et al. used MRI-based FSI models to study the correlations between fluid dynamic parameters and histological markers of atherosclerosis [32]. Four patients were scanned using MRI and ultrasound, and subsequently underwent carotid endarterectomy. For each patient, a geometric model and a numerical mesh were constructed from MRI data (without plaque components), and velocity boundary conditions established. The model was also solved by ADINA. Correlations attempted between the various fluid dynamic variables and the biological markers were interesting but inconclusive. Tendencies of maximum wall shear stress temporal gradient and average wall shear stress to correlate negatively with macrophages and lipid, and positively with collagen and smooth muscle cells, as well as tendencies of oscillatory shear index to correlate positively with macrophages and lipid and negatively with collagen and smooth muscle cells, were observed. These trends agree with hypotheses in the literature, which are based on *ex vivo* and in vitro experimental studies.

While fluid-structure interactions are included in the above models, investigations were mainly focused on flow behaviors and stress/strain distribution, plaque components were not included in these FSI models.

In 2003, Tang's group introduced a thick-wall stenotic model with a lipid core made with PVA hydrogel whose mechanical properties are close to those of carotid arteries. A hyperelastic Mooney–Rivlin model was used to implement the experimentally measured nonlinear elastic properties of the tube wall. A 36.5% pre-axial stretch is applied to make the simulation physiological. Their results indicate that severe stenosis leads to high velocity, high shear stress and low or even negative pressure at the throat, flow re-circulation, and wall compression or even collapse distal to the stenosis. Lipid core affects plaque stress/strain distributions considerably. Thin plaque cap and sharp angle of the lipid core are closely related to local extreme stress/strain conditions and may be sites of possible plaque rupture. Critical stress/strain conditions are affected (from 30% to more than 100%) by stenosis severity, eccentricity, lipid pool size, shape and position, plaque cap thickness, axial stretch, pressure, and fluid-structure Interactions [63, 71].

2.5.4 3D MRI-Based Multi-Components FSI Models

In addition to FSI models, 3D *ex vivo* MRI data set for a human coronary plaque with a large calcification block and a lipid-rich necrotic core was introduced by Tang's group to construct the model which was used to perform mechanical analysis for human atherosclerotic plaques and identify critical flow and stress/strain conditions which may be related to plaque rupture. The 3D nonlinear modified Mooney-Rivlin model was used to describe the material properties of the vessel wall and components. The flow was assumed to be laminar, Newtonian, viscous, and incompressible. The fully coupled fluid and structure models were solved by ADINA. Results were obtained and compared from a series of 3D models, which were based on *ex vivo* MRI and histological images, with different component sizes and plaque cap thickness, under different pressure and axial stretch conditions. These results indicate that large lipid pools and thin plaque caps are associated with both extreme maximum (stretch) and minimum (compression when negative) stress/strain levels [70]. They proposed that the local stress/strain behaviors at critical sites, such as very thin plaque cap and locations with plaque cap weakness, may be closely related to plaque rupture risk. Based on this, a stress-based computational plaque vulnerability index (CPVI) and critical site tracking (CST) method were proposed to assess plaque vulnerability. Their initial results showed good agreement with assessment given by histopathological analysis [67]. This is the first attempt to investigate the problem of coronary plaque rupture by integrating 3D multi-component FSI models, MRI images, and histopathological analysis. The proposed CPVI value is also a first attempt to quantify plaque vulnerability based on 3D FSI models. With the patient specific geometry, the results obtained from FSI simulation are more realistic and useful to understand the rupture mechanism. Their work fills a gap in current literature and may have the potential for future clinical applications.

Part II.

MRI Data Preparation and 3D Geometry Reconstruction

3. Image Processing for MRI

3.1 Introduction

Image segmentation is the technique to partition medical images of biological (for this thesis) organs into regions of different tissue types according to image intensities to obtain the morphology of the organ (artery plaque in our case). Accurate and reliable plaque morphology is one of the most basic elements needed to construct computational models.

High resolution MRI is capable of quantifying plaque morphology and plaque components [54]. Multi-contrast MR images are created by the differences in the strength of the nuclear magnetic resonance signal. Different contrast-MR images characterize tissues with different sensitivity, for instance, T1-MRI can distinguish calcification better than other contrast images; and GRE-weighting MRI can characterize lumen better than other contrast MRI. Therefore, it was hypothesized that multi-contrast MR images could enhance the differentiation of various tissue components based on their signal intensities in different MR weightings. An automated multi-contrast plaque segmentation method using Bayes theorem with normal probability distribution is introduced in this chapter [35]. In addition to saving the time in image review, the proposed automated segmentation procedure would also permit combination of multi-contrast MR Image. Results from *ex vivo* MRI of a patient were obtained and validated by histological data.

3.2 Probabilistic Framework

We assume that the class label ω is a discrete random variable taking values in the set of class labels $\Omega = \{\omega_1,\ \omega_2, \dots, \omega_c\}$. The *prior probabilities*, $P(\omega = \omega_i)$, *i*=1, ..., *c*, constitute the probability mass function (pmf) of the variable ω_i,

$$0 \leq P(\omega = \omega_i) \leq 1 \text{ and } \sum_{i=1}^{c} P(\omega = \omega_i) = 1 \tag{3.1}$$

Assume the objects, represented by $\mathbf{x} = (x_1,\ x_2, \ldots, x_n)$, from class ω_i are distributed in $\mathbb{R}^n$ according to the *class-conditional probability density function* (pdf) $P(\mathbf{x}|\omega_i)$, where $P(\mathbf{x}|\omega_i) \geq 0$, $\forall\ \mathbf{x} \in \mathbb{R}^n$, and

$$\int_{\mathbb{R}^n} p(\mathbf{x}|\omega_i) dx = 1,\ i = 1, \ldots, c \tag{3.2}$$

The likelihood of **x** is given by *unconditional* pdf,

$$P(\mathbf{x}) = \sum_{i=1}^{c} P(\omega_i) P(\mathbf{x}|\omega_i) \tag{3.3}$$

Given the prior probabilities and the class-conditional pdf, we can calculate the posterior probability using famous Bayes' decision theory [42],

$$P(\omega_i|\mathbf{x}) = P(\omega_i) P(\mathbf{x}|\omega_i) / P(\mathbf{x}) \tag{3.4}$$

3.3 Segmentation Method

3D multi-contrast *in vivo*/*ex vivo* MR images and corresponding Histological images of a patient's atherosclerotic plaque were provided by Dr. Zheng's group using protocol approved by Washington University Institutional Review Board with informed consent obtained where applicable. 3D Multi-contrast MRI data including *in vivo, ex vivo* MR Images were acquired on a GE SIGNA 1.5T MR scanner. The *in vivo* imaging data set involved multi-contrast weighting images with T1-, T2- density and proton density (PD) weightings. Each contrast weighting session consists of 14 2D slices with high resolution (FOV=130×130 mm^2; matrix size: 640×640; slice thickness=3mm). The *ex vivo* imaging data set consists of T1-, T2-, gradient-echo (GRE) density and PD weighted MRI images. Each contrast weighting sessions included 32 2D slices with high resolution (FOV=56×56 mm^2; matrix size: 512×512; slice thickness=1mm).

The pixels in the training set were performed to generate the probability function which was used to determine the probability that each pixel belongs to each tissue type, and the maximum likelihood classifier was selected to determine which tissue type the pixel belongs to. Using clustering results, the segmentation can be done by the Canny edge detection in the Image Processing Toolbox which is provided by MATLAB (MathWorks, MATLAB, Natick, MA). The digital contour data were then automatically acquired using a self-developed program developed in MATLAB. The segmentation procedures are given by Diagram. 3.1, the details followed.

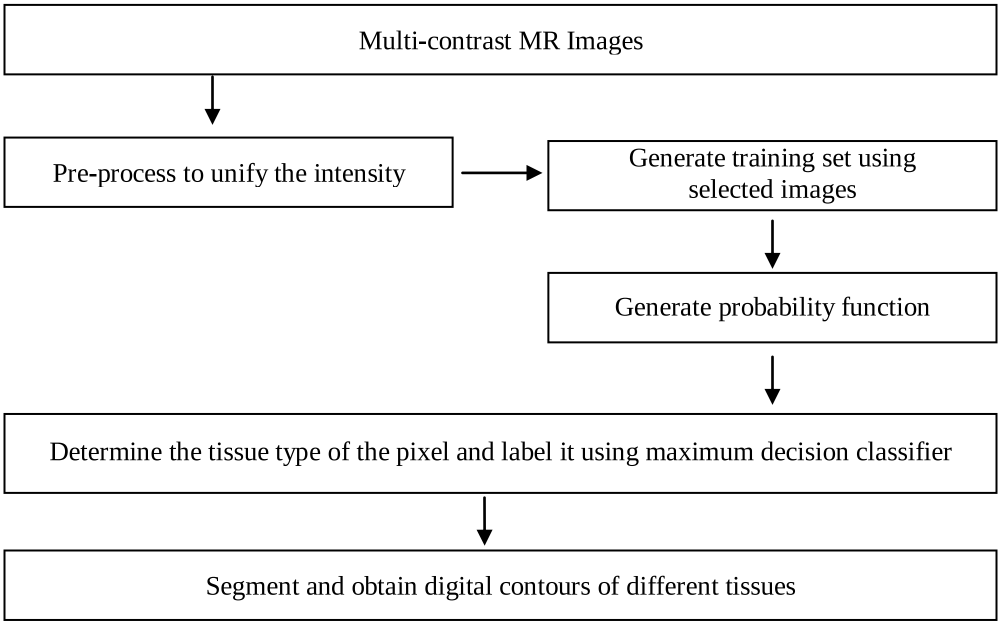

Diagram 3.1. Flowchart of plaque tissue segmentation.

3.3.1 Pre-processing

The intensity of each image should be adjusted to be relatively uniform due to the effects of coil inhomogeneity. The region (14mm×14mm), which is in the center of the vessel, was selected as the interesting one. The contrast of the image was increased by linear transformation,

$$u_1 = \frac{u_0-m}{M-m} \times 255 \tag{3.5}$$

Where u_0 is the initial intensity, u_1 is adjusted intensity, M is the maximum intensity, and m is the minimum intensity. Fig. 3.2 shows the effects of pre-processing of unified intensity.

(a) Original T2-weighted MRI

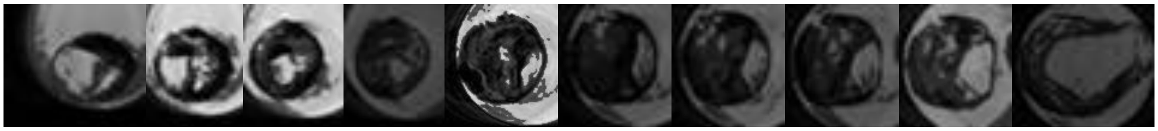

(b) Resultant images after contrast increase

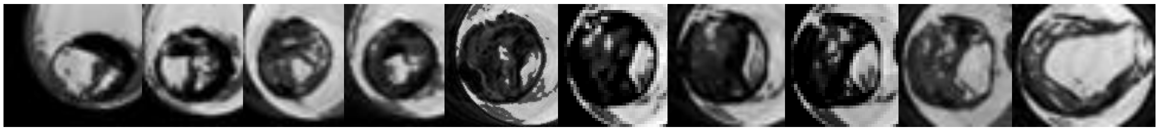

Figure 3.1. Pre-Processing results of selected slices from 32 slices of ex vivo MR Images: (a) original T2-weighted MRI (b) resultant images after contrast increase.

3.3.2 Training Set

The training set was used to generate the probability density function (3.7) which would be used to determine the probability of that pixel in the images belongs to each tissue type. From slices with histological images of *ex vivo* data set, slice 14 and 26 were selected. To generate the training set for segmentation, images of those two slices were manually segmented based on registered histological results and relative intensity. A total of 573 pixels (each pixel contains 4 densities representing all 4 different contrast weightings) were selected randomly for study. From the segmentation results, each location was determined to belong to 4 tissue types including lipid (denoted as Z_1), normal tissue (denoted as Z_2), calcification (denoted as Z_3) and others (including lumen or outer tissue, denoted as Z_4).

3.3.3 Generating the Probability Density Function

The most important part of the segmentation algorithm is to determine the probabilities of each pixel belonging to each tissue type. These probabilities represent the likelihood that the tissue at the location of the pixel is lipid, calcification, normal tissue or others. The probabilities were determined by the probability density function which is generated based on the theorem of section 3.2.

Each pixel has associated with the intensity vector $\vec{I} = (I_1,\ I_2,\ I_3,\ I_4)$ representing the intensity of the pixel in one of the contrast weighting MR images and Z_i, i =1, 2, 3, 4, corresponds to the label of the tissue. $P(Z_i|\vec{I})$ was used to represent the probability that the pixel belongs to i tissue type (Z_i). Assume that I_i is conditionally independent of I_j, $(i \neq j)$, that is, the intensity of one of the contrast weighting MRI does not depend on other contrast weighting MR images. This conditional independent assumption allows for the following representation,

$$P(\vec{I}\,|Z_i) = P(I_1|Z_i)P(I_2|Z_i)P(I_3|Z_i)P(I_4|Z_i) \tag{3.6}$$

Together with these assumptions and theorem of section 3.2 (eqn. (3.4), (3.5)), the posterior probability function was obtained,

$$P(Z_i|\vec{I}) = \frac{P(Z_i)P(\vec{I}|Z_i)}{\sum_{i=1}^{4} P(Z_i)P(I_1|Z_i)P(I_2|Z_i)P(I_3|Z_i)P(I_4|Z_i)} \tag{3.7}$$

The prior probability $P(Z_i)$ was estimated by the frequency of each of the four tissue types from the training set. Assume that the conditional probability density function (pdf) is a normal distribution, denoted by $I_j \mid Z_i \sim N(\mu_{ji},\ \sigma_{ji})$, where μ_{ji} and σ_{ji} is the unbiased estimation of the mean value and standard deviation respectively of i^{th} tissue type for j^{th} contrast weighting images.

3.3.4 Determining the Tissue Type

To make the smallest possible number of mislabeling, the maximum classifier was used to determine which tissue type the pixel belongs to, that is, the pixel was labeled with the class of the highest tissue type probability. Diagram 3.2 gives the flowchart of our maximum decision probability functional classifier, where $\vec{I}$ is the intensity of the pixel in multi-contrast weighting MR images transformed by preprocessing, $g_i(\vec{I})$ is the decision function pdf $P(Z_i|\vec{I})$. If $g_i(\vec{I})$ is the maximum value, then pixel with intensity $\vec{I}$ belongs to Z_i and is labeled *i*. The classification procedure will return a matrix has the same dimension with the image and the value of the element will be obtained classification label.

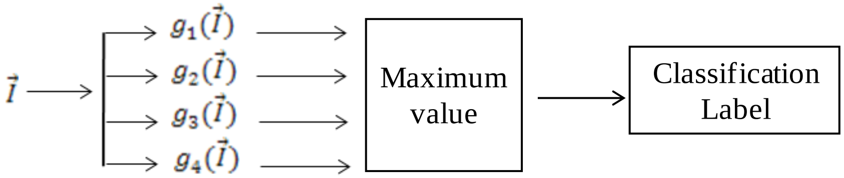

Diagram 3.2. Flowchart of maximum decision probability functional classifier.

3.3.5 Obtain the Digital Contours

The procedure in section 3.3.4 partitions the interested region of the MR images into classification regions denoted by $\mathcal{R}_1, \dots, \mathcal{R}_4$

$$\mathcal{R}_i = \left\{\vec{I} | g_i\left(\vec{I}\right) = \max_{k=1,\dots,4} g_k\left(\vec{I}\right)\right\}, \quad i = 1, \dots, 4 \tag{3.9}$$

This means that $\mathcal{R}_1, \dots, \mathcal{R}_4$ divides the image into 4 regions: region 1 ($\mathcal{R}_1$) is lipid; region 2 ($\mathcal{R}_2$) is normal tissue; region 3 ($\mathcal{R}_3$) is calcification; and region 4($\mathcal{R}_4$) is lumen or outer tissue. Fig 3.3(a) shows the classifier results, using different color to represent different tissue. To obtain the digital contours of plaque components using classification results, there are 3 steps as follows,

Step 1. Create the contour of the components

This step is to create the contours using the “edge” function in the Image Processing Toolbox based on classified results. The input is a matrix generated by the classifier procedure (section 3.3.4), and the output will be a new matrix with value either 0 (if the pixel is not at a contour), or 1 (if the pixel is at a contour).

Step 2. Label the contours

Step 2 is to generate a new matrix in the same size as the one obtained from step 1, in which if the pixel is the boundary of inner, outer, lipid, calcification, then the value of the new matrix will respectively be different (i.e. 1, 2, 3, ...), while the others will still be zero. This procedure will return a matrix with only a few values (depends on how many lipid and calcification components).

Step 3. Detect the boundary and save the digital contour data

We seek the first point of the line from the left lower location of the image as the starting point on the boundary. Each identified pixel has eight directions numbered by 0-7 (Fig. 3.2) [53]. Since the contour is a closed and connected curve, at least the pixel on one of these directions must also be a new boundary point. Hence each new point on the boundary can be represented by the former point and the direction.

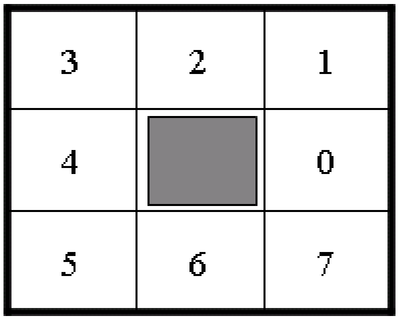

3	2	1
4	▨	0
5	6	7

Figure 3.2. Chain code, 0-7 represent 8 directions from the center point [53].

The following tracking rule was selected to improve the efficiency: Starting from the first point of the boundary, the horizontal direction (numbered 0) is chosen as the beginning direction. Here is an example for tracing a contour labeled by 1. If the neighbor in horizontal direction is labeled by 1 (that means the point is on the boundary), the current tracking procedure is finished. If not, the direction will be rotated by 45 degree in the clockwise direction (the number of direction is added by 1) till to find the first point which is labeled by 1. After these, the X/Y coordinate values of the finding point will be stored; the point in the matrix will be relabeled by 0, and taken as the new boundary point. The current direction will be taken as the new direction for the next seeking procedure after rotation by 90 degree in anti-clockwise direction (the number of direction is reduced by 2). Repeat these steps to find the new point on the boundary until going back to the first point. To save the storage space, we can only save the X/Y-coordinate values of the starting point and the directions other than the coordinate values for each new point. To simplify the problem, we saved X/Y coordinate values as the digital contour data. The other contour data can be obtained by repeating the above tracking procedure.

3.4 Results

The conditional pdf $P(I_j|Z_i)$ was assumed to be a normal distribution denoted $I_j|Z_i \sim N(\mu_{ji},\ \sigma_{ji})$, that is,

$$P\left(I_j\middle|Z_i\right) = \frac{1}{\sqrt{2\pi}\sigma_{ij}} exp\left[-\frac{\left(I_i-\mu_{ij}\right)^2}{2\sigma_{ij}^2}\right] \tag{3.9}$$

Where μ_{ij} and σ_{ij} are the unbiased estimation of mean value and standard deviation separately of the i^{th} tissue type for the j^{th} contrast weighting images calculated from the training set given in table 3.1.

μ_{ij}	I_1	I_2	I_3	I_4	σ_{ij}	I_1	I_2	I_3	I_4
Z_1	89	131	81	55	Z_1	25	20	41	31
Z_2	111	123	67	111	Z_2	38	35	48	48
Z_3	21	23	22	21	Z_3	15	9	13	11
Z_4	210	215	191	229	Z_4	15	19	40	17

Table 3.1 Results of unbiased estimation of mean value and standard deviation separately of i^{th} tissue type for j^{th} contrast weighting images calculated from training set.

Fig. 3.3 (a) presents the classification results, with lipid in red, the calcification in yellow, normal tissue in blue, and others (including lumen) in green. Fig. 3.3 (b) gives the contour result based on 3.3(a). Fig. 3.3 (c)-(f) presented the segmentation result shown in all different contrast weighting MR images. Fig. 3.3 (g) showed the corresponding histological images, where C, L represent calcification and lipid respectively. The results match pathology well. The image processing results of all *ex vivo/ in vivo* MR Images are presented in Fig. 3.4 & Fig. 3.5.

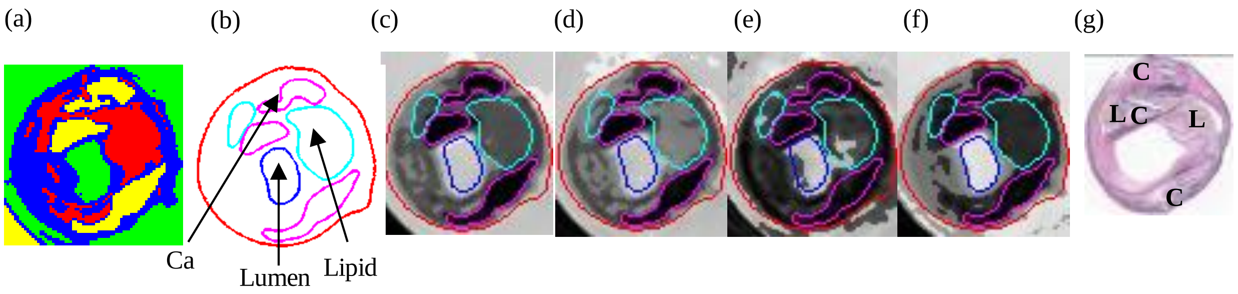

Figure 3.3. Segmentation results of selected slice (Slice 24) of patient-specific multi-contrast MRI. (a) Automatic segmentation result of classifier procedure; (b) Segmented contour result; (c)-(f) give segmentation results on T1, PD, T2, GRE weighting MR images respectively; (g) shows corresponding histological images. Our contour results show excellent agreement with histopathological data.

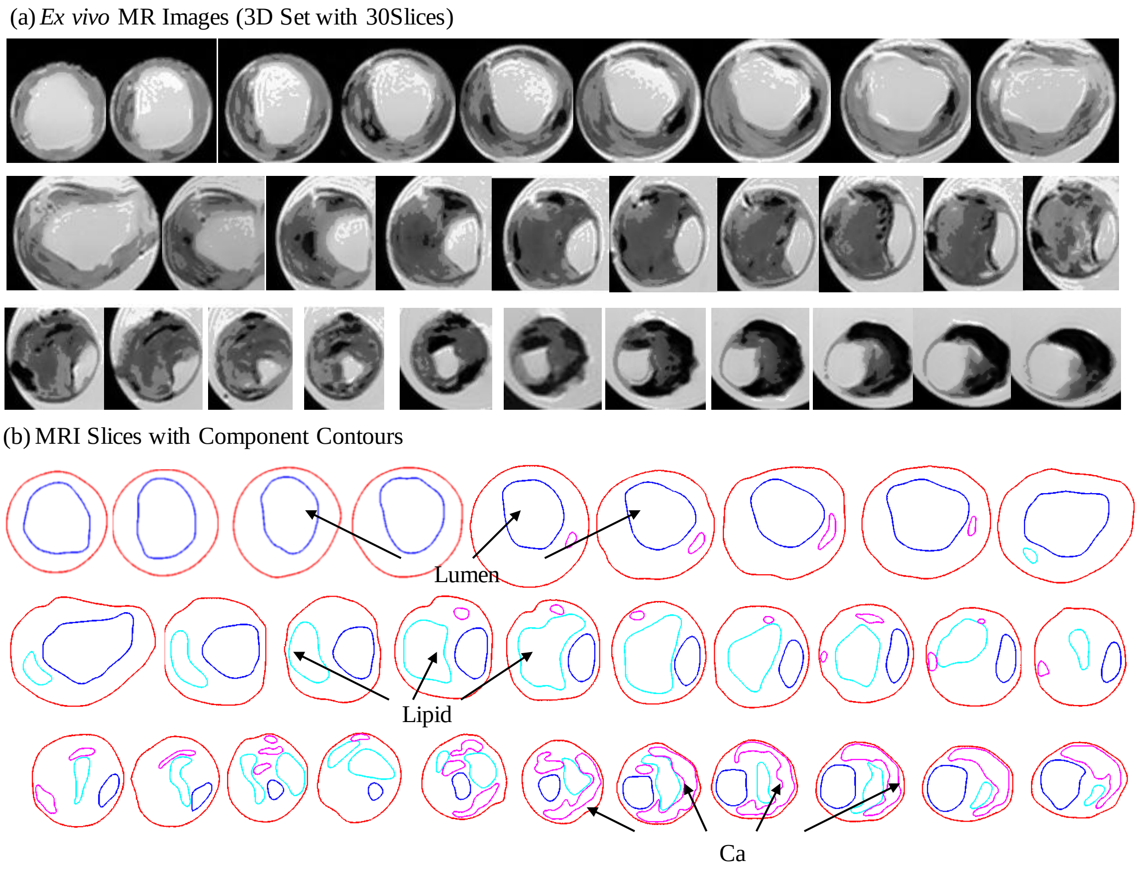

Figure 3.4. Segmented contour plots of all ex vivo MRI slices showing plaque components.

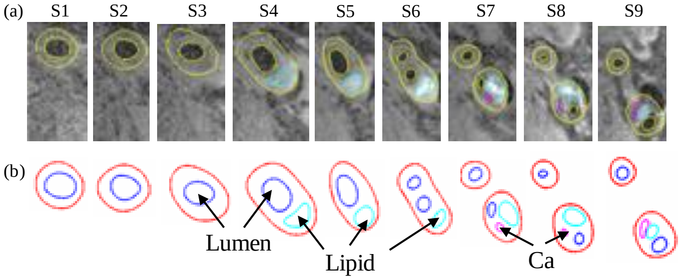

Figure 3.5. Segmented contour plots of all in vivo MRI slices showing plaque components. (a) Segmentation results on 9 in vivo MRI (T1W) slices (S1-S9); (b) Segmented contour plots for (a) showing plaque components;

3.5 Conclusion

In this chapter, a method to automatically segment MRI data set and obtain the digital contours of plaque components was introduced. The maximum decision probability functional classifier was applied to multi-contrast weighted MR image processing. Histological images were used to validate the reliability of the segmentation method for multi-contrast weighting *in vivo* and *ex vivo* MR images. The segmentation method is a simple technique while results in high accuracy. To simplify the problem, we use "Canny" edge function tool to segment the images. In the future, combining this classification method with other segmentation methods may lead to improvement.

4. 3D Geometry Reconstruction and Mesh Generation

There are three main steps involved in 3D geometry re-construction and mesh generation for human carotid atherosclerotic plaque FSI models: 1) acquire 3D *in vivo* MRI data; 2) re-construct 3D geometry and generate mesh for both structure and fluid domains; 3) connect fluid and structure domains and set fluid-structure interactions. Proper mesh is critical for the convergence of a 3D fluid-structure interaction model. However, the complex deformable plaque structure and components in the plaque significantly increase the difficulty of the mesh generation process which is very difficult to handle by available commercial software. A Volume Component-Fitting Method (VCFM) was introduced to generate mesh for 3D multi-component FSI models. The general idea of this technique is to divide the plaque geometry into hundreds or even thousands of small "volumes" to curve-fit the very irregular plaque geometry and all the components which are "inclusions" in the structure. Each small volume has a more regular shape for mesh/element generation. The general VCFM procedure was used to generate 3D mesh for the following three geometrical domains:

a) plaque component in the vessel: 3D solid body whose external surface is defined by the component boundary;

b) fluid domain: 3D fluid body whose external surface is defined by lumen.

c) vessel structure domain: 3D solid body defined by outer vessel surface and lumen with plaque component inclusions.

The procedure is presented in details and illustrated in this chapter using the specific data (Fig. 4.1) provided by Dr. Zheng's group. The geometry reconstruction and mesh generation was made under ADINA computing environment.

(a) In Vivo MR Images (3D Set with 16 Slices)

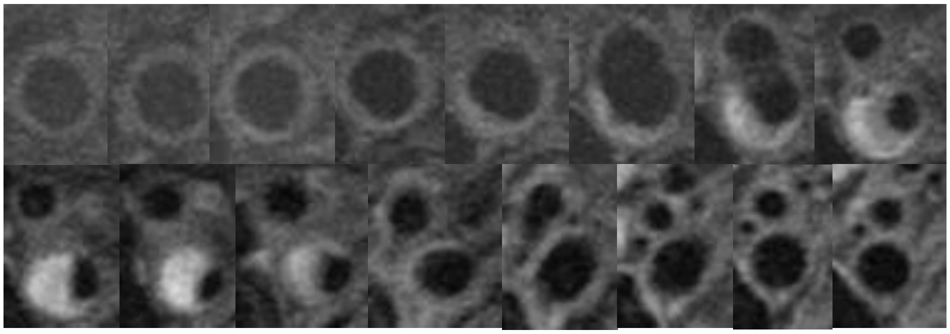

(b) Segmented MRI Slices with Component Contours

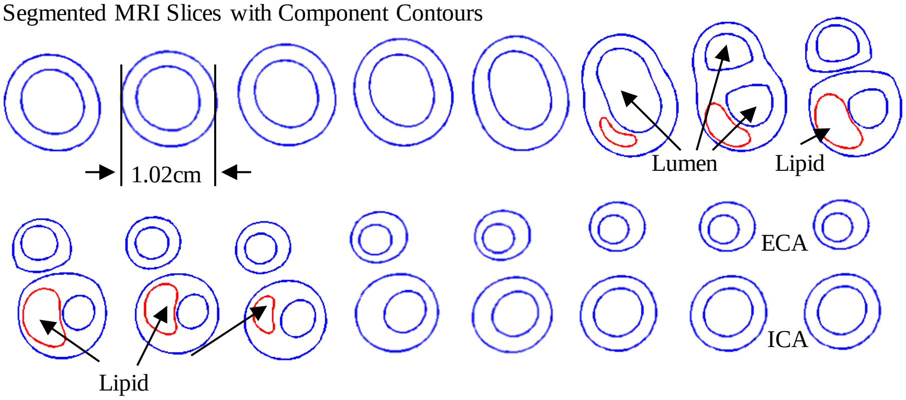

Figure 4.1. In vivo 3D MRI images of a human carotid plaque and re-constructed 3D geometry. (a) 16 MRI (T1) slices (S1-S16), slice spacing: 3mm. Each image shown here was cut from the whole neck image. (b) Segmented contour plots showing plaque components.

4.1 Constructing Plaque Component Domain

The plaque sample given by Fig. 4.1 has a lipid core as its only inclusion. Fig. 4.2(a) shows the contours of the lipid. According to the geometric features of the lipid component, the geometry of the lipid was divided into 5 hexahedral volumes. Each volume was generated, followed by defining the points, lines, and surfaces. To construct the lipid domain, the first step is to import segmented contour data from MR images into ADINA input file (Fig. 4.2(a)), pixel by pixel. The second step is to generate proper lines based on input contour points as the edge of surface for a volume (Fig. 4.2(b) & (c)). In the same surface, there are four polylines, using smoothing spline method to fit the geometry points well, generated to enclose an area which will be further assigned to be a surface (Fig. 4.2(b)). To generate the volume, the surface between two neighbored slices should also be created. Hence, two polylines and two straight lines were generated to enclose an area between two neighboring slices (Fig. 4.2(c)). The third step is to define the surfaces by edges which were specified in the second step. The next step is to define the volume surrounded by defined surfaces. A hexahedral volume was bounded by 6 facets with two facets in neighboring slices and 4 surfaces between these two neighboring slices (Fig. 4.2(c)). By repeating these steps slice by slice, the geometry of the lipid can be generated (Fig. 4.2(d)).

After the volumes were constructed, element group was assigned to each volume. Information about an element group includes element style, material and other information (such as assuming large-strain or large-displacement for the kinematic formulation for the element group). After specifying mesh density and mesh style for each volume, the fluid domain now can be meshed in ADINA (Fig. 4.2(e)). There are a total of 2168 elements generated for this lipid core component. All procedures described above were written in a ADINA-in file using the Adina infile program language.

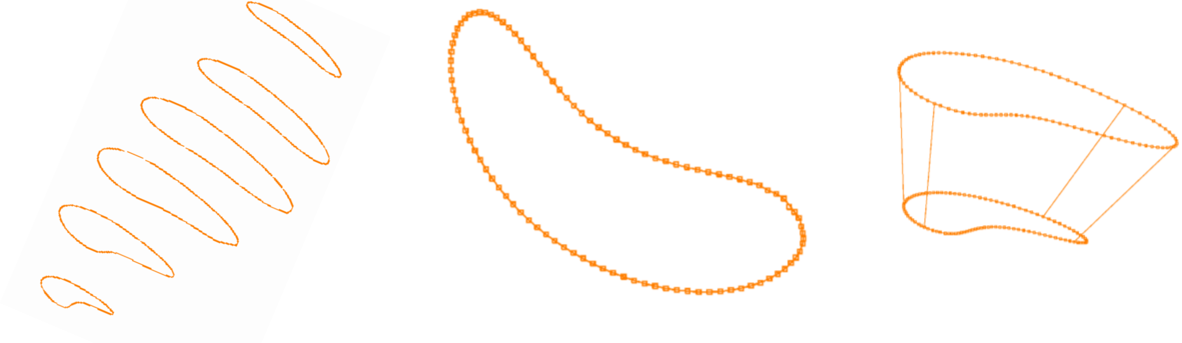

(a) Data points used to construct the lipid.

(b) Data points in one slice of lipid and corresponding smoothed line using spline function.

(c) Lines creation between two neighboring slices

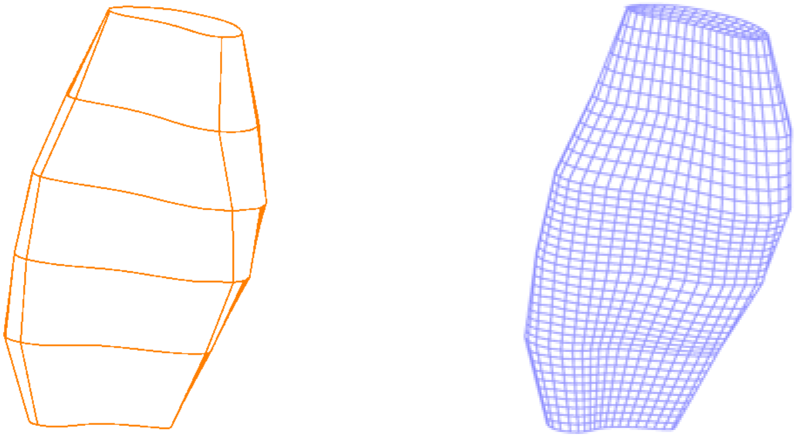

(d) Geometry of the lipid consisting of 5 hexahedral volumes.

(e) 8-node brick finite element meshing.

Figure 4.2 Stages in the 3D geometry reconstruction and mesh generation of the lipid component.

4.2 Constructing Fluid Domain

The fluid domain contains the following three parts:

1) Common carotid artery (CCA)
2) Internal carotid artery (ICA)
3) External carotid artery (ECA)

The geometries of ICA and ECA were constructed separately using the method in section 4.1 by hexahedral volumes. Compared with lipid domain, the difficulty of fluid domain is the bifurcation. To connect with ICA and ECA, the CCA was manually cut into two parts (Fig.

4.3(a)) by parallel lines. The center line (L_1) in S_6, which separated CCA, was selected to "parallel" edges L_2 and L_3 (Fig. 4.3 (b)) and separate slice 6 by the area proportions of slice 7 in ECA and ICA. The 3D geometry reconstruction and mesh generation of the fluid domain were presented in Fig. 4.4.

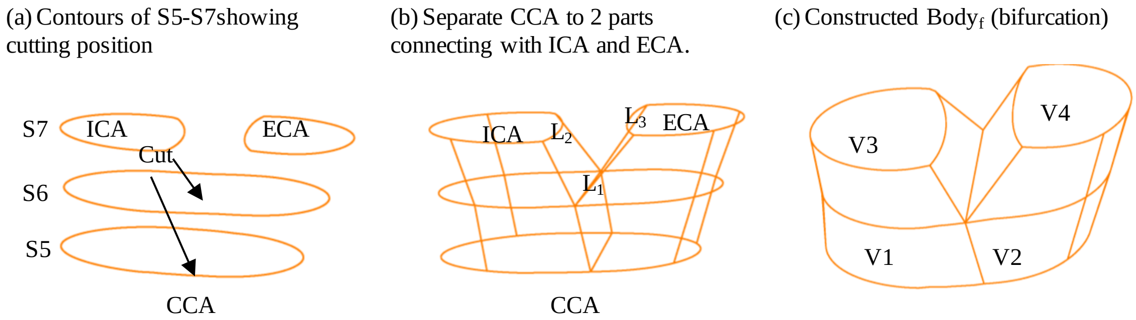
(a) Contours of S5-S7showing cutting position

(b) Separate CCA to 2 parts connecting with ICA and ECA.

(c) Constructed Body_f (bifurcation)

Figure 4.3. Showing the procedure of 3D geometry reconstructions of bifurcation.

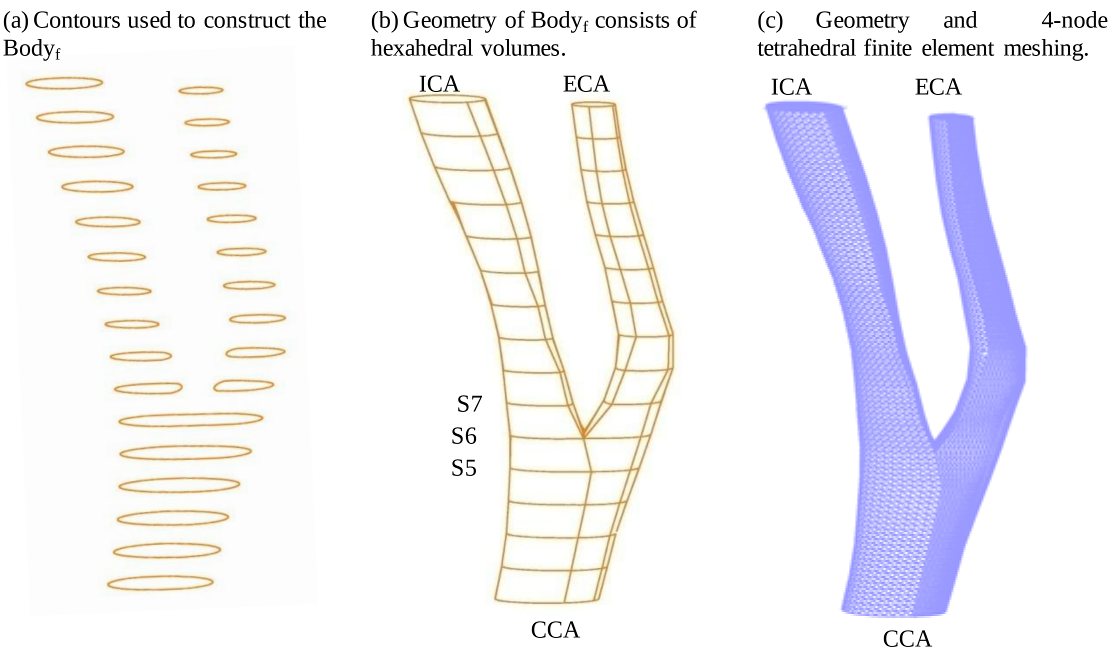
(a) Contours used to construct the Body_f

(b) Geometry of Body_f consists of hexahedral volumes.

(c) Geometry and 4-node tetrahedral finite element meshing.

Figure 4.4. 3D geometry reconstructions and mesh generation of fluid domain.

4.3 Constructing Structure Domain

In addition to the bifurcation, the multi components increase the difficulty of 3D geometry reconstruction and mesh generation. Due to this complexity of the geometry of the structure, in addition to hexahedral volume mode, prismatic and 5-faced volume modes were employed to generate volumes to fit the plaque geometry. To create such proper small volumes, some artificial contours were added to help divide each slice into a few areas (Fig. 4.5(a) & (b)).

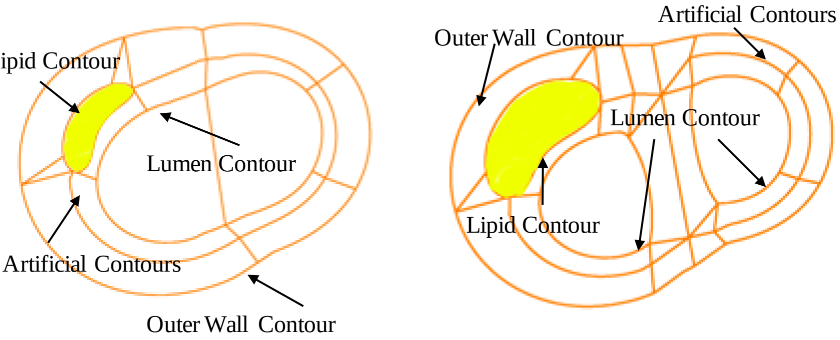

(a) Created Lines connecting data points and dividing Slice 6.

(b) Created Lines connecting data points and dividing Slice 7.

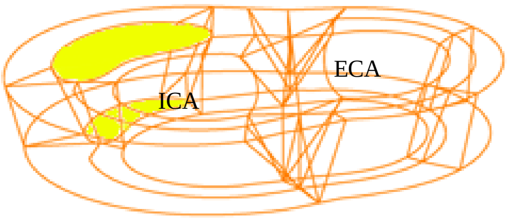

(c) Create lines between two neighbored slices (Slice 6 & 7)

Figure 4.5. Created lines of two neighboring slices for constructing volumes to fit plaque geometry.

Due to the thin plaque cap and components with sharp angles, finer meshes are necessarily used to get better resolution and handle high stress concentration behaviors. There are a total of 298 small volumes and 95,296 elements generated (Fig. 4.6(a) & (b)).

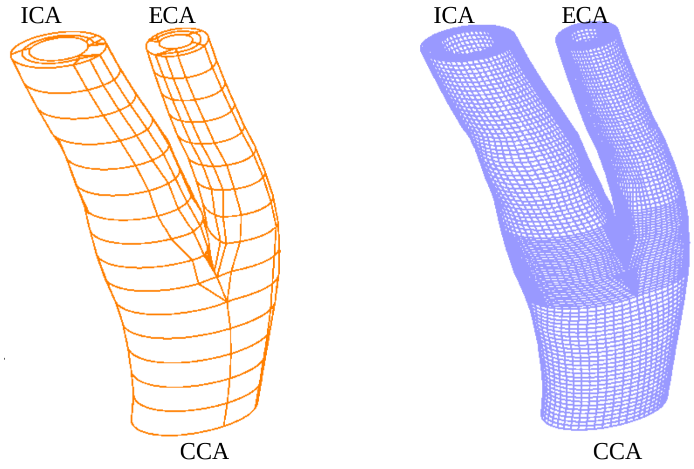

(a) Geometry of normal tissue consist of 298 volumes

(b) 8-node brick finite element meshing.

Figure 4.6 3D geometry construction of structure domain (normal tissue) and mesh generations.

Part III.

FSI Models, Solution Methods and Validations

5. The 3D *In Vivo* MRI-Based FSI Model

Fluid-structure interactions (FSI) analysis integrates both flow and structure forces and motions together, places plaque in a more realistic environment, and provides more accurate assessment for plaque vulnerability. In this chapter, a brief theoretical framework for 3D FSI plaque models is presented which includes fluid part for blood flow through the artery and solid part for the arterial wall and other plaque components.

5.1 Fluid Model

Blood flow is assumed to be laminar, viscous, incompressible and Newtonian. No-slip condition is applied at the fluid-vessel interface, i.e., flow velocity at the flow-vessel interface is set to be the same as that of the vessel wall. For FSI computational model, the fluid domain changes while the structure deforms and that requires frequent mesh adjustments. The Arbitrary Lagrangian-Eulerian (ALE) formulation of the Navier-Stokes equations is used as governing equations for the blood flow:

$$\rho(\partial \mathbf{u}/\partial t + ((\mathbf{u} - \mathbf{u}_g) \cdot \nabla)\, \mathbf{u}\,) = -\nabla p + \mu \nabla^2 \mathbf{u}\,, \tag{5.1}$$

$$\nabla \cdot \mathbf{u} = 0, \tag{5.2}$$

where $\mathbf{u}$ is the flow velocity, $\mathbf{u}_g$ is the mesh velocity, μ is the coefficient of viscosity, p is the pressure, and ρ is the density of blood. ALE formulation uses the moving mesh as the reference frame and is especially suitable for problems with fluid-structure interactions.

As the finite element mesh moves, the volume of each cell in the grid changes, and the fluid mass is not conserved for each individual cell. Therefore, Geometry Conservation Law (GCL) must be applied in the discrete sense,

$$\text{Cell Volume}\,|_{new} - \text{Cell Volume}\,|_{old} = \int_v \nabla \cdot \mathbf{u}\, d\mathbf{V} \tag{5.3}$$

Boundary conditions are prescribed as,

$$\mathbf{u}|_{\Gamma} = \partial \mathbf{v}/\partial t|_{\Gamma}, \quad \partial \mathbf{u}/\partial n|_{\text{inlet, outlet}} = 0, \tag{5.4}$$

$$p|_{\text{inlet}} = p_{\text{in}}(t), \quad p|_{\text{outlet}} = p_{\text{out}}(t), \tag{5.5}$$

where Γ represents the inner wall of the vessel, p is the pressure, **v** is the solid displacement vector.

5.2 Solid Model

The solid model is a set of equations that governs the behaviour of the blood vessel wall under loads with variables of displacement, stress (measures of force per unit area), and strain (deformation measures). The motion of the artery wall is governed by the following differential equations,

$$\rho\, v_{i,tt} = \sigma_{ij,j}, \quad i,j=1,2,3, \qquad \text{(Equation of Motion)}, \tag{5.6}$$

where *t* stands for time, *i* and *j* label spatial coordinates, **v** is the solid displacement vector, $\boldsymbol{\sigma}=[\sigma_{ij}]$ is the stress tensor, $f_{\cdot,j}$ stands for derivative with respect to the j^{th} variable. Here, body force due to gravity is ignored. Einstein summation convention is applied here and in all equations in Chapter 5 & 7.

The strain-displacement relations is given by,

$$\varepsilon_{ij} = (\, v_{i,j} + v_{j,i} + v_{\alpha,i}\, v_{\alpha,j})/2, \quad i,j,\alpha=1,2,3, \tag{5.7}$$

where $\boldsymbol{\varepsilon}=[\varepsilon_{ij}]$ is the Green-Lagrange strain tensor.

To introduce the constitutive material models (stress-strain relations), both artery wall and plaque components are assumed to be hyperelastic, isotropic, incompressible, and homogeneous. The non-linear Mooney-Rivlin hyperelastic model is used as the constitutive law for all materials [3-4, 69-70]. The Strain energy density function is given by,

$$W = c_1(I_1 - 3) + c_2(I_2 - 3) + D_1[e^{D_2(I_1-3)} - 1] \tag{5.8}$$

where

$$I_1 = \sum C_{ii}, I_2 = \frac{1}{2}(I_1^2 - C_{ij}\,\mathrm{C}_{\mathrm{ij}}) \tag{5.9}$$

are the 1st and 2nd invariants of the deformation tensor $\mathrm{C}=[\mathrm{C}_{ij}]=\mathbf{X}^{\mathrm{T}}\mathbf{X}$, $\mathbf{X}=[\mathrm{x}_{ij}]=[\partial \mathrm{x}_i/\partial a_j]$ is the deformation gradient, where (x_i) is current position and (a_i) is the original position of the deformation tensor, and $\mathrm{c_i}$, $\mathrm{D_i}$ are the material constants. are the 1st and 2nd invariants of the deformation, and c_i, D_i are material constants, . The stress-strain relations can be found by [3-4]**,**

$$\sigma_{ij} = (\partial \mathrm{W}/\partial \varepsilon_{ij} + \partial \mathrm{W}/\partial \varepsilon_{ji})/2 \tag{5.10}$$

where σ_{ij} are the second Piola-Kirchhoff stresses.

Natural and traction equilibrium boundary conditions are specified by,

$$\sigma_{\mathrm{ij}} \cdot \mathrm{n_j}\ |_{\mathrm{out\_wall}} = 0,\ \sigma^{\mathrm{r}}_{\mathrm{ij}} \cdot \mathrm{n_j}\ |_{\mathrm{interface}} = \sigma^{\mathrm{s}}_{\mathrm{ij}} \cdot \mathrm{n_j}|_{\mathrm{interface}} \tag{5.11}$$

where **n** is the unit normal direction, superscripts r and s indicate different materials. For example, r represents lipid, s represent normal tissue.

5.3 Fluid Structure Interactions

The fluid and structure will be coupled through their interface. The conditions of traction equilibrium and compatibility of displacements/velocities along the structure-fluid interfaces must be satisfied,

$$\boldsymbol{f}_{\mathrm{f}}=\boldsymbol{f}_{\mathrm{s}}, \quad \text{(Traction Equilibrium)}, \tag{5.12}$$

$$\boldsymbol{v}_{\mathrm{f}}=\boldsymbol{v}_{\mathrm{s}} \quad \text{(Displacement Compatibility)} \tag{5.13}$$

$$\mathbf{u}_{\mathrm{f}}= \dot{\boldsymbol{v}}_{\mathrm{s}} \quad \text{(Velocity compatibility (Non slip condition))} \tag{5.14}$$

where ***v*** and ***f*** are the displacements and tractions, subscripts f and s stand for fluid and solid, respectively.

5.4 The Shrink-Stretch Process for *In vivo* MRI-Based FSI Models

Under physiological condition (*in vivo* state), the artery is axially stretched and pressurized [30]. That is, the segmented contours based on *in vivo* MR-image represent the deformed shapes of vessel wall and enclosed plaque components. For a non-linear computational model, the computer starting shape should be the one at zero-stress state [17-18, 20]. With this consideration, the *in vivo* segmented contours cannot be directly used for the 3D FSI computational model. A shrink-stretch process was introduced to achieve the start shape of plaque morphology for the computation model. Due to the limitation of current non-invasive technology, the residual stress [20] in the plaque is not measurable, and it is ignored. The procedures are presented as follows,

Step 1: Pre-Shrink.

Based on the axial and inner circumferential shrinkage rate, the *in vivo* geometry of plaque iss shrunk to obtain the geometry at no-load condition as the computer starting geometry. The shrinkage in axial direction is achieved by shortening the distance between MRI slices. In cross-section, inner lumen contour is shrunk with inner circumferential shrinkage rate. The volume conservation law,

$$\text{Plaque Volume }|_{in\ vivo} = \text{Plaque Volume }|_{\text{shrunk}} \tag{5.18}$$

is employed to determine the shrinkage rate for the outer wall contour. The component is proportionally adjusted if present. The lumen and outer boundary shrinkage rate are adjusted iteratively so that the computational geometry model under pressure and stretch reach best match with *in vivo* plaque geometry.

Step 2: Construction of Model and Obtaining Loaded Plaque Geometry.

The structure-only model will be re-constructed based on the shrunk contours and solved under ADINA environment using the method described in chapters 4, 5 and 6. The average values of systolic and diastolic pressures are used as the loading condition and axial stretch will be applied at both ends of artery while the simulation is performed to recover the *in vivo* length.

Step 3: Comparison and Best Match with *In Vivo* Geometry.

The deformed geometry are extracted and compared with the *in vivo* geometry. The initial circumferential shrinkage rate in **Step 1** are adjusted and the above steps are repeated until satisfied deviation between the deformed geometry and *in vivo* geometry is obtained.

According to the obtained results, skipping the shrinking procedure will induce unacceptable deviation either in 2D or in 3D computational models. The quantitative comparisons with 2D model are presented below (Fig. 5.1). Fig 5.1(a) shows segmented contours based on *in vivo* MRI Image. Fig. 5.1(b) is the corresponding shrunk contours with 10.5%, and 5.1% shrinkage rate for lumen and outer wall, respectively. When the inner shrunk contour is pressurized with the mean value (129mmHg) of systolic and diastolic pressures, the *in vivo* contours is well recovered as shown in Fig. 5.1(c). The deviations of lumen contour in width, height and area are 2.0%, 3.3% and 2.3%, respectively. However, if the simulation started directly from *in vivo* contours as shown in Fig. 5.1(e), the deformation is largely over-predicted (10%) as shown in

Fig. 5.1(f), and the maximum Stress-P_1 value is over-estimated by 22.1% with 129mmHg pressure loading (Fig. 5.1(f)). The effects of shrink-stretch process for 3D FSI models will be discussed in Chapter 9.

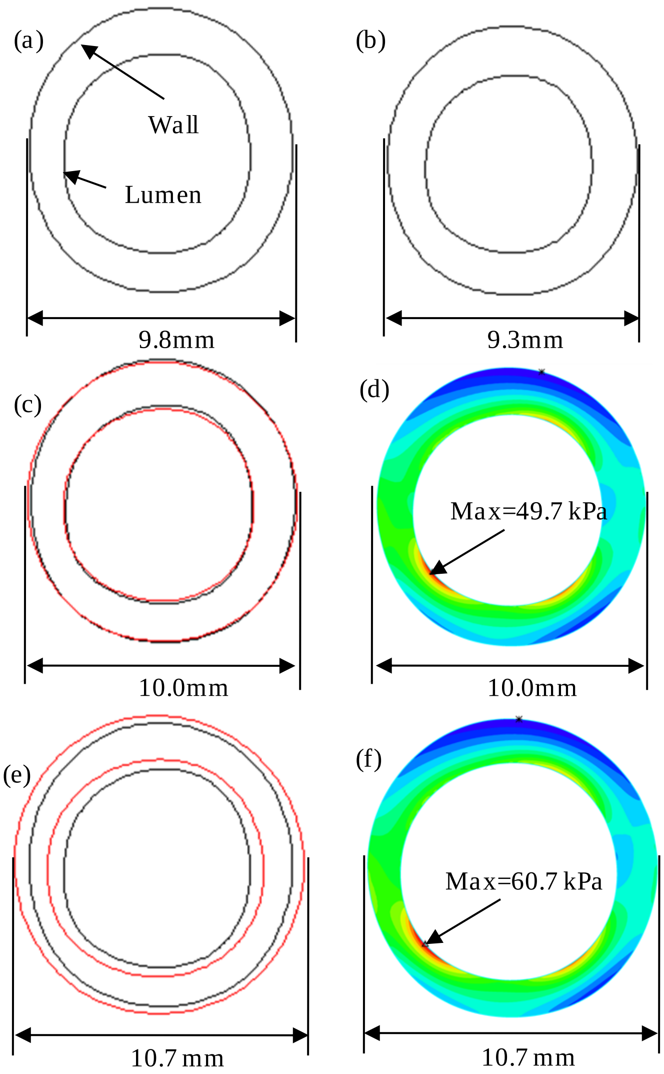

Figure 5.1. Shrink-stretch process has considerable impact on precision of simulation. (a) The in vivo 2D segmented contour (S1) of patient's plaque; (b) Shrunk contour used as numerical start shape; (c) Comparison between the pressurized contour start from shrunk contours (Red lines) and in vivo contours (Black lines); (d) Band plot of Stress-P_1 *simulation starts with shrunk contour; (e) Comparison between the pressurized contour(Red lines)start from non-shrunk contour (in vivo contour)and in vivo contour (Black lines); (f) Band plot of Stress-*P_1 *for non-shrunk contour.*

5.5 Pressure Condition

Pressure condition is one of the most important factors in determining the computational results. We believe including more patient-specific information in the computational model, will increase the accuracy of the assessment for plaque vulnerability. With this concern, patient-specific pulsating arterial pressure (Fig. 5.2) was imposed in the numerical simulations. The wave form was scaled with patient systolic pressure (p_s) and diastolic pressure (p_d) from the last hospital admission. Fig. 5.2 presents the pressure profile which was specified at the inlet (CCA) and the outlet (ICA and ECA).

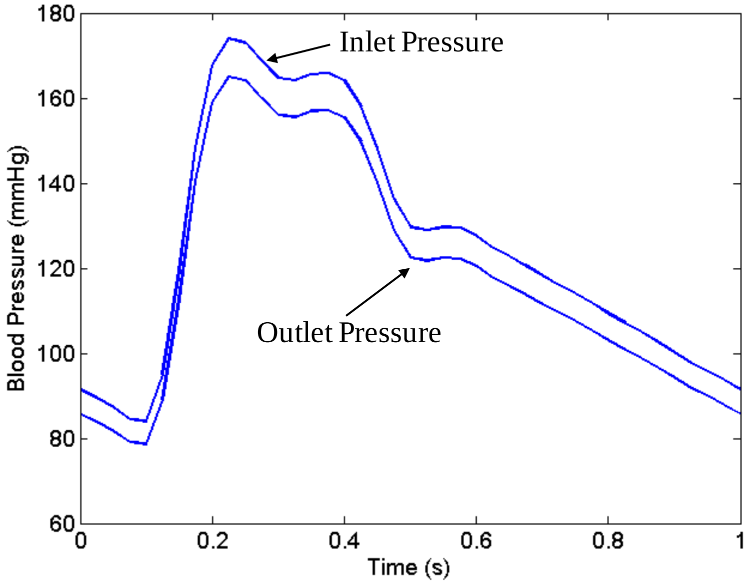

Figure 5.2. Patient-specific pulsatile blood pressure wave. In the multi-component plaque FSI model, the pressure was specified at the inlet (CCA) and outlet (ICA and ECA), where p_s *=174mmHg and* p_d *=84mmHg.*

6. Solution Methods and ADINA Package

The FSI models proposed in Chapter 5 were solved by a commercial software ADINA (Automatic Dynamic Incremental Nonlinear Analysis, ADINA R & D, Inc., Watertown, MA, USA) which provides a finite element program system to perform comprehensive finite element analysis of structures, heat transfer, fluids, and their interactions. For completeness, Section 6.1 briefly introduces the solution methods which are implemented in ADINA to solve fluid-structure interactions models. Section 6.2 gives a brief introduction on how to use ADINA package to perform the computation of fully coupled fluid flows with structure interactions. The theoretical frame can be found in reference [3-4].

6.1 Solution Method for the FSI Model

6.1.1 3D Finite Element Method for the Solid Model

Most structure part is meshed using 8-node hexahedral elements. Therefore, the 8-node hexahedral element will be used to illustrate the discretization process. Total Lagrangian incremental nonlinear finite element method will be used to solve solid model. The displacement-based method, which means all variables are expressed in terms of displacement, is introduced to establish the governing finite element equations.

For a 3D 8-node isoparametric displacement-based finite element (Fig. 6.1),

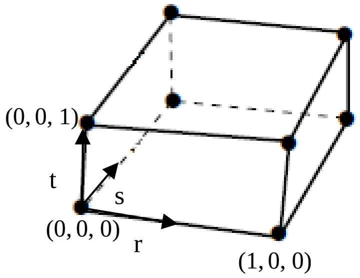

Figure 6.1 3D 8-node solid elements.

the interpolation functions h_i corresponding to node i are,

$$h_i(r,s,t) = G(r,r_i)G(s,s_i)G(t,t_i) \tag{6.1}$$

where $$G(\alpha,\alpha_i) = \begin{cases} \frac{1}{2}(1+\alpha_i\alpha) & if\ \alpha_i = 1 \\ 1-\alpha^2 & if\ \alpha_i = 0 \end{cases} \qquad \alpha = r,s,t \tag{6.2}$$

and r, s, t are isoparametric coordinates.

The coordinates and displacements are interpolated as,

$$x_h = \sum_{i=1}^{8} x_i\, h_i;\ \ y_h = \sum_{i=1}^{8} y_i\, h_i;\ z_h = \sum_{i=1}^{8} z_i\, h_i \tag{6.3}$$

$$v_{1h} = \sum_{i=1}^{8} v_{1i}\, h_i;\ \ v_{2h} = \sum_{i=1}^{8} v_{2i}\, h_i;\ v_{3h} = \sum_{i=1}^{8} v_{3i}\, h_i \tag{6.4}$$

where x_h, y_h, z_h are the coordinates and v_{1h}, v_{2h}, v_{3h} are displacements at any point of the element h and x_i, y_i, z_i are the coordinates of ith nodal point, and $v_{1i}, v_{2i}, v_{3i}, i = 1, \ldots, 8$ are the displacements of the element nodes i. For an element m, eqn. (6.4) can be rewritten in matrix form as,

$$\boldsymbol{v}^{(m)} = \boldsymbol{H}^{(m)}\boldsymbol{V} \tag{6.5}$$

where the superscript m denotes the mth element and $\boldsymbol{V}$ is a vector of global displacement components at all nodal points. Based on definition of strain (eqn. (5.7)), the strain vector can be described as,

$$\boldsymbol{\varepsilon}^{(m)} = \boldsymbol{B}^{(m)}\boldsymbol{V} \tag{6.6}$$

The columns of $\boldsymbol{H}^{(m)}$ and $\boldsymbol{B}^{(m)}$ consist of zero elements if they correspond to a degree of freedom not defined for element m.

Incremental generalized Hooke's law is used to deal with the non-linear material properties,

$$\boldsymbol{\sigma} = \boldsymbol{C}\boldsymbol{\varepsilon} \tag{6.7}$$

where $\boldsymbol{C}$ is the incremental material matrix, which is evaluated by further differentiation as,

$$\boldsymbol{C} = C_{\mathrm{ijrs}} = (\partial\sigma_{ij}/\partial\varepsilon_{rs} + \partial\sigma_{ij}/\partial\varepsilon_{sr})/2 \tag{6.8}$$

For a static problem, performing assemblage process, the virtual displacement theorem gives the equilibrium relations,

$$\sum_m \int_{V^{(m)}} \bar{\boldsymbol{\varepsilon}}^{(m)}\boldsymbol{\sigma}^{(m)}\, dV^{(m)} = \int_{V^{(m)}} \overline{\boldsymbol{V}}^{(m)}\boldsymbol{f}^{B^{(m)}}\, dV^{(m)} +$$

$$\sum_m \int_{S^{(m)}} \overline{\boldsymbol{V}}^{S^{(m)}}\boldsymbol{f}^{S^{(m)}}\, dS^{(m)} + \sum_i \overline{\boldsymbol{V}}^i\boldsymbol{F}^{iC} \tag{6.9}$$

where $\overline{\boldsymbol{V}}$ are the virtual displacements and $\boldsymbol{f}^B$ is external body forces, $\boldsymbol{f}^S$ is external surface tractions, and $\boldsymbol{F}^{iC}$ is concentrated load.

Using equations (6.5), (6.6), and (6.7), the governing finite element matrix equations can be obtained [p87-90, 5],

$$\boldsymbol{KV}=\boldsymbol{R}-\boldsymbol{F} \tag{6.10}$$

Where ***R*** is external load vector, ***F*** is concentrated load, matrix ***K*** is the stiffness matrix of the element assemblage.

In our study, the loads are time-dependent, the inertia forces need to be considered; i.e., a truly dynamic problem needs to be solved. Applying d'Alembert's principle, the element inertia forces can be simply included as part of the body forces. The dynamic equilibrium equations are lead to [p165, 3],

$$\boldsymbol{M}\ddot{\boldsymbol{V}} + \boldsymbol{KV} = \boldsymbol{R} - \boldsymbol{F} \tag{6.11}$$

where ***R***, ***F*** and ***V*** are time dependent, the matrix ***M*** is the mass matrix of structure.

Applying pseudo-steady-state assumption, which means that the system is in steady state at a discrete time point, the solution to the governing equilibrium conditions (eqn. (6.11)) will be obtained using modified Newton-Raphson iteration [p493, 3], for *i*=1, 2, 3,...,

$${}^{t+\Delta t}\boldsymbol{M}\ddot{\boldsymbol{V}}^{(i)} + {}^{t+\Delta t}\boldsymbol{K}\Delta\boldsymbol{V}^{(i)} = {}^{t+\Delta t}\boldsymbol{R} - {}^{t+\Delta t}\boldsymbol{F}^{(i-1)} \tag{6.12}$$

$${}^{t+\Delta t}\boldsymbol{V}^{(i)} = {}^{t+\Delta t}\boldsymbol{V}^{(i-1)} + \Delta\boldsymbol{V}^{(i)} \tag{6.13}$$

The latest estimates for the nodal point displacements are used to evaluate the corresponding element stresses and nodal point forces ${}^{t+\Delta t}\boldsymbol{F}^{(i-1)}$. The iteration will be repeated until convergence is obtained.

6.1.2 3D Finite Element Method for the Fluid Model

The governing equations for fluid model described in Chapter 5 can be rewritten as,

$$\rho\left(\frac{\partial u_i}{\partial t} + u_{i,j}\left(u_j - u_{gj}\right)\right) = \sigma_{ij,j} \quad \text{(Momentum)} \tag{6.14}$$

where $\sigma_{ij} = -p\delta_{ij} + 2\mu\varepsilon_{ij}$ (6.15)

$$u_{i,i} = 0 \text{ (Continuity)} \tag{6.16}$$

The finite element equations will be obtained by establishing a weak form of the governing equations using Galerkin method [4]. The momentum equations are weighted with the velocities, the continuity equation is weighted with pressure. By integrating over the computational domain *V*, and performing integration by parts, we obtain the following weak form of eqn. (6.14) & (6.16) [p677, 3],

$$\int_V \bar{u}_i \rho\left(\frac{\partial u_i}{\partial t} + u_{i,j}\left(u_j - u_{gj}\right)\right) dV + \int_V \bar{\varepsilon}_{ij}\sigma_{ij}\, dV = \int_{S_f} \bar{u}_i^S f_i^S\, dS \text{ (Momentum)} \tag{6.17}$$

where prescribed tractions f_i^S on the surface S_f,

$$\sigma_{ij} n_j |_{S_f} = f_i^S \tag{6.18}$$

$$\int_V \bar{p} u_{i,i} dV = 0 \text{ (Continuity)} \tag{6.19}$$

To employ the finite element methods for incompressible fluid flow analysis, the inf-sup condition should be satisfied [3, 6]. Let P_h be the finite element space of the pressures with $p_h \in \mathrm{P}_h$, $\boldsymbol{V}_h$ be the finite element space of the velocities with $\boldsymbol{v}_h \in \boldsymbol{V}_h$ (the subscript *h* denotes the element). Then the inf-sup condition is given by,

$$\inf_{p_h \in P_h} \sup_{v_h \in V_h} \frac{\int p_h \nabla \cdot v_h \; dV}{\left\| p_h \right\|_0 \left\| v_h \right\|_1} \geq \beta \geq 0 \tag{6.20}$$

where β is a mesh-independent constant [3]. If this condition is satisfied, the elements will be optimal for the velocity and pressure interpolations; that is, the numerical scheme will be stable. In this situation, 3D tetrahedral (4-node) Flow-Condition-Based-Interpolation (FCBI) elements will be employed. Fig. 6.2 shows a 4-node element. All variables are defined at the corner nodes while the center node 0 is an auxiliary node where only defines the velocity.

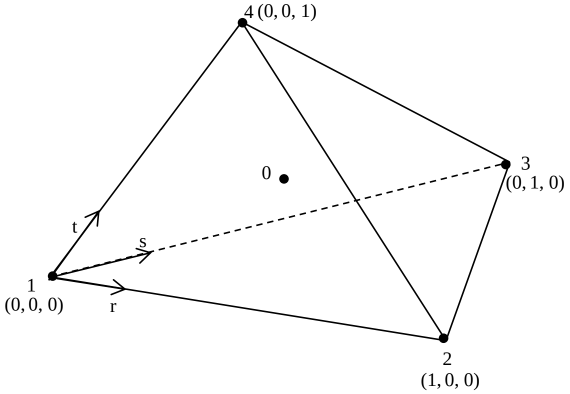

Figure 6.2 3D tetrahedral (4-node) FCBI elements using for Galerkin formulation.

The interpolation functions h_i corresponding to node i for 4-node tetrahedral element are,

$$h_1 = 1-r-s-t,\ h_2=4,\ h_3=s,\ h_4=t,\ h_0=h_1 h_2 h_3 h_4 \tag{6.21}$$

where r,s, and t are isoparametric coordinates. For an element, V_h, the solution variables are interpolated as,

$$p_h = \sum_{i=1}^{4} p_i \, h_i \tag{6.22}$$

$$\boldsymbol{u}_h = \sum_{i=0}^{4} \boldsymbol{u}_i \, h_i \tag{6.23}$$

where p_i stands for the nodal pressure and $\boldsymbol{u}_i$ denotes the nodal velocity.

Applying proper boundary conditions and assembling all elemental contributions together, the nonlinear finite elements equations for fluid model will be obtained [p678, 3],

$$\begin{bmatrix} \boldsymbol{M} & \boldsymbol{0} \\ \boldsymbol{0} & \boldsymbol{0} \end{bmatrix} \begin{bmatrix} \dot{\boldsymbol{U}} \\ \dot{\boldsymbol{P}} \end{bmatrix} + \begin{bmatrix} \boldsymbol{K} & \boldsymbol{K_p} \\ \boldsymbol{K_p^T} & \boldsymbol{0} \end{bmatrix} \begin{bmatrix} \boldsymbol{U} \\ \boldsymbol{P} \end{bmatrix} = \begin{bmatrix} \boldsymbol{R} \\ \boldsymbol{0} \end{bmatrix} \tag{6.24}$$

where $\boldsymbol{U}$ denotes vectors of global velocity and $\boldsymbol{P}$ lists all pressure at all nodal points, $\dot{\boldsymbol{U}}$ denotes the derivative of velocity with respect to time t, $\boldsymbol{R}$ is the load vector. Using Euler backward integration and Newton-Raphson iteration method to perform incremental analysis to obtain the solution iteratively by solving linearized algebraic equations, as follows [835, 3],

$$\left({}^{(t+\Delta t)}\begin{bmatrix} \boldsymbol{K} & \boldsymbol{K_p} \\ \boldsymbol{K_p^T} & \boldsymbol{0} \end{bmatrix}^{(\boldsymbol{i}-\boldsymbol{1})} + \frac{1}{\Delta t} \begin{bmatrix} \boldsymbol{M} & \boldsymbol{0} \\ \boldsymbol{0} & \boldsymbol{0} \end{bmatrix} \right) \begin{bmatrix} \Delta \boldsymbol{U}^{(i)} \\ \Delta \boldsymbol{P}^{(i)} \end{bmatrix} =$$

$$\begin{bmatrix} {}^{t+\Delta t}\boldsymbol{R} \\ \boldsymbol{0} \end{bmatrix} - \left(\begin{bmatrix} \boldsymbol{M} & \boldsymbol{0} \\ \boldsymbol{0} & \boldsymbol{0} \end{bmatrix} \begin{bmatrix} {}^{(t+\Delta t)}\dot{\boldsymbol{U}}^{(i-1)} \\ {}^{(t+\Delta t)}\dot{\boldsymbol{P}}^{(i-1)} \end{bmatrix} + {}^{(t+\Delta t)}\begin{bmatrix} \boldsymbol{K} & \boldsymbol{K_p} \\ \boldsymbol{K_p^T} & \boldsymbol{0} \end{bmatrix}^{(\boldsymbol{i}-\boldsymbol{1})} \begin{bmatrix} {}^{(t+\Delta t)}\boldsymbol{U}^{(i-1)} \\ {}^{(t+\Delta t)}\boldsymbol{P}^{(i-1)} \end{bmatrix} \right) \tag{6.25}$$

$$\begin{bmatrix} {}^{(t+\Delta t)}\boldsymbol{U}^{(i)} \\ {}^{(t+\Delta t)}\boldsymbol{P}^{(i)} \end{bmatrix} = \begin{bmatrix} {}^{(t+\Delta t)}\boldsymbol{U}^{(i-1)} \\ {}^{(t+\Delta t)}\boldsymbol{P}^{(i-1)} \end{bmatrix} + \begin{bmatrix} \Delta \boldsymbol{U}^{(i)} \\ \Delta \boldsymbol{P}^{(i)} \end{bmatrix} \tag{6.26}$$

6.1.3 Fluid-Structure Interactions

In FSI solving process, the fluid and solid equations will be solved individually at each time step. At each time step, the fluid model and solid model will solve individually using the latest information provided by the other part. Which means the fluid model will be solved with the latest displacement and velocity conditions provided by the solid part of the last time step. The obtained stress, pressure will be employed as boundary and loading condition for structure model for the next time step. These two steps will be repeated until the final time step is reached. This iterative FSI Coupling solution method requires less memory than the Direct FSI Coupling method. Therefore, iterative FSI coupling method is more adequate in our case.

6.2 ADINA Package

ADINA system has been used widely in many fields of application, including the automotive, aerospace, manufacturing, nuclear, and biomedical industries, civil engineering applications, and research. Especially, in real life, ADINA system has been tested by hundreds of applications and has been used by Tang to solve many FSI models [3-4, 60-61, 63, 66, 70-71].

The ADINA system offers a one-system program for comprehensive finite element analyses of structures, fluids, and fluid-structural interactions. The system consists of the following modules,

ADINA-AUI: The ADINA User Interface program (AUI) provides complete pre- and post-processing capabilities for all the ADINA solution programs.

ADINA-M: The ADINA Modeler (ADINA-M) is an add-on module to ADINA-AUI that provides solid modeling capabilities and direct integration with all other Parasolid-based CAD systems.

ADINA: The premium finite element program for linear and highly nonlinear analyses of solids and structures.

ADINA-F: Computational Fluid Dynamics (CFD) program for the analysis of compressible and incompressible flow with state-of-the-art capabilities for moving boundaries and automatic remeshing.

ADINA-T: Module for the heat transfer analysis of solids and field problems.

ADINA-FSI: The ADINA-FSI program is the leading code used by industries for fully coupled analysis of fluid flow with structural interactions problems.

ADINA-TMC: This module provides capabilities for thermo-mechanical coupled (TMC) analysis, including analysis of contact with heat transfer.

In this project, ADINA-FSI module was selected to analyze coupled fluid flow with structural interactions. A batch of programming commands was written into two input files (.in file) for the creation of structure and fluid models, respectively, and ADINA-AUI module was used to load these two .in files to generate .dat files for running ADINA-FSI program. The detail build up procedure are presented as follows.

6.3 Build-Up Procedure Using ADINA

6.3.1 Geometry Creation

The geometry consists of points, lines, surfaces, and volumes, which are generated under ADINA computing environment. The details of the procedure are described in Chapter 4.

6.3.2 Physical Model Generation

Physical properties, such as material properties, initial conditions and boundary conditions are necessary to be specified before the FSI simulation.

6.3.2.1 Material Properties Assignment

The physical properties were assigned to the geometry model directly.

Solid Model: The artery wall and plaque components were assumed to be hyperelastic, isotropic, incompressible and homogeneous. Different material properties can be assigned to each volume to reflect the complexity of biological tissues.

Fluid model: The blood flow was assumed to be laminar, viscous, incompressible and Newtonian.

6.3.2.2 Element Group Generation

Before generating elements, the element groups for solid and fluid model need to be defined. An element group can be regarded as a container for elements which share certain common attributes, e.g. material, kinematics formulation, numerical integration order, interpolation formulation, results output [4].

Solid Model: The 3D solid element groups with Mooney-Rivlin material model were used for describing the material properties of vessel wall and all components. The following material parameters values were chosen in this study to describe the material: Vessel wall/fibrous cap, c_1=36.8kPa, D_1=14.4kPa, D_2=2; Calcification, c_1=368kPa, D_1=144kPa, D_2=2.0; Lipid core/hemorrhage, c_1=2kPa, D_1=2kPa, D_2=1.5.

Fluid model: The density of the blood was assumed to $\rho = 1\ g \cdot cm^{-3}$ and the viscosity was assumed to be $0.04\ dyn \cdot cm^{-2}$.

6.3.2.3 Mesh Generation

After selecting the 3D element types (3D Solid/3D Fluid for solid/fluid model) for the volumes, the mesh density was assigned by specifying the proper numbers of division along the edges of volumes. Finer mesh were used for thin plaque cap, bifurcation and components with sharp angles to obtain better resolution and handle high stress concentration behaviors.

Numbers of volumes and elements used for this patient-specific models are: Normal (fibrous) tissue: volumes: 298, elements: 95,296; lipid core: volumes: 5, elements: 2688; Fluid: volumes: 30, elements: 315,648. Total volumes for the whole model: 333; total elements: 413,632.

6.3.2.4 Initial Conditions/Boundary Conditions

Solid model: Specified the inner boundary of vessel wall as the fluid-structure boundaries using ADINA command “FSBOUNDARY”. The blood vessel was tethered by the surrounding tissue at *in vivo* state. Therefore, we should add some constraints on the vessel wall. Prescribed displacement, which was defined by shrinkage rate of blood vessel, was specified to the surfaces at inlet and outlet position to apply loading using the command “Load Displacement”.

Fluid model: Specified the outer boundary of the fluid domain as the fluid-structure boundaries. Flow velocity at the flow-vessel interface was set to move with vessel wall (non slip condition). The pressure conditions were specified at inlet (CCA) and outlet (ICA and ECA). In this study, patient-specific pulsating arterial pressure (Section 5.5) was imposed.

6.3.2.5 Analysis Control

Additionally, the following control data are needed for a successful FSI simulation,

1) Master degrees of freedom: In this project, we provide only X-translation, Y-translation, Z-translation degrees of freedom, while rotation is prohibited.

2) Time function: The time function is used for applying time-dependent loads or gradually increasing loads.

3) Time step: The time step sequence is assigned to control the time/load-step increment. The assignment of time step should satisfy Courant–Friedrichs–Lewy condition (CFL condition).

4) Solution control variables: The iteration method, maximum number of iterations, iteration tolerance, and the output information are all necessary.

7. Validation of ADINA Software and Computational Models

Computational models and software need to be validated so that they can be used to make reliable predictions. In this chapter, validation results for the commercial software package ADINA and our computational 3D FSI models are provided by comparing (1) the analytic solutions with numerical solutions obtained by ADINA and (2) computational results from 3D FSI model with the experimental data[*]. Details are given below.

7.1 Validation of ADINA Software by Analytic Solutions

Two hydrodynamic models having analytical solutions were used to validate the software. Both models are simplified versions of our full 3D models.

7.1.1 A Steady Flow in a Cylindrical Tube

7.1.1.1 Analytical Solution

Let us consider an incompressible steady flow in a uniform rigid tube with length L and inner radius r as shown in Fig. 7.1 (L>> r). The gravitational effect (a body force) was ignored.

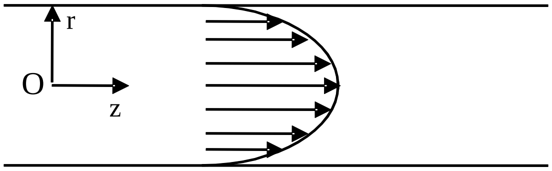

Figure 7.1. Laminar flow in a cylindrical tube.

In cylindrical coordinate system, considering the symmetry, the Navier-Stokes equation is simplified as,

---

[*] The experimental results reported here was done by Prof. Tang's group, and published in 2003, 2004 [38, 39, 63, 71].

$$0 = -\frac{\partial p}{\partial r} \tag{7.1}$$

$$0 = -\frac{1}{r}\frac{\partial p}{\partial \theta} \tag{7.2}$$

$$0 = -\frac{\partial p}{\partial z} + \eta\left[\frac{1}{r}\frac{\partial}{\partial r}\left(\frac{r\partial u}{\partial r}\right)\right] \tag{7.3}$$

where p is the pressure, u is the velocity, η is viscosity of fluid. The continuity condition requires,

$$\frac{\partial \mathrm{u}}{\partial z} = 0 \tag{7.4}$$

Applying non slip boundary conditions, the model has a solution

$$u = -\frac{dp}{dz}\frac{(R^2 - r^2)}{4\eta} \tag{7.5}$$

This is the famous parabolic velocity profile of the Hagen-Poiseuille flow [19, 47].

7.1.1.2 Comparison between Numerical and Analytical Solutions

A fluid flow through a rigid tube of length 10 cm, radius 0.3cm was considered. The flow is assumed to be laminar, viscous, incompressible and Newtonian. The viscosity of the fluid is 4×10^{-3}N·s/m^2, and the pressure gradient $\frac{dp}{dZ}$ is set to be 0.0625 mmHg/cm. The incompressible Navier-Stokes equations are used as governing equations. The simulation was performed using ADINA.

Mesh analysis was performed first to obtain numerical solutions which are mesh-independent and to determine mesh size to be used in the validation. The baseline element edge length in radius and longitudinal directions was set as 0.05cm. The element edge lengths of Mesh 2 and Mesh 3 in radial direction were decreased to 0.025 and 0.0125 cm. Flow velocity (**v**) values (at θ=0, z=5) corresponding to different r positions for the three meshes are listed in Table 7.1. The differences between solutions from Mesh 1 and Mesh 2, and from Mesh 2 and Mesh 3 are

0.19% and 0.05%, respectively, as measured by l_2-norm. Therefore the solution is mesh-independent. We also tried tubes of different length (length=20 cm, 40 cm) with the same pressure gradient. No difference in the velocity prediction was found.

Points	1	2	3	4	5	6	7
r (cm)	0.00	0.05	0.10	0.15	0.20	0.25	0.30
Mesh 1: Edge length=0.05	45.76	44.08	40.31	34.01	25.19	13.85	0.00
Mesh 2: Edge length=0.025	45.45	44.08	40.31	34.01	25.19	13.85	0.00
Mesh 3: Edge length=0.0125	45.37	44.08	40.31	34.01	25.19	13.85	0.00

Table 7.1 Comparison of solutions from three meshes.

Using the baseline mesh (Mesh 1), comparison between numerical velocity $\mathbf{v}_n$ and analytical velocity $\mathbf{v}_a$ is presented in Table 7.2 and Fig. 7.2. The obtained l_2-norm of $\mathbf{v}_n$ and $\mathbf{v}_a$ are 18.10 and 18.66, respectively. The relative error is 3.01% obtained by using the formula as follows,

$$error = \frac{\|\mathbf{v}_n - \mathbf{v}_a\|_2}{\|\mathbf{v}_a\|_2} \times 100\% \tag{7.6}$$

The numerical solutions match analytical solutions very well.

Points	1	2	3	4	5	6	7
r (cm)	0.00	0.05	0.10	0.15	0.20	0.25	0.30
Analytical velocity (cm/s)	46.87	45.57	41.66	35.15	26.04	14.32	0.00
Numerical velocity (cm/s)	45.76	44.08	40.31	34.01	25.19	13.85	0.00

Table 7.2 Comparison of velocity profiles between numerical solution and analytical solution.

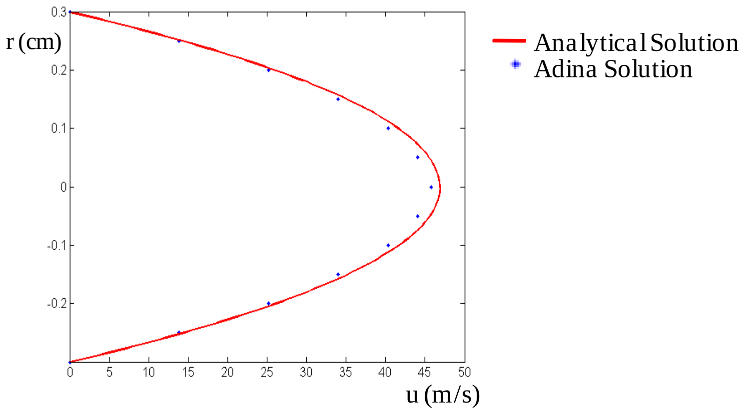

Figure 7.2. Numerical velocity profiles of a Poiseuille flow showing good agreement with analytical results.

7.1.2 Unsteady Flow in Thin Elastic Cylindrical Tube

Pulsatile flow in a uniform, long and thin elastic tube was chosen to validate the precision of computational results obtained under ADINA environment. The analytic solution for the velocity and wall motion can be obtained with Womersley theory [47, 75, 78]. The theoretical frame is introduced briefly in the following sections.

7.1.2.1 Fluid and Solid Models

Assume the wall is thin and composed of elastic, isotropic and homogeneous material. Under pulsatile loading condition, the wall deformation is small. With the above assumptions, the equations for wall motion are given by

$$\rho H \frac{\partial^2 \xi}{\partial t^2} - p + \frac{Eh}{1-\sigma^2}\left(\frac{\sigma}{R}\frac{\partial \xi}{\partial z} + \frac{\xi}{R^2}\right) + 2\eta\left(\frac{\partial v}{\partial r}\right)_{r=R} = 0 \tag{7.7}$$

$$\rho H \frac{\partial^2 \zeta}{\partial t^2} + \rho H \zeta \omega^2 - \frac{Eh}{1-\sigma^2}\left(\frac{\partial^2 \xi}{\partial z^2} + \frac{\sigma}{R}\frac{\partial \xi}{\partial z}\right) + \eta\left(\frac{\partial u}{\partial r} + \frac{\partial v}{\partial z}\right)_{r=R} = 0 \tag{7.8}$$

in which ξ is radial displacement, ζ is the longitudinal displacement, *E* is Young's modulus, and σ and *H* are Poisson's ratio and thickness of the wall, respectively, *p* is the pressure, ω is the circular frequency of the oscillation.

Assume the fluid is laminar, incompressible, viscous and Newtonian flow. Navier-Stokes equations using cylindrical coordinate system was employed as the governing equations of fluid model.

The following assumptions were added to simplify the models.

1) The translation accelerations $u\frac{\partial u}{\partial z}+v\frac{\partial u}{\partial r}$, $u\frac{\partial v}{\partial z}+v\frac{\partial v}{\partial r}$ are much smaller than translation acceleration $\frac{\partial u}{\partial t}$, and $\frac{\partial v}{\partial t}$ respectively. Therefore, the nonlinear translation accelerations can be omitted.
2) The radius of vessel is much less than pulse wavelength, that is

$$\frac{\omega^2 R^2}{c^2}=\frac{4\pi^2 R^2}{\lambda^2}\ll 1 \tag{7.9}$$

where R is radius of vessel, c is pulse wave velocity, λ is pulse wavelength. Based on this assumption, $\frac{\partial^2 u}{\partial z^2}$, and $\frac{\partial^2 v}{\partial z^2}$ can also be omitted.

The obtained linear Navier-Stokes equations are as follows,

$$\frac{\partial u}{\partial z}+\frac{1}{r}\frac{\partial rv}{\partial r}=0 \tag{7.10}$$

$$\frac{\partial u}{\partial t}=-\frac{1}{\rho}\frac{\partial P}{\partial z}+\frac{\eta}{\rho}\left(\frac{\partial^2 u}{\partial r^2}+\frac{1}{r}\frac{\partial u}{\partial r}\right) \tag{7.11}$$

$$\frac{\partial v}{\partial t}=-\frac{1}{\rho}\frac{\partial P}{\partial r}+\frac{\eta}{\rho}\left(\frac{\partial^2 v}{\partial r^2}+\frac{1}{r}\frac{\partial v}{\partial r}-\frac{v}{r^2}\right) \tag{7.12}$$

where u is the longitudinal velocity and v is radial velocity, *p* is pressure, ρ is density and η is viscosity of fluid, t stands for time.

In large tube, Womersley number α is larger than 1, according to assumption 2), we have

$$\frac{\omega^2 R^2}{c^2} \ll \alpha^2 \tag{7.13}$$

Using equation (7. 9) & (7. 13), the blood wall motion equations can be simplified as following,

$$\rho H \frac{\partial^2 \xi}{\partial t^2} = \frac{p}{H} + \frac{Eh}{H(1-\sigma^2)} \left(\frac{\sigma}{R} \frac{\partial \xi}{\partial z} + \frac{\xi}{R^2} \right) \tag{7.14}$$

$$\rho \frac{\partial^2 \zeta}{\partial t^2} = \frac{Eh}{H(1-\sigma^2)} \left(\frac{\partial^2 \xi}{\partial z^2} + \frac{\sigma}{R} \frac{\partial \xi}{\partial z} \right) - \frac{\eta}{H} \left(\frac{\partial u}{\partial r} \right)_{r=R} - \frac{K}{H} \zeta = 0 \tag{7.15}$$

where $K = \rho H \omega^2$.

Non slip conditions was employed at vessel wall, in addition, considering the symmetry of flow at the centre of the tube (r=0), the boundary conditions were given as follows,

$$\frac{\partial \zeta}{\partial t} = u|_{r=R} \tag{7.16}$$

$$\frac{\partial \xi}{\partial t} = v|_{r=R} \tag{7.17}$$

$$v|_{r=o} = 0 \tag{7.18}$$

$$\frac{\partial u}{\partial r}|_{r=0} = 0 \tag{7.19}$$

7.1.2.2 Comparison of Analytical and Numerical Solutions

To validate numerical solution, velocity profile was selected to be investigated. Here is an illustration. We considered the fluid flow through an elastic tube of length 10 cm, outer radius 0.4 cm, thickness 0.05cm. The viscosity of the fluid is 4×10^{-3}N·s/m^2, the density of the fluid is 1 g/cm^3, and the fluid flow is governed by the given pressure (Fig. 7.3) at the ends of the tube.

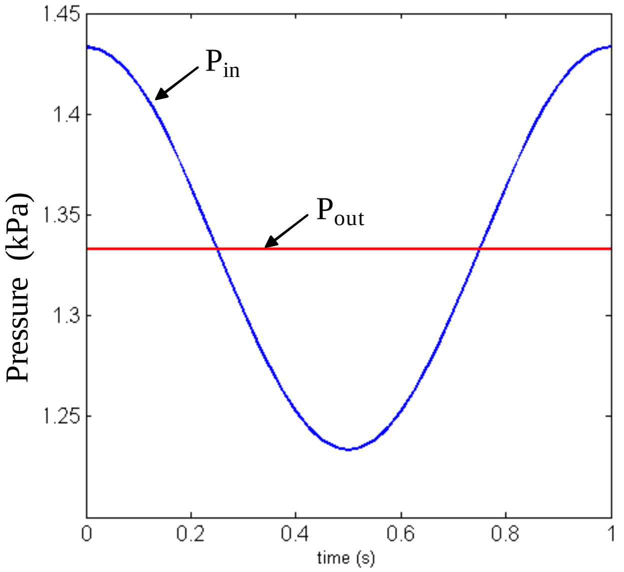

Figure 7.3. Pressure conditions specified at the inlet and outlet used in the FSI model. The inlet pressure is given by $P_{in}=(1.33+0.1\cos(2\pi t))$ *kPa; The outlet pressure is given by* $P_{out}=1.33$*kPa.*

The analytical solution of flow velocity in longitudinal direction in this problem is [77],

$$u = \frac{A^{*}R^{2}}{i\alpha^{2}\eta}\left[1-\frac{J_0(\alpha y\, i^{3/2})}{J_0(\alpha i^{3/2})}\right]e^{i\omega t} \tag{7.20}$$

where $\alpha = R\sqrt{\frac{\omega\rho}{\eta}}$ is Womersley number; y is fractional radius, y=r/R; J_0 is a Bessel function of the first kind of order zero and complex argument; A^* is defined in $\frac{\partial p}{\partial z} = A^{*}e^{i\omega t}$; $\omega=\frac{2\pi}{T}$ is the angular frequency in radian/sec of the oscillatory motion, with T the period. The comparison between analytical and numerical solution is given in Fig. 7.4, and the average value of relative error is less than 10%.

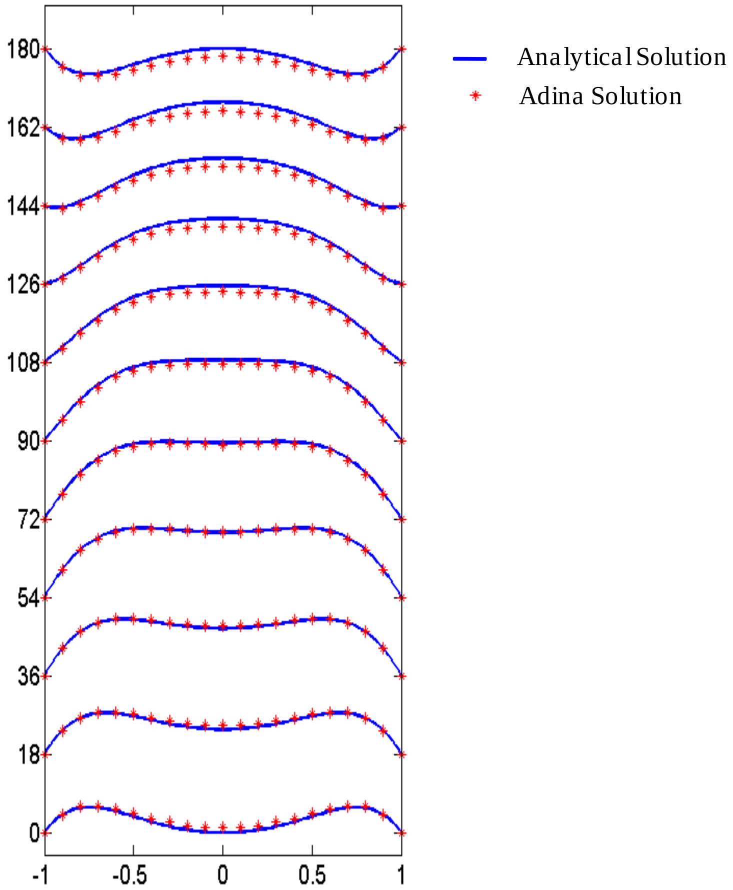

Figure 7.4. Numerical velocity profiles of a periodically pulsatile blood flow in an elastic cylindrical tube matches analytical results well. Profiles are plotted for phase angle steps of $\Delta\omega t=18^{o}$.

7.2 Validation of Computational FSI Model by Experimental Data [38-39, 63, 71]

Prof. Tang's group has introduced a series of experimental and computational models to investigate blood flow in stenotic arteries [38-39]. The experimental data has been compared with numerical results for validation [63, 71]. Straight PVA hydrogel tubes, whose mechanical properties are close to human carotid arteries, with stenosis were used to simulate the atherosclerotic carotid artery (Fig. 7.5). Steady flow was perfused through the stenosis tube.

Two constant head reservoirs were settled for the upstream and downstream pressures. The working fluid used was water at room temperature. Sagittal and cross section images were recorded by duplex ultrasound scanning for comparison.

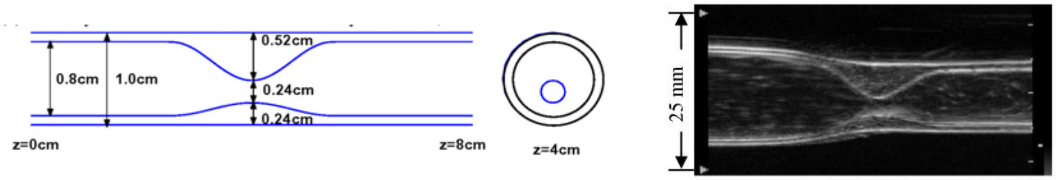
(a) The Asymmetric Stenotic Tube, S0=70%, Ecc=50%

(b) Ultrasound Image of the Deformed Stenotic Tube

Figure 7.5. The asymmetric stenotic tube geometry [63, 71].

7.2.1 Determination of Material Parameters

Uniaxial stretch test and compression testing were conducted to measure the material properties of the PVA hydrogel. A solid cylindrical rod (80mm long with 10 mm diameter) made of the same PVA hydrogel was used for stretch test. The rod was stretched from λ=1 to λ=1.4, where λ is stretch ratio and relaxed with the speed of 33 mm/min. In the compression test, the cylindrical PVA hydrogel rod was compressed from λ=1 to λ=0.6 and relaxed with the speed of 9.2 mm/min. Test was repeated several times and data were averaged for better accuracy. Stress/stretch relations for both positive and negative stress portions are presented in Fig. 7.6. To describe the material, the 3D Mooney-Rivlin model is selected (Section 5.2). The parameters, c_1=4.6 kPa, c_2=0, D_1=3 kPa, D_2=2.0 were chosen, the agreement with experimental stress/strain relations is good (Fig. 7.6). This agreement indicates that Mooney-Rivlin model with the selected parameters are good choices for wall material.

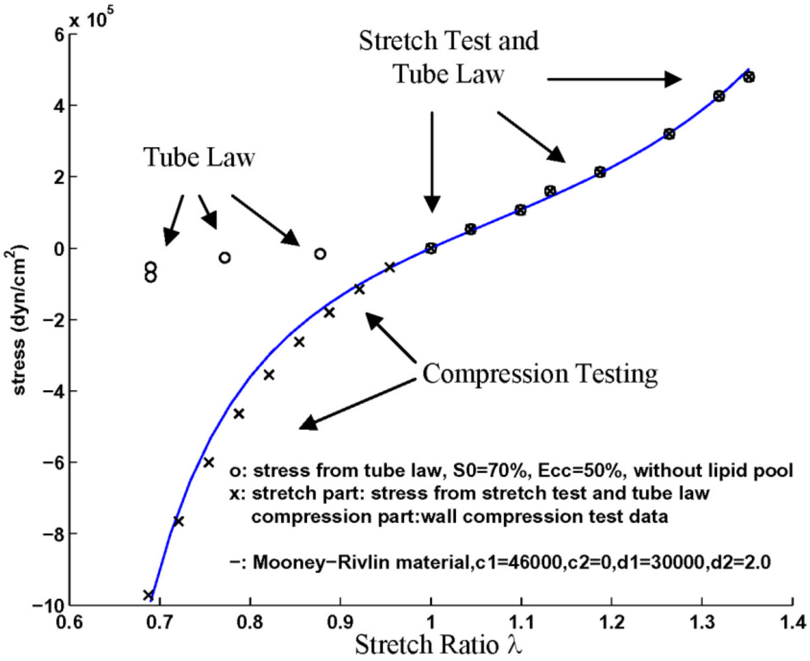

Figure 7.6. Mooney-Rivlin material curve matches experimental stress/strain relations well.

7.2.2 Comparison for Wall Deformation

In vitro experiments were conducted using PVA tube with a 70% stenosis and 50% eccentricity under 100 mmHg upstream pressure and the downstream pressure decreased from 90 to 0 mmHg to observe and quantify wall deformation. Ultrasound images were digitized to be compared with numerical results. Comparison of numerical and experimental results of tube inner shape under three different pressure conditions is given by Fig. 7.7. The agreement is good.

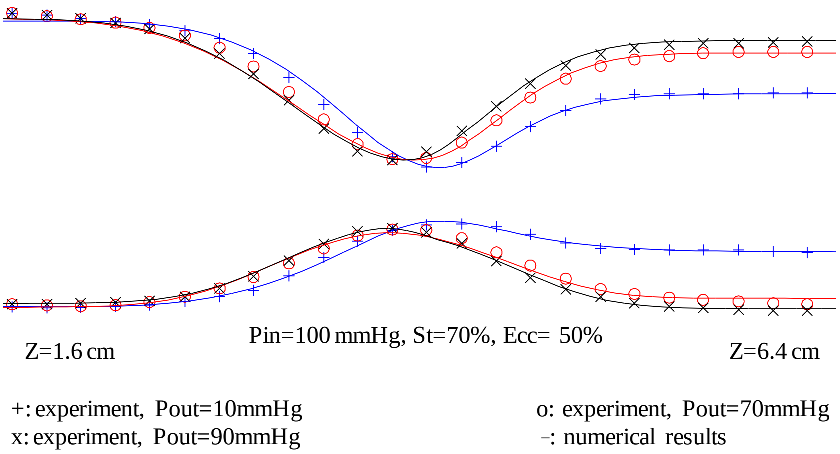

Figure 7.7. Validation: Comparison of numerical and experimental results for wall deformation.

7.2.3 Comparison of Flow Rate

Flow rates were measured experimentally under two sets of pressure conditions with two stenosis severities: the inlet pressure is 70 mmHg and 100 mmHg and the outlet pressure varies from 70 to 0 and 100 to 0 mmHg with increments of 10 mmHg. The stenosis is 70% and 75% respectively with 50% eccentricity. Numerical simulations were performed and compared with experimental data shown in Fig. 7.8. The difference between numerical data and experimental results for flow rate were less than 5%.

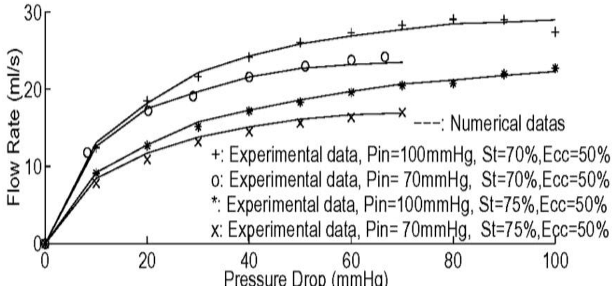

Figure 7.8. Validation: Computational flow rate (4 sets of data) show very good agreement with experimental measurements.

7.3 Conclusion

In this chapter, a steady and laminar flow through a rigid tube, a pulsatile flow through an elastic tube, and experimental results of wall deformation and flow rate with stenosis tube were introduced to validate proposed FSI models solved using ADINA package. The results indicate that ADINA package is capable of dealing with FSI problems with acceptable errors compared with analytic solutions and experimental measurements.

Part IV. Results

8. Quantifying Vessel Material Properties

8.1 Introduction

It should be noted that in order for a computational human carotid plaque model to be physiologically realistic and its results to bear biological relevance and significance, it is necessary to use real human carotid plaque material properties [56]. Dr. Tang's studies demonstrate that stiffness variations of plaque components (50% reduction or 100% increase) may affect maximal stress values by 20-50% [69]. Therefore, material property of an atherosclerotic artery is critical for the accuracy of computational models. However few can be found from the current literatures, which provide sufficient information that can be employed in the 3D FSI computational model. In this chapter, a method using MRI images under *in vitro* pressurized conditions and Least Squares Approximation Method is introduced to determine vessel material parameters. 3D MRI-based FSI computational models were used to evaluate the effects of material properties on flow and wall stress/strain behaviors. The results in this chapter have been reported in [33-34].

Using MRI will minimize the trauma to the specimen. To our knowledge, this is the first attempt to quantify vessel mechanical properties using MRI images and incorporate that with 3D FSI modeling to perform mechanical analysis. The procedure has the potential to be implemented under *in vivo* condition for non-invasive measurement of material properties and assessment of plaque vulnerabilities.

8.2 MRI data acquisition, Method and Model

8.2.1 Data Acquisition under Pressurized Condition

MRI data was obtained by Dr. Zheng’s group using protocol approved by Washington University Institutional Review Board with informed consent obtained where applicable. Fresh specimens were obtained from the autopsy division of the Department of Pathology. MRI study was conducted immediately after obtaining the specimens. The specimen was connected to both the insertion catheters of the newly assembled pressure phantom (Fig. 8.1) and tied with suture thread. The artery was not stretched along the vessel axis, or along the radial direction. A flow circulation was added to allow blood mimicking fluid (Model 046, CIRS Tissue Simulation & Phantom Technology, Norfolk, Virginia) to circulate the artery specimen. The inner pressure, which can be changed, was induced by air compression through a syringe.

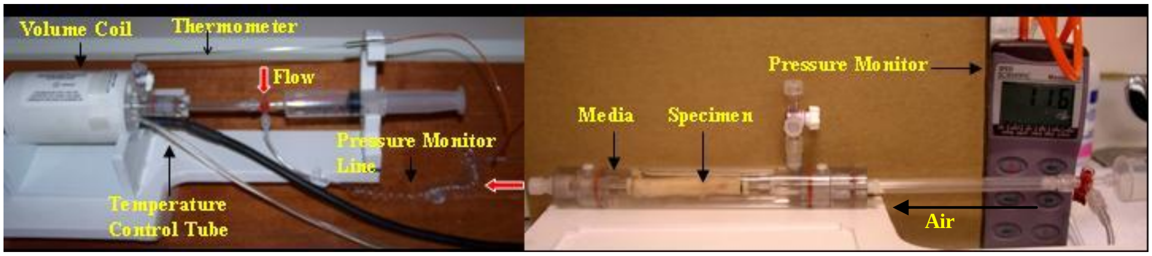

(a) The *in vitro* setup of plaque-phantom, side view. (b) Closer detailed view.

Figure 8.1. View of the MR compatible specimen chamber. The vessel specimen was mounted on cannulas and pressurized to desired pressure. The cannula on each side was connected to an end cap that can be connected to a long plastic tube with fluid flow. (a) side view; (b) closer detailed view;

MRI study was performed by using a small volume coil with a diameter of 3.5 cm in a 3 Tesla clinical MR system (Algrea, Siemens Medical Solution, Erlangen, Germany). Five MR imaging sessions under different pressure conditions (no flow) were obtained. Each imaging session involved multi-contrast (T1, T2, and PD) MRI imaging that included conventional spin-echo data acquisition along the cross sections of the artery. Each 3D MRI data set consisted of 24 2D slices with high resolution (FOV=28×28 mm^2, matrix size: 512×512; resolution: 0.055×0.055 mm^2; slice thickness = 1 mm). Fig. 8.2 gives the MR images of a selected slice (slice 12) under 5 pressure conditions and reconstructed 3D geometry of the specimen.

(a) MR image (slice 12) of a coronary artery segment under 5 pressure conditions

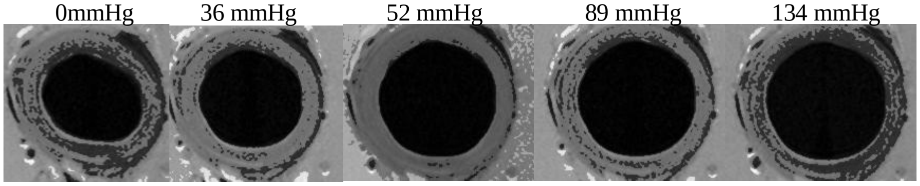

(b) Reconstructed 3D geometry of the sample vessel

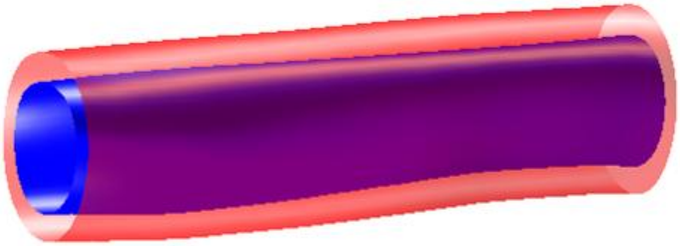

Figure 8.2. Ex vivo 2D MRI image of human carotid artery and 3D reconstruction. (a) MR images (slice 12) of a coronary artery segment under 5 pressure =0, 36, 52, 89, 134 mmHg; (b) Reconstructed 3D geometry of the sample vessel.

Segmentation was done to get the lengths of inner and outer boundaries by a self-developed software package Atherosclerotic Plaque Imaging Analysis (APIA) written in Matlab (MathWorks, MATLAB, Natick, MA).

8.2.2 Parameter Determination of Mooney-Rivlin Model

The 3D non linear modified Mooney-Rivlin (M-R) model was selected to describe the material properties of the vessel wall and plaque components. The strain energy density function was given by eqn. (5.8), where c_i, D_i are material parameters to be chosen to match MRI measurements.

The Least-Squares Approximation Method is used to find the proper parameters for M-R model to fit the MRI data obtained under 5 pressure conditions. The relationship between the circumferential wall stress and the flow pressure can be derived from the Laplace law [20],

$$p=\mathrm{T}/\mathrm{r}, \tag{8.1}$$

$$\mathrm{T}= \sigma \mathrm{h}, \tag{8.2}$$

$$\sigma = p\mathrm{r}/\mathrm{h}, \tag{8.3}$$

where T is tension in the arterial wall, σ is the mean circumferential stress, p is pressure, h is the tube wall thickness, r is the average vessel radius. Based on MR images (Fig. 8.2) under different pressure (slice 12 was selected), vessel radii were obtained approximately by using inner and outer perimeters since the vessel was not axis-symmetric,

$$\mathrm{r}_{\mathrm{in}}=\mathrm{C}_{\mathrm{in}}/2\pi \tag{8.4}$$

$$\mathrm{r}_{\mathrm{out}}=\mathrm{C}_{\mathrm{out}}/2 \tag{8.5}$$

$$\mathrm{r}_{\mathrm{av}}=(\mathrm{r}_{\mathrm{in}}+\mathrm{r}_{\mathrm{out}})/2 \tag{8.6}$$

$$\mathrm{h}= \mathrm{r}_{\mathrm{out}} - \mathrm{r}_{\mathrm{in}} \tag{8.7}$$

$$\lambda= \mathrm{r}/\mathrm{r}_1 \tag{8.8}$$

Circumferential stress σ_i (i=1,2, …, 5) corresponding to each pressure condition p_i was obtained using eqn. (8.3), vessel radius and wall thickness were determined using eqn. (8.4)-(8.7).

The uni-axial stress/stretch relation for an isotropic material is obtained from eqn. (5.8) [3-4, 20],

$$\sigma = \frac{\lambda \partial W}{\partial \lambda} = c_1(2\lambda^2 - 2\lambda^{-1}) + c_2(2\lambda - 2\lambda^{-2}) + D_1 D_2 (2\lambda^2 - 2\lambda^{-1}) e^{D_2(\lambda^2+2\lambda^{-1}-3)} \tag{8.9}$$

where σ is the uni-axial Cauchy stress, λ is the stretch ratio.

A parameter-reduction procedure was used to determine the four parameters in eqn. (8.9) so that the predicted stress-stretch curve would have a "best fit" to the MRI-measured data set $\{(\sigma_i, \lambda_i), i=1,\ldots,5)$. According to our past experience, c_2 was set to zero. Then for each fixed D_2 value, the Least-Squares Approximation Method was used to determine c_1 and D_1. Let,

$$X_1 = 2\lambda^2 - 2\lambda^{-1} \tag{8.10}$$

$$X_2 = D_2(2\lambda^2 - 2\lambda^{-1})e^{D_2(\lambda^2+2\lambda^{-1}-3)} \tag{8.11}$$

eqn. (8.9) leads to

$$\sigma^* = c_1X_1 + D_1X_2 \tag{8.12}$$

Define the error function,

$$f(c_1, D_1) = \sum_{i=1}^{n}(\sigma_i^* - \sigma_i)^2 = \sum_{i=1}^{n}(c_{1i}X_{1i} + D_{1i}X_{2i} - \sigma_i)^2 \tag{8.13}$$

where σ_i was calculated from eqn. (8.3). Least- Squares Approximation Method is used to find the parameters to minimize the function *f*. The minimum value of *f* occurs when all partial derivatives are simultaneously zero, that is,

$$\begin{cases} \dfrac{\partial f}{\partial c_1} = 2\sum_{i=1}^{n} X_{1i}\left(c_1X_{1i} + D_1X_{2i} - \sigma_i\right) = 0 \\ \dfrac{\partial f}{\partial D_1} = 2\sum_{i=1}^{n} X_{2i}\left(c_1X_{1i} + D_1X_{2i} - \sigma_i\right) = 0 \end{cases} \tag{8.14}$$

Hence, the best parameters were chosen by solving the equations,

$$\begin{cases} c_1\sum_{i=1}^{n} X_{1i}^2 + D_1\sum_{i=1}^{n} X_{1i}X_{2i} = \sum_{i=1}^{n} X_{1i}\sigma_i \\ c_1\sum_{i=1}^{n} X_{1i}X_{2i} + D_1\sum_{i=1}^{n} X_{2i}^2 = \sum_{i=1}^{n} X_{2i}\sigma_i \end{cases} \tag{8.15}$$

For D_2 values from 0.5 to 12 with 0.1 increments, we got c_1, D_1 parameters from each D_2 value.

Fig. 8.3(a) shows the errors have no significant change with different D_2, which indicates that for different D_2 values, c_1 and D_1 can be chosen to get about the same approximation level as measured by the errors. A parameter value set was chosen (c_1= -47.1 kPa, D_1=40.9 kPa, D_2=2.0) which gives the best fit to the (σ_i , λ_i) data set. The obtained parameter will be further used for 3D FSI model based on the MR images. The predicted deformation will be compared with the MR Image with the same pressure loading and the values of parameters will be adjusted until the best match is obtained. Finally, the parameters were chosen to be c_1=-31.8kPa, D_1=27.6 kPa, D_2=2.0. Fig. 8.3(b) shows the stress-stretch curve fitting MRI data and errors from the 3D FSI model. Tube radii and errors are given in Table 8.1.

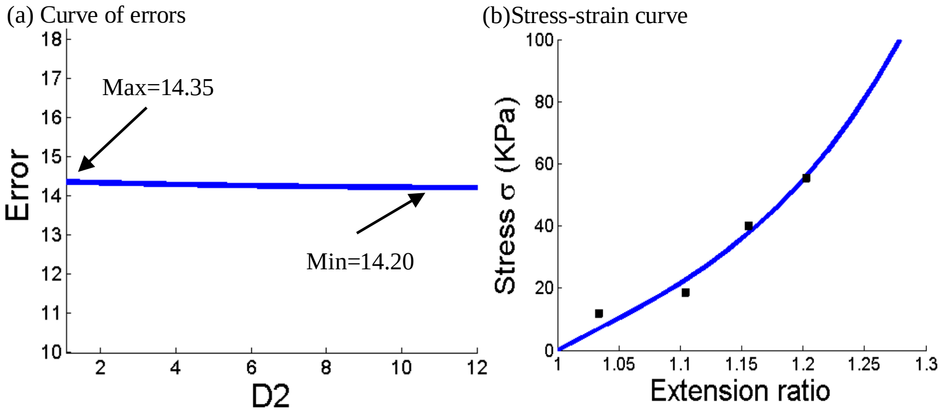
(a) Curve of errors

(b)Stress-strain curve

Figure 8.3. The Curve of errors from Least Squares Methods under different D_2 values and Stress-stretch curve derived from the M-R model using 3D FSI model has good agreement with MRI data.

Pressure	P1	P2	P3	P4	P5
R_{MRI} (cm)	0.2957	0.3061	0.3267	0.3422	0.3565
R_{FSI} (cm)	0.2957	0.317	0.3256	0.342	0.3567
Rel Error %	0	3.54	-0.33	-0.04	0.05

Table 8.1. Radii and errors from the 3D FSI model using adjusted material curve. R_{MRI} is the average radius; R_{FSI} is the radius obtained using the 3D FSI model.

8.3 Effects of Material Stiffness

Simulations were conducted using 3D MRI-based FSI model to investigate the effects of material properties on flow and stress/strain characteristics. It is essential to perform sensitivity analysis of the material parameters included in the Mooney-Rivlin model. Starting from baseline model, c_1 and D_1 values were doubled from Case 0 (c_1=-31.8 kPa, D_1=27.6 kPa, D_2=2.0) to Case 10 (c_1= -63.4 kPa, D_1=55.2 kPa, D_2=2.0) in 10 even steps with about 100% stiffness increase. The pressure conditions for all cases were set as follows: upstream pressure p_{in}=110 mmHg, downstream pressure p_{out} =109mmHg. The corresponding flow rate was 17.53 ml/s for Case 0. Band plots of flow max-shear-stress (MSS) and structure maximum principal stress/strain distributions (Stress-P_1/Strain-P_1) are shown in Fig. 8.4. When stiffness increased 100%, maximum values of Stress-P_1 decreased by 22.2%; maximum values of Strain-P_1 decreased by 40.5%. While changes in flow characteristics were much less noticeable: MSS was decreased by 2.37%, maximum flow velocity was decreased by 8.18% due to higher resistance from a narrower vessel.

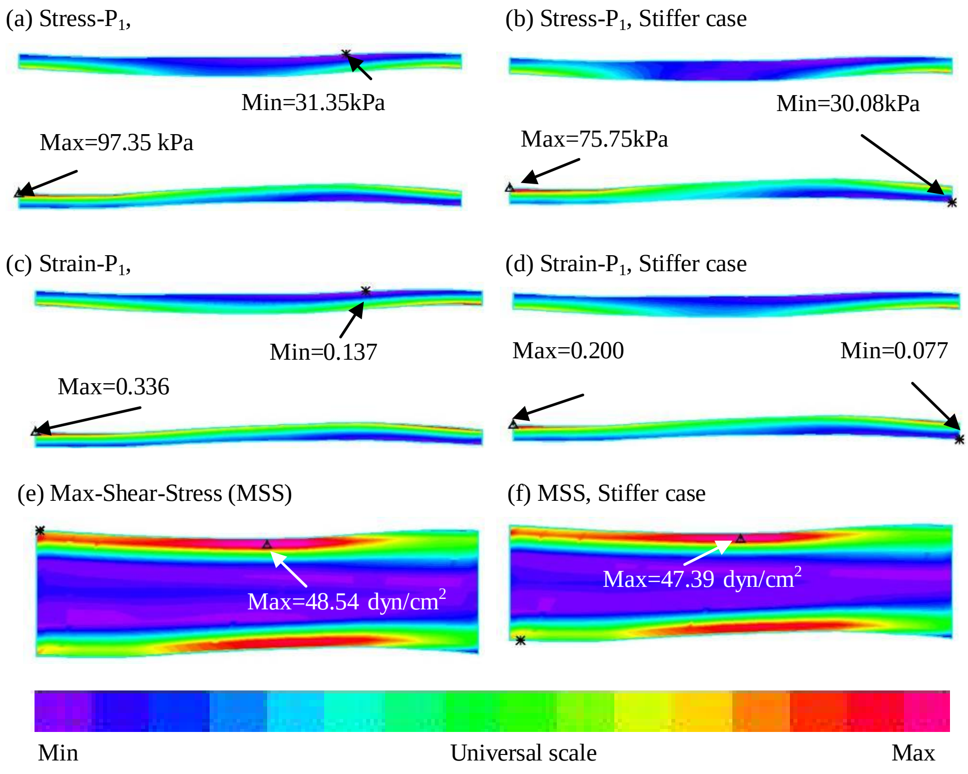

Figure 8.4. Plots of Stress-P$_1$, Strain-P$_1$, Max-Shear-Stress distribution from 2 cases (Case 0 & Case 10). (a)-(b) Stress-P$_1$; (c)-(d) Strain-P$_1$;(e)-(f) Max-Shear-Stress.

Fig. 8.5 shows Stress-P$_1$, Strain-P$_1$ and MSS tracked at a site on slice 12. TP$_1$ was chosen for tracking Stress-P$_1$/Strain-P$_1$ and TP$_2$ was chosen for tracking MSS. Stress-P$_1$ decreased by 12.5%, Strain-P$_1$ decreased by 48%, and MSS was almost unchanged as material stiffness increased 100%.

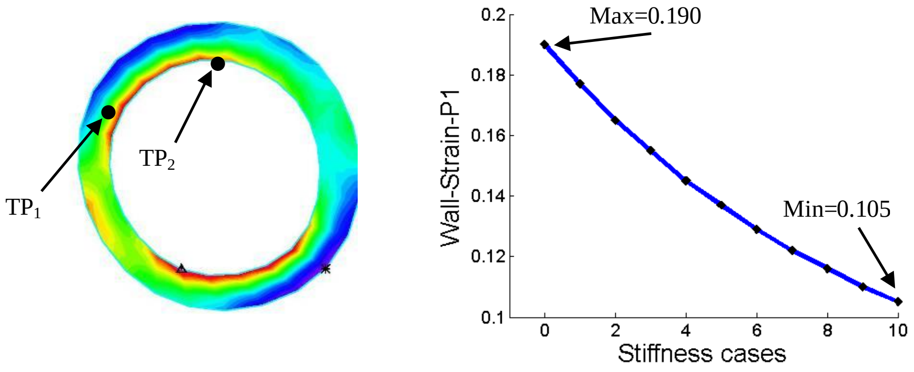

(a) Tracking Points

(b) Strain-P_1 from TP1

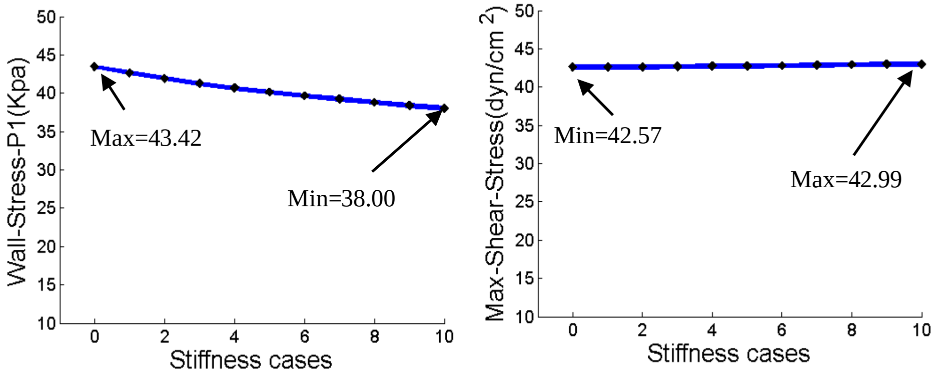

(c) Stress-P_1 from TP1

(d) MSS from TP2

Figure 8.5. Flow and stress/strain values at tracking points vary with material stiffness parameter changes. Horizontal label indicates 11 cases (from Case 0 to Case 10). (a) Stress-P_1 and position of tracking points on slice 12; (b) Strain-P_1 tracked at TP_1; (c) Stress-P_1 at TP_1; (d) MSS at TP_2.

This quantitative study shows that structure Stress/Strain variations are sensitive to the material stiffness. The findings suggest that obtaining accurate material properties is very important for the accuracy of computational simulations and predictions, especially for structure stress/stain analysis. Flow variables are less sensitive to material stiffness variations.

8.4 Discussion and Conclusion

Vessel material property is an important integrated part of FSI models. It's critical for the computational results and risk analysis for plaque vulnerability assessment. The method presented in this chapter is the first attempt combining MRI data obtained under pressurized conditions and 3D computational modeling to determine parameter values in material models so that the 3D vessel deformation has the best fit with MRI measurement. It may have the potential to be extended to *in vivo* applications. In addition, effects of material properties on flow and wall stress/strain behaviors were evaluated. The result indicates that accurate material properties measurement will improve the accuracy and reliability of computational assessments and predictions.

9. Quantify Artery Shrinkage and Effect of Shrink-Stretch Process

9.1 Introduction

In this chapter, a method using patient-specific *in vivo*/*ex vivo* MRI images to quantify human carotid artery shrinkage in axial and radial directions between *in vivo* (loaded) and *ex vivo* (unloaded) state is presented. To our knowledge, this is the first report demonstrating human carotid artery shrinkage using *in vivo* and *ex vivo* MRI images, although it has been recognized for many years that *in vivo* arteries subjected to significant axial stretch. The results in this chapter have been published in [32].

The shrink-stretch procedure described in section 5.4 was used to process the *in vivo* MRI contour to obtain the computing start shape for 3D MRI-based FSI model. Six multi-component 3D FSI models of carotid atherosclerotic plaques were developed to quantify the effects of axial/radial shrinkage on critical flow and plaque stress/strain conditions.

9.2 Data Acquisition and Artery Shrinkage

9.2.1 Multi-Contrast MRI Acquisition

3D *in vivo*/*ex vivo* MR images of human carotid atherosclerotic plaques from ten (10) patients (age: 51-82, average: 65; 9 male; 1 female) were acquired by Dr. Yuan's group (9 patients) at University of Washington (UW) using protocol approved by University of Washington Institutional Review Board, and by Dr. Woodard and Dr. Zheng's group (1 patient) at Washington University (WU) using protocol approved by Washington University Institutional Review Board, with informed consent obtained at both locations. High resolution, Multi-contrast in T1, T2, proton density (PD), time-of-fight (TOF), and contrast-enhanced (CE) T1 weighed MRI images of carotid arteries were obtained to characterize plaque tissue composition, luminal and vessel wall morphology. A segmentation package CASCADE (Computer-Aided System for Cardiovascular Disease Evaluation) developed by the Vascular Imaging Laboratory (VIL) at UW was used by Yuan's group to perform image analysis and segmentation [37]. Fig. 9.1 gives a screen shot of a CASCADE display showing multiple contrast weighting MR images with contours generated by CASCADE.

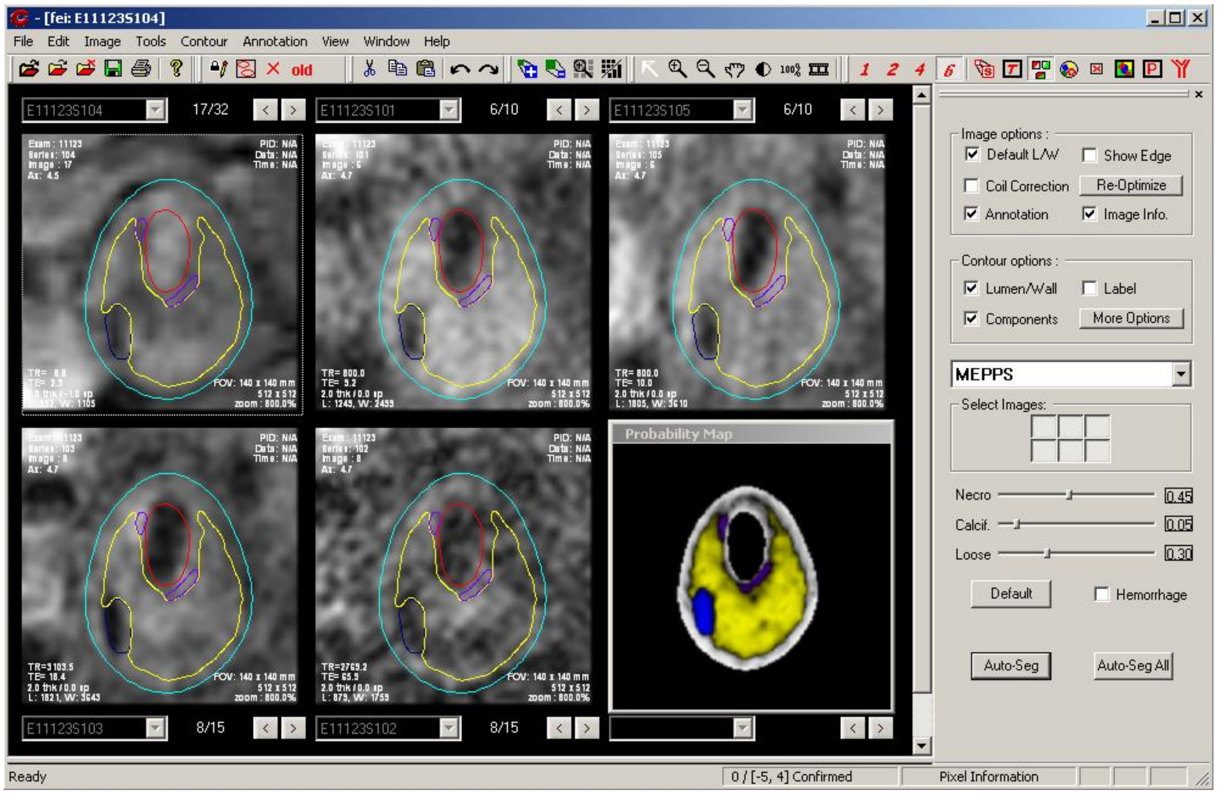

Image options :
☑ Default L/W ☐ Show Edge
☐ Coil Correction
☑ Annotation ☑ Image Info.

Contour options :
☑ Lumen/Wall ☐ Label
☑ Components

MEPPS

Necro 0.45
Calcif. 0.05
Loose 0.30
☐ Hemorrhage

Ready
0 / [-5, 4] Confirmed
Pixel Information

Figure 9.1. Contour plots of plaque components shown were generated by CASCADE and digitized for 3D geometry reconstruction. The CASCADE interface permits multiple-contrast weighting display, interactive delineation of plaque features, and concise reporting of quantitative lesion indexes among other functions.

CASCADE provides manual and automatic analysis tools for accurate lumen and wall boundary identification, and image registration. It is able to accurately identify specific plaque features, including the lumen, wall boundary, lipid rich necrotic core, calcifications and other components. The segmented results have been validated by histological studies. MRI data acquired at WU site was segmented by Woodard and Zheng's group using a self-developed software package, Atherosclerotic Plaque Imaging Analysis (APIA), written in Matlab (Math Works, MATLAB, Natick, MA), and the results also have been validated by histological analysis.

9.2.2 Artery Shrinkage in Axial/Cross-Section Direction

In vivo/*ex vivo* MRI Images of carotid atherosclerotic plaques were used to construct *in vivo*/*ex vivo* geometries. Both 3D geometries and 2D slices were carefully examined and compared to identify "corresponding locations" to quantify patient-specific artery shrinkage. The bifurcation point is a natural choice for registration. Other plaque morphological features such as lumen narrowing and shape change, plaque component size, shape and location were all considered. The *ex vivo* and *in vivo* images might be very different due to: a) different image resolution; b) plaque sample changes once it was taken out of human body (loss of blood, water, lipid leakage, *etc.*); c) deformation caused by manual handling. Among various morphological features, lumen size and shape are more reliable and easier to compare *ex vivo* images with *in vivo* images. Therefore using lumen size to register became our preferred choice. The luminal bifurcation and narrowest location were selected as marking points for registration. Fig. 9.2 gives the registration results using both 2D slices and the matching 3D view.

(a) *In vivo* MRI and Segmented Contours

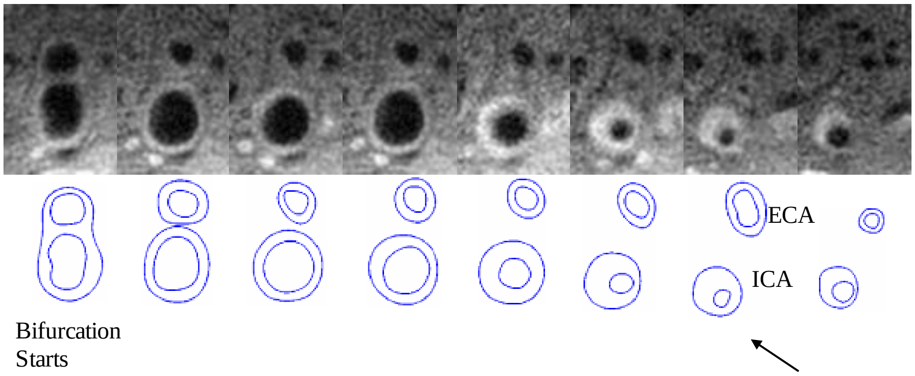

(b) *Ex vivo* MRI and Segmented Contours

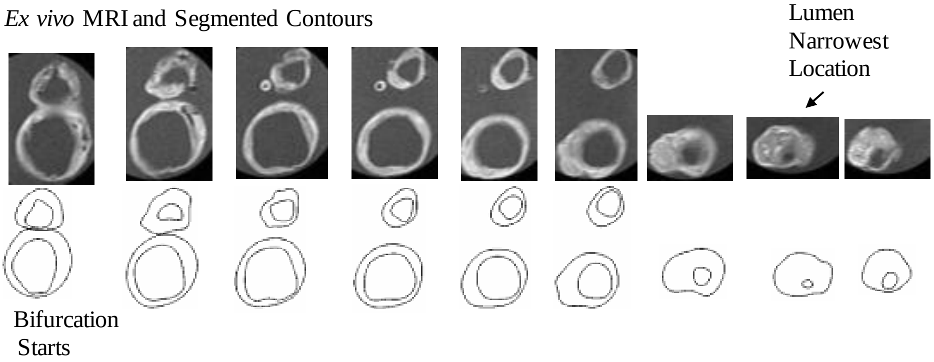

(c) *In vivo/Ex vivo* 3D Comparison

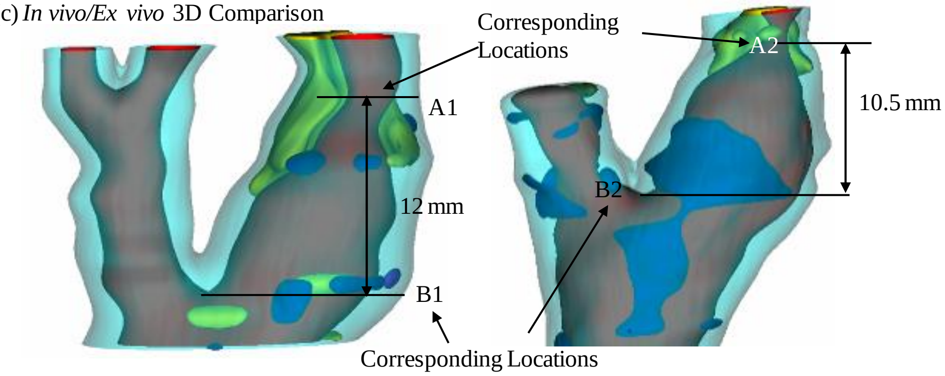

Figure 9.2. In vivo and ex vivo MR images and 3D geometries of a human carotid plaque were compared to quantify axial and inner circumferential shrinkages. (a) In vivo MRI images and segmented contour plots(Example #1); (b) Ex vivo MRI images and segmented contour plots; (c) 3D geometries and identified corresponding locations. Blue: Calcification; Yellow: Lipid-rich necrotic core*; Red: Lumen; Light blue: Artery wall.*

In Fig. 9.2(c), locations A1, A2 mark the corresponding lumen narrowest location and B1, B2 indicate the corresponding beginning position of luminal bifurcation at *in vivo* and *ex vivo* state, respectively. There are 7 slices of MRI image at *in vivo* state (Fig. 9.2(a)) and 8 slices of MRI image at *ex vivo* state (Fig. 9.2(b)) between these two locations, respectively. The slice thickness of *in vivo* MRI data set is 2 mm, so the length of the two marking points at *in vivo* state is 12 mm. The slice thickness of *ex vivo* MRI images is 1.5 mm. Therefore the distance of the two marking points is 10.5 mm at *ex vivo* state. Assuming the shrinkage of the artery in the axial direction was uniform and defining the axial shrinkage as λ_z,

$$\lambda_z = (L_{in} - L_{ex})/L_{in} \times 100\% \qquad (9.1)$$

where L_{in} and L_{ex} are the distance between the two marking points at *in vivo* and *ex vivo* state, respectively. For the case shown in Fig. 9.2, the axial shrinkage is 12.5%. Fig. 9.3 gives 3 more examples showing site registrations using lumen and plaque component features.

(a) Example #2: Matching result by components (lipid) , λ_Z=25%

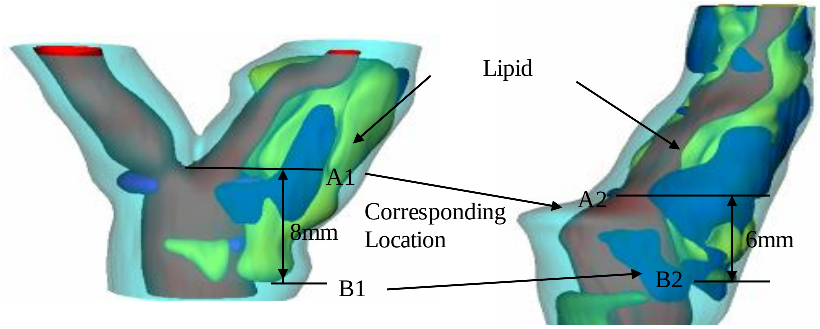

(b) Example #3: Matching result by lumen size, λ_Z=25%

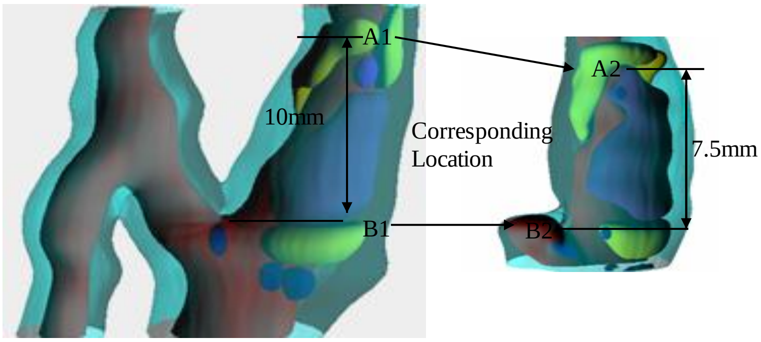

(c) Example #4: Matching result by lumen size, λ_Z=25%

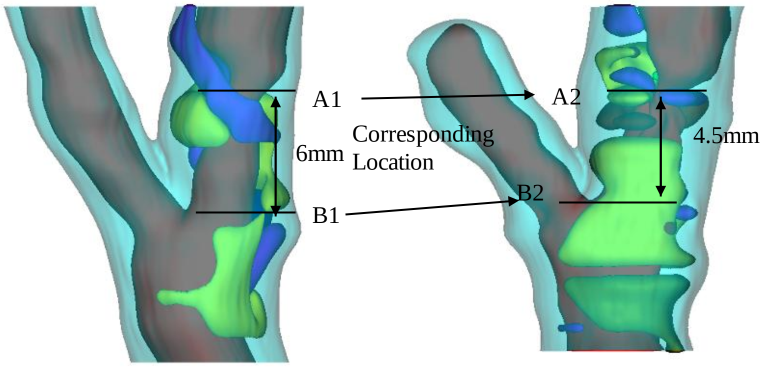

Figure 9.3. Three more examples showing plaque registration results, 3D view.

To quantify the shrinkage in cross-section, the circumference of plaque lumen contour was chosen for the following reasons: a) lumen contour can be relatively more precisely captured by MRI; b) most plaque cross sections are of very irregular shape and not circular. It is not possible to define "radius" for those cross sections. On the other hand, circumference can be calculated easily and used to measure circumferential shrinkage; c) when plaque is taken out of human body during endarterectomy surgery, the media and adventitia layers of the artery are kept in patient's body. Therefore, while *in vivo* MR images include the artery with all its layers, *ex vivo* samples and MR images do not enclose the media and adventitia layers of the vessel. So the outer boundary is not suitable for use in determining circumferential shrinkage. The circumferential shrinkage is defined as λ_C,

$$\lambda_C = (C_{in} - C_{ex}) / C_{in} \times 100\%, \tag{9.2}$$

where C_{in} and C_{ex} are the lumen circumference at *in vivo* and *ex vivo* state, respectively. When the *in vivo* and *ex vivo* MRI images were not matched slice by slice, linear interpolation was used to calculate the inner circumference of corresponding slice at *ex vivo* state. The average shrinkage values from all slices of a plaque sample were used as the circumferential shrinkage for each plaque.

9.3 Results

In this section, the results of human carotid artery axial and inner circumferential shrinkages were presented. Using the modeling and solution methods presented in Chapter 5 & 6, six 3D FSI multi-component models were obtained to investigate the effects of different axial stretch ratio and circumferential shrinkage/expansion on critical flow and plaque stress/strain conditions: Case 1 (base model) & 2: 0% axial stretch, with/without circumferential shrinkage; Cases 3 & 4: 10% axial stretch, with/without circumferential shrinkage; Cases 5 & 6: 33% axial stretch, with/without circumferential shrinkage.

9.3.1 Artery Axial and Circumferential Shrinkage

Table 9.1 gives axial and circumferential shrinkage results from 10 patients who participated in this study. From this 10 patient data set, it was found that the average value of axial shrinkage was 24.6% and inner circumferential shrinkage was 7.9%.

Patient	Circumferential Shrinkage (%)	Axial Shrinkage (%)
Patient 1	3.3	25.0
Patient 2	9.2	25.0
Patient 3	12.3	25.0
Patient 4	11.9	25.0
Patient 5	5.7	25.0
Patient 6	-5.3	12.5
Patient 7	10.3	25.0
Patient 8	5.7	25.0
Patient 9	16.7	25.0
Patient 10	9.1	33.3
Average	7.9	24.6

Table 9.1. The results of axial and circumferential shrinkage for carotid artery determined from comparisons of in vivo and ex vivo MR images and re-constructed 3D geometries. Data was obtained from 10 participating patients.

9.3.2 Overview of Plaque Behaviors

Fig. 9.4 shows the plaque sample (MRI & Segmented data were shown in Fig. 4.1) with one MRI slice, the corresponding histological data indicating the site of rupture, and 3D re-constructed geometry of the plaque.

(a) MRI and Histology for Slice 7 (S7) Showing Site of Rupture

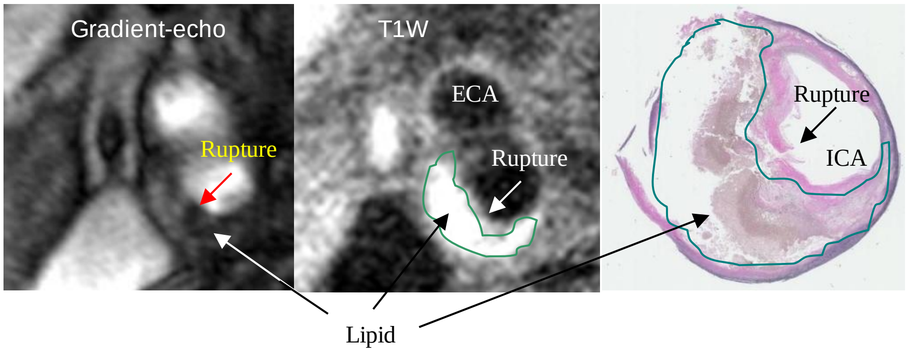

(b) Re-Constructed Plaque #1 3D Geometry

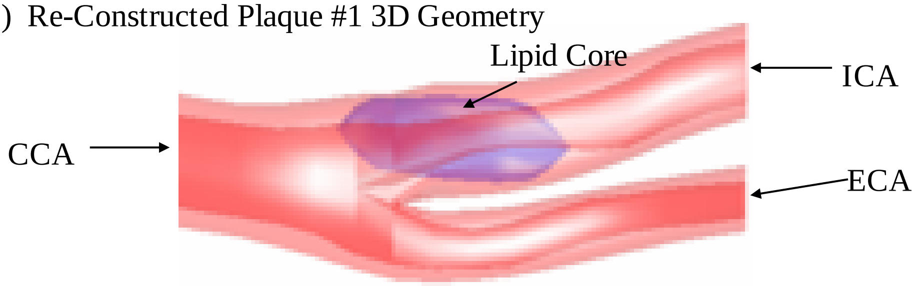

Figure 9.4. A human carotid plaque sample with histological data showing rupture. a) An MRI slice with matching histological slide showing site of rupture; b) 3D re-constructed plaque geometry.

An overview of solution features from our 3D FSI models (Case 3) were presented in Fig. 9.5. Stress-P_1 on stacked cross-section slices, Stress-P_1 and Strain-P_1 distributions on a bifurcation cut (B-cut) surface, and Strain-P_1, flow velocity, pressure, and FMSS on the L-cut are shown. Fig. 9.5(a) & (c) shows that maximum Stress-P_1 and Strain-P_1 value located at the site of rupture. Fig. 9.5(d)-(g) give the band plots of both structure and flow features on L-cut surface which shows lipid pool and cap thickness much clearer than the bifurcation cut. Fig. 9.5(d) presents distribution of Strain-P_1 showing maximum value located at the lipid cap position. Flow velocity is higher at the stenosis narrowing of internal carotid artery (ICA). A maximum value of

Maximum-Shear Stress (MSS) was also found at the plaque throat (narrowing). 3D FSI results contain rich information which can serve as the basis for many further investigations.

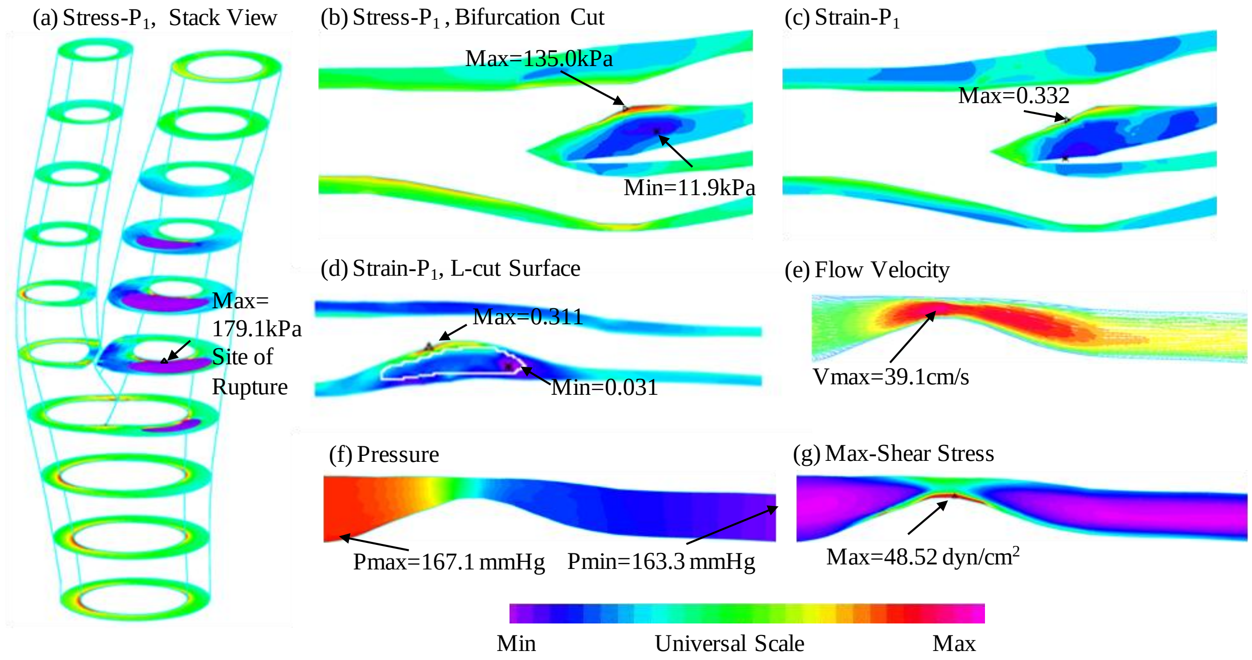

Figure 9.5. Overview of 3D FSI solution (Case 3, 10% axial stretch, 7.8% inner circumferential shrinkage) behaviors using plaque sample shown in Fig. 4.1, Pin=174 mmHg. a)Plot of Stress-P_1 distribution on stack view; b) Plot of Stress-P_1 distribution on B-cut surface; c) Plot of Strain-P_1 distribution on B-cut surface; d) Strain-P_1 on L-cut surface; e) Flow velocity reaching its maximum in the stenotic region; f) Pressure band plot on L-cut surface; g) Flow maximum shear stress band plot on L-cut surface showing a maximum at the stenosis throat.

9.3.3. Effects of Axial Stretch

Fig. 9.6 presents band plots of Stress-P_1 and fluid maximum shear stress (MSS) for the baseline case and Case 5 (0%, and 33% axial stretch, both with circumferential shrinkage) corresponding to 100 mmHg inlet pressure conditions. The L-cut surface is chosen to present the results for the comparative case studies because it has simpler geometry and shows the lipid core and plaque cap better. When axial stretch increased from 0% to 33%, maximum Stress-P_1 value increased from 62.6 to 281.6 kPa (349.8% increase). Stress distribution patterns and locations of maxima were different, greater axial stretch moved the location of maximum stress values to the healthy part of the vessel where the vessel wall is thin. On the other hand, when axial stretch increased from 0% to 33%, the maximum value of MSS increased from 37.3 to 39.9 dyn/cm^2 (6.97% increase). The changes in flow characteristic were much less noticeable. Therefore, to demonstrate the effects of shrink-stretch process, we mainly addressed on stress/strain behaviors in the structure part.

(a) Based Case, 0% Stretch, Stress-P_1 (b) Case 5, 33% Stretch, Stress-P_1

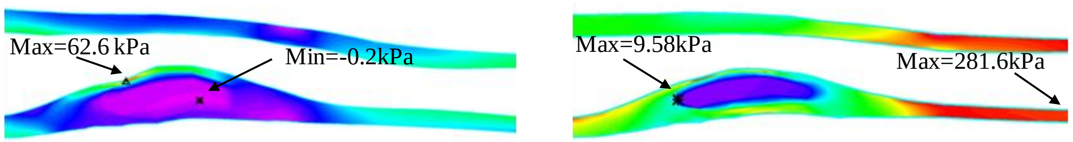

(c) Based Case, 0% Stretch, MSS (d) Case 5, 33% Stretch, MSS

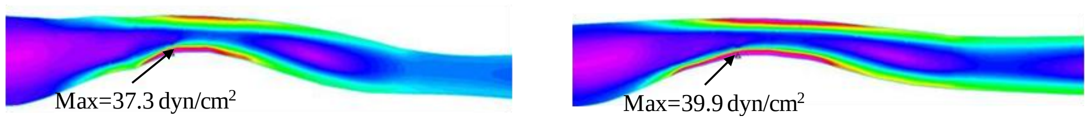

Figure. 9.6 Plots of Stress-P_1, and Fluid MSS distributions showing the effects of axial stretch by comparing the baseline case and Case 5.

Cases 1, 3, and 5 (with 0%, 10%, and 33% axial stretch, all with circumferential shrinkage) were compared to investigate the stress/strain variation with axial stretch. Fig. 9.7 & 9.8 give band plots of Stress-P_1/Strain-P_1 distributions for all six cases corresponding to 100 mmHg inlet pressure conditions. Maximum Stress-P_1 and Strain-P_1 values were summarized in Table 9.2. Using stress and strain values of Model 1 as the reference, maximum Stress-P_1 values increased from 62.6 to 78.7 kPa (Case 3, 25.7% increase) and 281.6 kPa (Case 5, 349.8% increase), and maximum Strain-P_1 values increased from 0.147 to 0.175 (Case 3, 19% increase) and 0.513 (Case 5, 249% increase), when axial stretch increased from 0% to 10% and 33%, respectively. Stress/Strain distribution patterns and locations of maxima were different for the 3 cases. Greater axial stretch moved the location of maximum stresses to healthy part of the vessel where the vessel wall is thin.

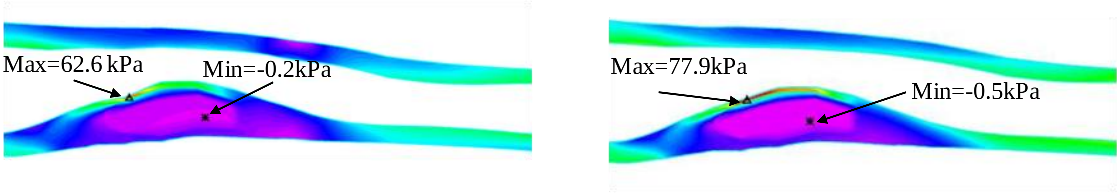

(a) Case 1, 0% Stretch, with Cir_Shrinkage

(b) Case 2, 0% Stretch, no Cir_Shrinkage

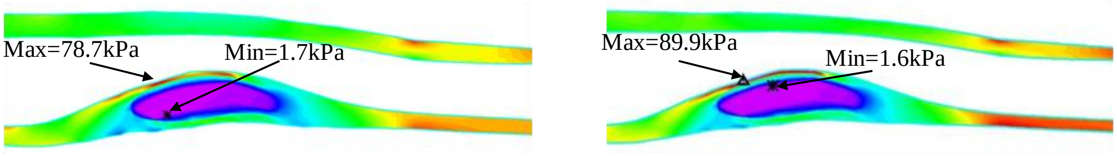

(c) Case 3, 10% Stretch, with Cir_Shrinkage

(d) Case 4, 10% Stretch, no Cir_Shrinkage

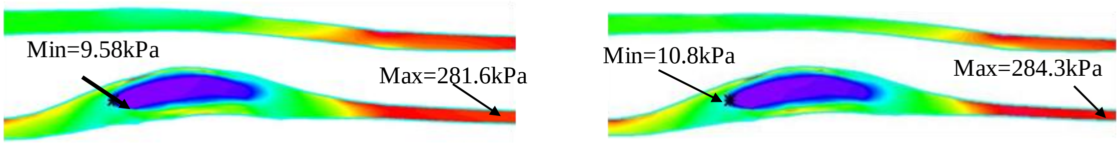

(e) Case 5, 33% Stretch, with Cir_Shrinkage

(f) Case 6, 33% Stretch, no Cir_Shrinkage

Figure 9.7. Plots of Stress-P_1 distribution on L-cut surface from 6 case studies showing effects of axial stretch and circumferential shrinkage.

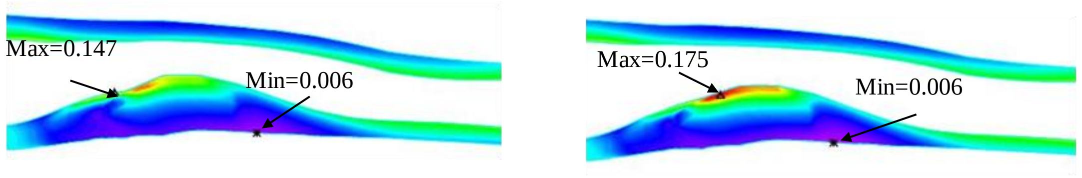
(a) Case 1, 0% Stretch, with Cir_Shrinkage

(b) Case 2, 0% Stretch, no Cir_Shrinkage

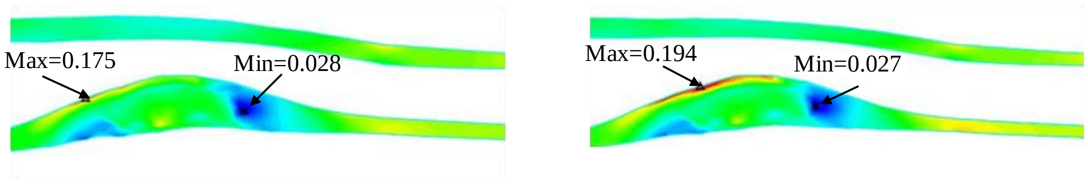
(c) Case 3, 10% Stretch, with Cir_Shrinkage

(d) Case 4, 10% Stretch, no Cir_Shrinkage

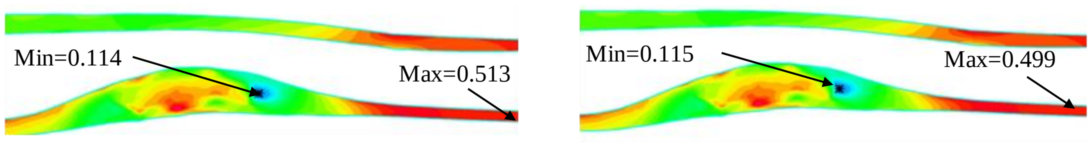
(e) Case 5, 33% Stretch, with Cir_Shrinkage

(f) Case 6, 33% Stretch, no Cir_Shrinkage

Figure 9.8. Plots of Strain-P_1 distribution on L-cut surface from 6 case studies showing effects of axial stretch and circumferential shrinkage.

Case	Defining Conditions		Stress-P_1 (kPa)	% of Base	Strain-P_1	% of Base
	Axial Stretch	Circumferential Shrinkage				
Case1	0%	YES	62.6	100	0.147	100
Case2	0%	NO	77.9	124.4	0.175	119.0
Case3	10%	YES	78.7	125.7	0.175	119.0
Case4	10%	NO	89.9	143.6	0.194	132.0
Case5	33%	YES	281.6	449.8	0.513	349.0
Case6	33%	NO	284.3	454.2	0.499	339.5

Table 9.2. Maximum values of Stress-P_1 and Strain-P_1 increased 349.8% and 249.0% respectively with 33% axial stretch: Comparison of maximum Stress-P_1 and Strain-P_1 values from 6 cases showing axial stretch has considerable effects on stress/strain predictions.

The plaque cap location was also chosen to be examined because that the rupture more likely occurs at such a location. Table 9.3 summarizes Stress-P_1 and Strain-P_1 values tracked at the plaque cap location for all 6 cases. Significant variations of Stress-P_1/Strain-P_1 values at the tracking point were found. Still using the results of Case 1 as the reference, Stress-P_1 values at plaque cap increased from 39.6 to 61.5 kPa (Case 4, 55.3% increase) and 167.9 kPa (Case 6, 324.0% increase), and maximum Strain-P_1 values increased from 0.105 to 0.116 (Case 4, 10.5% increase) and 0.271 (Case 6, 158.1% increase), when axial stretch increased from 0% to 10% and 33%, respectively. These results demonstrate that the axial stretch also has considerable effects on plaque cap stress/strain conditions which are closely related to plaque rupture and vulnerability assessment [67].

Case	Defining Conditions		Stress-P_1 (kPa)	% of Base	Strain-P_1	% of Base
	Axial Stretch	Circumferential shrinkage				
Case1	0%	YES	39.6	100	0.105	100
Case2	0%	NO	59.1	149.2	0.148	141.0
Case3	10%	YES	61.5	155.3	0.116	110.5
Case4	10%	NO	76.1	192.2	0.146	139.0
Case5	33%	YES	167.9	424.0	0.271	258.1
Case6	33%	NO	166.3	419.9	0.261	248.6

Table 9.3. Comparison of Stress-P_1 and Strain-P_1 values tracked at plaque cap. Values of Stress-P_1 and Strain-P_1 at the plaque cap increased about 324% and 158% respectively with 33% axial stretch.

9.3.4 Effects of Circumferential Stretch

Fig. 9.7 & 9.8 and Tables 9.2 & 9.3 give Stress-P_1/Strain-P_1 plots as well as maximum values for the 6 cases to investigate the variation of stress/strain behavior due to circumferential stretch.

Table 9.4 calculated the percentage differences using Cases 1, 3, & 5 (all with circumference shrinkage) as base numbers. The cases (cases 2 & 4) without circumference shrinkage gave higher stress/strain values (plaque cap Stress-P_1 was 49.2% higher for 0% case, and 23.7% higher for the 10% case). However, ignoring circumference shrinkage only induces a very small deviation (plaque cap Stress-P_1 was 0.95% lower, and Strain- P_1 was 3.7% lower) in the 33% axial stretch group (Cases 5 & 6). These results indicate that when the axial stretch is more significant, the effects of circumferential shrinkage on stress/strain are less noticeable. This can be explained by the fact that larger axial stretch makes dominant contributions to Stress-P_1 and Strain-P_1 due to larger axial deformation comparing with much smaller circumferential deformation. However, when axial stretch is smaller (<10%), effects from the circumferential shrinkage become noticeable and should be taken into account.

Axial Stretch	Max Stress-P_1 Increase (%)	Cap Stress-P_1 Increase (%)	Max Strain-P_1 Increase (%)	Cap Strain-P_1 Increase (%)
0%	24.4	49.2	19.0	41
10%	14.2	23.7	10.9	25.9
33%	0.96	-0.95	-2.7	-3.7

Table 9.4. Comparison and percentage increases (no circumferential shrinkage vs. with circumferential shrinkage, i.e., Cases 2,4,6 vs Cases 1,3,5) of maximum and plaque cap Stress-P_1 and Strain-P_1 values on L-cut surfaces showing the circumferential shrinkage affects.

9.4 Discussion and Conclusion

The method and results presented here are the first attempt quantifying human carotid artery axial and inner circumferential shrinkages by comparing *ex vivo* and *in vivo* MRI images. The average value of axial shrinkage from the 10 patient data was 24.6% and average circumferential shrinkage was smaller (7.9%). This is significant and should be taken into consideration in computational modeling.

The effects of axial stretch and circumferential shrinkage/expansion were quantified by six FSI models. The obtained results indicate that the effects of axial stretch are not only in stress/strain value but also in their distribution patterns, especially when axial stretch is large (33% stretch case). Maximum values of maximum principal stress and strain increased 349.8% and 249% respectively with 33% axial stretch ratio. Influence of inner circumferential shrinkage (7.9%) was not very noticeable under 33% axial stretch ratio, but became more noticeable when axial stretch ratio was smaller (<10%). Our results indicated that accurate knowledge of artery shrinkages and the shrink-stretch process will considerably improve the accuracy of plaque vulnerability assessment based on computational results obtained from those *in vivo* MRI-based FSI models.

While our *in vivo* MRI-based plaque model with fluid-structure interactions represents clear advances in the modeling process, some limitations and model simplifications should be acknowledged: a) Opening angle is not included since it is un-measurable with current technique; b) Tissue tethering is the mechanical force that keeps the artery in its *in vivo* shape. It was not included in our model so our model geometries tend to become rounder when pressurized. This may lead to increased stress/strain concentration level at large curvature sites. Including tethering in FSI models represents a big challenge to all modeling researchers. c) Non-Newtonian effect was not included because it has been recognized that differences between Newtonian and Non-Newtonian flow models for large arteries are small and can be ignored [81]. d) Different tissue and plaque components may have different shrinkage and may affect the artery shrinkage. For example, calcification may shrink much less and lipid core may shrink more. This should be taken into consideration by shrinking individual component separately, if data is available.

Another non-modeling limitation of this study was the resolution of *in vivo/ex vivo* MRI images. The slice thickness was 2 mm for *in vivo* MRI images and 1.5 mm for *ex vivo* MRI images, respectively. The resolutions of *in vivo* and *ex vivo* MRI images were not the same. *Ex vivo* images had better resolution and could “see” plaque components better, which made it hard to compare *in vivo* and *ex vivo* geometries. These issues limited the accuracy of our shrinkage results. This could be improved when MRI images with better resolution become available.

10. Critical Flow and Stress/Strain Conditions and Plaque Rupture

10.1 Introduction

In clinical diagnosis, the lipid-rich core and the thickness of fibrous cap overlying the core are two major determinants of plaque's vulnerability [25]. With this in mind, lipid-rich core and fibrous cap thickness were chosen as parameter for investigation. In this chapter, two *in vivo* MRI-based 3D computational models were constructed to investigate the effects from lipid-rich necrotic core on structure/flow behaviors. Ten (10) adjusted 3D computational models with different plaque thickness were developed to evaluate the effects of plaque thickness on plaque wall stress and strain, and flow maximum shear stress (MSS) distribution.

3D *in vivo* MRI data sets of human carotid atherosclerotic plaques from two patients were used to construct 3D FSI computational models. The *in vivo* MRI data of patient 1 (P1) are shown in Fig. 4.1 and those from patient 2 (P2) were shown in Fig. 10.1 (provided by Dr. Yuan's group at University of Washington, Seattle). The following imaging parameters were used: a) in vivo MRI: field of view (FOV): 160×160mm^2, matrix size: 512×512, slice thickness 2mm. Using the method described in Chapter 4-6, FSI computational model were constructed and the solutions were obtained.

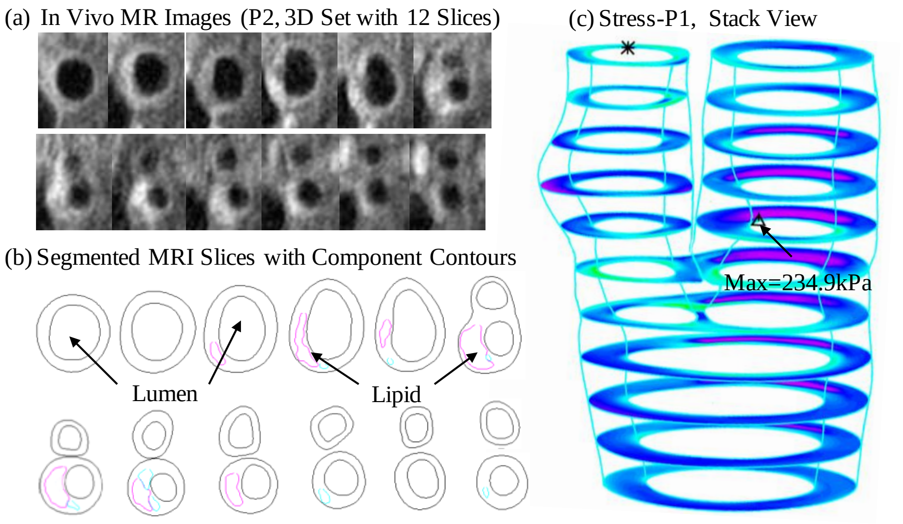

Figure 10.1. In vivo 3D MRI images of a human carotid plaque (P2). (a) 12 T1-weighted MRI slices (S1-S12), slice spacing: 2mm. Each image shown here was cut from the whole neck image; (b) Segmented contour plots showing plaque components; (c) Plot of Stress-P_1 distribution on 3D stack view obtained from FSI model.

10.2 Effects of Lipid Component

The results of wall Stress-P_1 and Strain-P_1 were extracted from these two 3D FSI solutions from each node on the lumen surface. The node was assigned as specified component node if the connected fibrous cap overlies component, otherwise the node would be assigned as wall node. For example, if the connected cap covers lipid, the node will be assigned as lipid node. Student *t*-test was selected to perform statistical analysis. Significant difference will be found if p value is smaller than 0.0001.

10.2.1 Comparison between Lipid and Non-Lipid Nodes.

For P1, the mean value of wall Stress-P_1 from all lipid nodes was 112.3 kPa, which was 53.2% higher than the mean value from all non-lipid nodes ($p<0.0001$). For P2, the mean Stress-P_1

value of lipid nodes was 80.1 kPa, which was 26.5% higher than the one from non-lipid nodes ($p<0.0001$). The results from both patients indicated that the value of Stress-P_1 of lipid nodes is significantly higher than the one from non-lipid nodes. The details could be found from Table 10.1. The similar results for Strain-P_1 were found (Table 10.2).

Case	Rupture	Lipid		None Lipid		p-value
		mean	Number of nodes	mean	Number of nodes	
P1	Yes	112.3	83	73.3	110	<0.0001
P2	No	80.1	66	63.3	437	<0.0001
Two patients		98.1	149	65.3	547	<0.0001

Table 10.1. Summary of mean plaque wall Stress-P_1 value of lipid, and non-lipid nodes for these two patients' FSI models. p-values are for lipid and non-lipid nodes comparison. Unit: kPa.

Case	Rupture	Lipid		None Lipid		p-value
		mean	Number of nodes	mean	Number of nodes	
P1	Yes	0.235	83	0.169	110	<0.0001
P2	No	0.185	66	0.146	437	<0.0001
Two patients		0.213	149	0.151	547	<0.0001

Table 10.2. Summary of mean plaque wall Strain-P_1 value of lipid, and non-lipid nodes from FSI models of P1 & P2. p-values are for lipid and non-lipid nodes comparison.

10.2.2 Comparison between the Ruptured (P2) and Non-Ruptured (P1) cases

Plaque rupture of P1 was observed by MR Image which is shown in Fig. 9.4 (a) and confirmed by the histological examination (Fig. 9.4 (a)). Some 2D simulations and histological studies suggested that the region of lesion bears high mechanical stress concentration [11, 43]. However, this hypothesis has never been validated by 3D *in vivo* study. For this concern, the comparisons of Stress-P_1 and Strain-P_1 between P1 and P2 were performed as follows.

The mean value of wall Stress-P_1 and Strain-P_1 from lipid nodes of rupture case were found to be significant higher than non-rupture case (112.3 kPa, 0.235 & 80.1 kPa, 0.185), which were 40.2% and 26.8% higher, respectively ($p<0.001$). For non-lipid nodes, the stress and strain values are 15.9%, 16.2% higher than non-rupture case. These indicate that the Stress-P_1 and Strain-P_1 values from lipid nodes are more sensitive than non-lipid nodes. That might imply that mechanical parameter of lipid nodes is a better indicator for assessment of the plaque vulnerability.

10.3 Effects of Plaque Cap Thickness

It should be noted that fibrous cap overlies different component, including lipid-rich necrotic core, calcification, *etc*. In this case, the focus was on the thin cap covers lipid-rich necrotic core and it was named “lipid-cap”. To investigate the effects of fibrous lipid-cap thickness on wall Stress-P_1 and Strain-P_1 and flow MSS distribution, a total of ten (10) adjusted FSI models based on P2 (non-rupture plaque in section 10.2) were constructed. Fixing the positions of lumen, wall, and non-lipid components, the lipid-cap thickness was varied from 0.05mm to 0.5 mm with 10 even steps by translating lipid component.

The location where the thinnest region overlies a lipid component in Slice 8 was considered as a critical site. Wall stress and strain values at critical site were used to investigate the effects of cap thickness.

Using Case 1 (Cap thickness=0.05mm) as the base model, when thickness increase from 0.05 mm to 0.50 mm, Stress-P_1 value decreased from 231.6 kPa to 66.6 kPa, which was 71.2% less; Strain-P_1 value decreased from 0.340 to 0.131, which was 61.4% lower; However, the flow MSS increased from 31.0 dyn/cm^2 to 36.6 dyn/cm^2, which was 18.1% higher (Table 10.3).

	Thickness (mm)	Stress-P_1 (kPa)	Strain-P_1	MSS dyn/cm^2
Case1	0.05	231.6	0.340	31.0
Case2	0.10	190.1	0.298	32.2
Case3	0.15	169.9	0.297	31.5
Case4	0.20	140.6	0.250	32.8
Case5	0.25	127.3	0.235	33.2
Case 6	0.30	113.4	0.219	33.7
Case7	0.35	102.8	0.205	34.1
Case8	0.40	94.4	0.194	34.5
Case 9	0.45	71.0	0.137	35.8
Case10	0.50	66.6	0.131	36.6

Table 10.3 Summary maximum values of wall Stress-P_1, Strain-P_1, and flow MSS in one cardiac cycle at critical site tracking point for all 10 cases showing effects of lipid-cap thickness.

Fig. 10.2 presents wall stress and strain value at critical cite in one cardiac cycle from Case 1, 4, 7, and 10 (with 0.05 mm, 0.2 mm, 0.35 mm, and 0.5 mm lipid-cap thickness). When lipid-cap thickness increased from 0.05 mm to 0.2 mm (Case1 & Case 4), the highest Stress-P_1 value in one cycle decreased 91.0 kPa; however, when lipid-cap thickness is 0.2 mm (Case 4) and 0.35 mm (Case 7), increased with same interval (0.15mm), the highest Stress-P1 value decreased only 37.8 kPa and 36.2 kPa, respectively. These results indicate that when lipid-cap is thin (lipid-cap thickness is less than 0.2 mm), the stress is much more sensitive to the change of lipid-cap thickness. The same phenomenon was observed from Strain-P_1 study (Fig. 10.2 (b)).

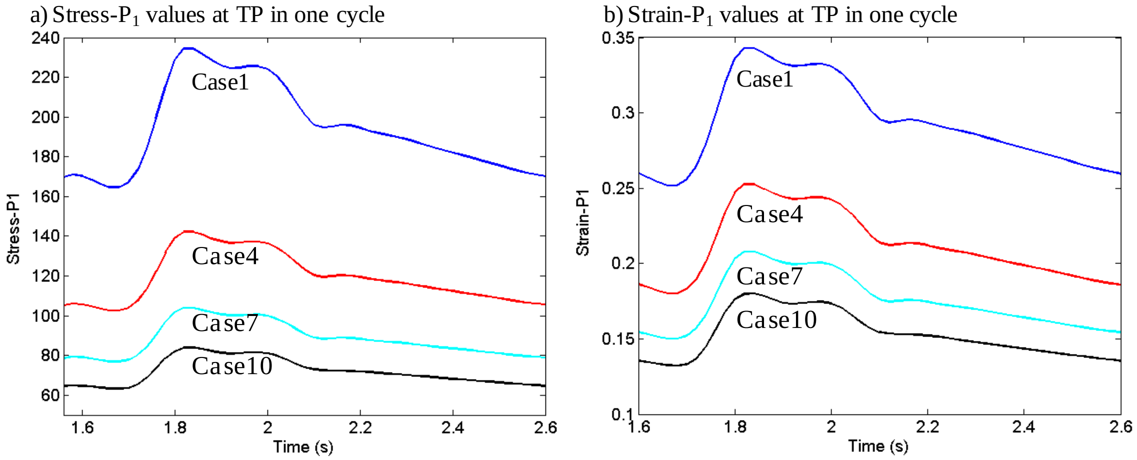

Figure 10.2. Comparison of wall Stress-P_1 & Strain-P_1 value at critical site from the selected cases in one cardiac cycle.

Such phenomenon of stress can be well captured the following exponential function as shown in Fig. 10.3(a) (R^2=0.9916),

$$\text{Stress-P}_1 = 237.4e^{-3.5\times\text{CapThickness}} + 28 \tag{10.1}$$

The relationship between Strain-P_1 and cap thickness can be approximated by a linear function (R^2= 0.9710),

$$\text{Strain-P}_1 = -0.4453\times\text{CapThickness} + 0.3531 \tag{10.2}$$

the fitting results are presented in 10.3 (b). It is worth noting that wall stress increased exponentially with decreasing thickness. Therefore, compared with strain, stress is a better indicator for the plaque risk assessment. The maximal shear stress (MSS) due to blood flow has a positive relation with cap thickness (Fig. 10.3(c); R^2=0.9495),

$$\text{MSS} = 11.52\times\text{CapThickness} + 30.37 \tag{10.3}$$

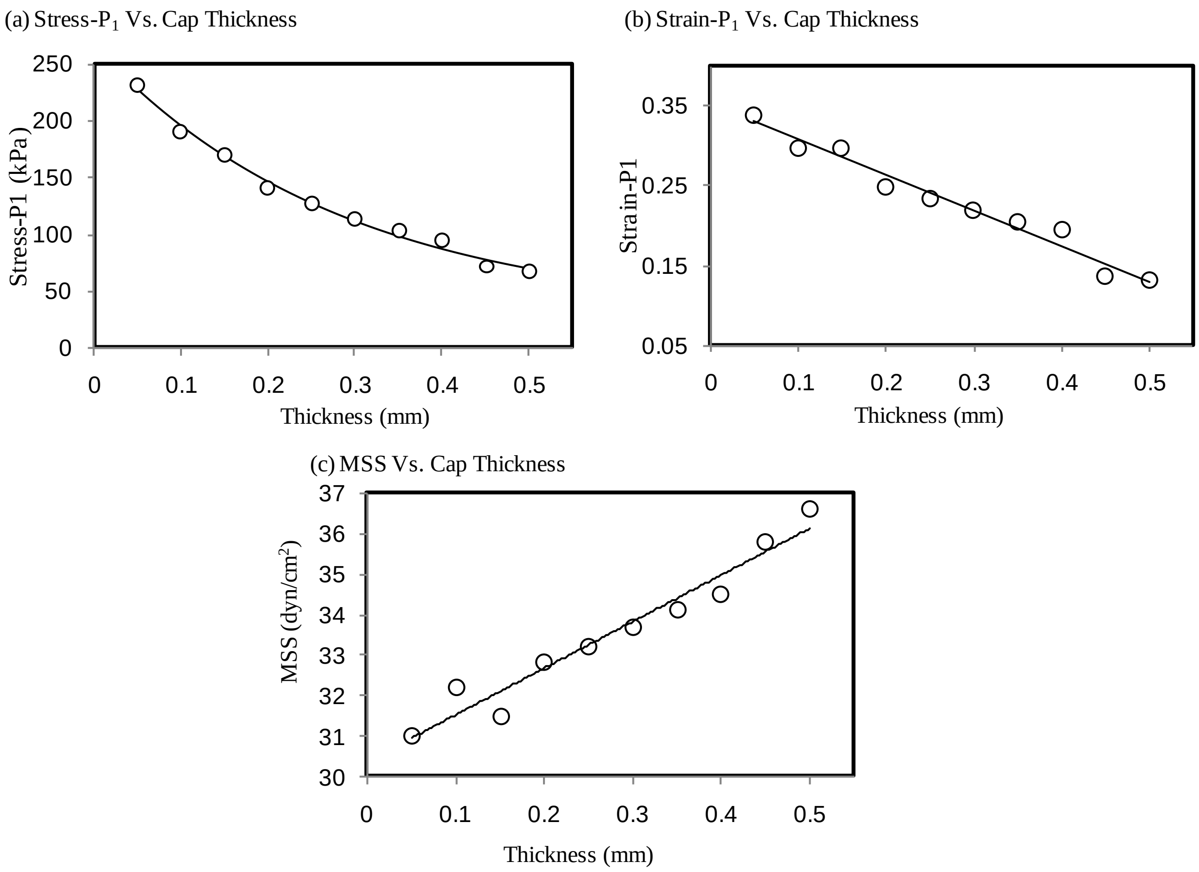

Figure 10.3. Plots of Stress-P_1 vs. cap thickness, Strain-P_1 vs. cap thickness, and MSS vs. cap thickness with the corresponding fitting curves obtained using the least squares method.

10.4 Discussion and Conclusion

Two MRI-based FSI computational models were re-constructed to study the effects of lipid component. The results show that the mean values of Stress-P_1 and Strain-P_1 from all lipid nodes were considerable higher than the ones obtained from other non-lipid nodes, especially for the rupture case. Therefore, wall stress/strain values of lipid nodes may be a good indicator for evaluating the plaque risk. A total of ten (10) adjusted FSI models were constructed to investigate the effects of fibrous lipid-cap thickness on structure/flow behaviors. To eliminate the contribution from other factors, morphologies of all components, except for lipid-cap thickness, were fixed. The obtained results indicate that wall stress and strain has negative correlations with lipid-cap thickness, while flow MSS has a positive correlation. The wall stress increased exponentially with decreasing thickness. These findings can explain why the plaque with thin cap is thought to be vulnerable. What's more, the obtained relationship between stress and strain respect with cap thickness may have the potential to predict the plaque growth function over certain period of time. To further validate the proposed relationship between wall stress and strain with cap thickness, large scale patients' study is necessary.

In this study, only the affect of lipid and the lipid-cap thickness was investigated due to the data limitation. Other component type (such as calcification and loose matrix) may have very different behaviors. Moreover, the contribution from the size of lipid core is not discussed. Another non-modeling limitation of this study was the resolution of *in vivo* MRI. Limited by the current technology, the current resolution is only 0.3 mm. For a more accurate assessment, one of the essential aspects is to improve the MRI resolution.

Part IV.

Discussion and Conclusion

11. Discussion

11.1 Contributions, Significance of Work Performed, and Related Fundamental Issues

Most reported image-based computational models for atherosclerotic plaques are based on histological or *ex vivo* MRI Images [27, 67, 70]. A few papers based on *in vivo* MRI are starting to appear in very recent years [43,81] . Though higher resolution can be obtained by using the histological image or *ex vivo* MRI, the plaque morphological information may be changed and damaged when the plaque is removed and distorted by further fixing procedures. Furthermore, the obtained plaque geometry does not include the complete shape of plaque, because endarterectomy specimen does not involve the whole artery. Therefore, compared with most of reported studies using the geometry derived from healthy patient [36, 82, 89] data, histology [27], or *ex vivo* MRI [70], the study in this dissertation based on *in vivo* MRI has more clinical relevance.

Usually, there is more than one atherosclerotic component enclosed in the plaque. It is essential to distinguish the contour of each component, since different component has different mechanical properties. Therefore identify the plaque morphology is one of the most fundamental issues and will dominate the accuracy of a MRI-based computational model. The developed segmentation method in this dissertation is capable of precisely classifying different tissue type. In addition, the segmentation method has the potential applying on other medical imaging, such as intravascular ultrasound (IVUS), computed tomography (CT), *etc*.

Due to the complicated structure and irregular geometry of atherosclerotic plaque, it is very difficult to obtain the convergent solutions of such highly non-linear 3D FSI computational model. Applying proposed Volume Component-Fitting Method (VCFM) mesh generation method, two 3D FSI computational models and other fourteen (14) adjusted models were solved successfully. In addition, VCFM will be applicable for many other computational models which are critical with mesh.

Determination of material properties of plaque is another important issue for MRI-based computational model. Compared with the most common used approach by measuring the pressure and outer diameter, using MRI to measure the pressurized inner diameter will minimize the trauma and avoid the effects from the irregular shape of the outer boundary and connective tissues. To our knowledge, this is the first attempt to quantify vessel mechanical properties for human carotid arteries using MRI data obtained under *in vitro* pressurized conditions and Least Squares Approximation Method. The procedure has the potential to be implemented under *in vivo* condition for non-invasive measurement of material properties and assessment of plaque vulnerabilities.

Under physiological condition (*in vivo* state), the plaque was tethered by the surrounded tissue and pressurized by the blood pressure. That is, the segmented contours obtained from *in vivo* MRI data undergo axial stretch and pressurization and cannot be directly used as the starting geometry. With this consideration, shrink-stretch process was proposed to achieve the start shape for the computational models. Both 2D and 3D simulations indicated that without this procedure, the deformation will be largely over-predicted and induce intolerant deviation in predicting stress and strain. In addition, to obtain the initial shrinkage rate of the plaques between loaded (*in vivo*) and unloaded (*ex vivo*) state, ten (10) *in vivo/ex vivo* MRI images of carotid atherosclerotic plaques were registered and examined. As we know, this study is the first time to quantify the shrinkage rate of human carotid atherosclerotic plaque by comparing *in vivo/ex vivo* MRI data, and discuss the error induced by ignoring the pre-shrinkage in the computational simulations.

The above contributions of this dissertation focus on improving the accuracy and reliability of 3D MRI-based FSI computational model. They are very important because a reliable model is a base of accurate mechanical analysis. The further goal of this project is to perform mechanical analysis for better understanding the mechanism of plaque rupture based on proposed computational model. In clinical diagnosis, the thickness of fibrous cap and the size of lipid core are regarded as two most important determinants of plaque rupture risk [25]. With this concern, lipid-rich core and fibrous cap thickness were chosen for the parameter investigation.

The study of the effects of lipid-rich necrotic core on structure/flow behaviors indicate that lipid nodes associated with higher stress/strain values than non-lipid nodes. Further analysis revealed that lipid nodes of plaque with prior rupture bear much higher stress/strain than non-rupture case. Both of these findings imply that high plaque stress and strain values might link to plaque rupture and lipid nodes might have the potential to be used as critical sites to assess the plaque vulnerability. To our knowledge, there is no report about investigating the different behaviors of lipid nodes between rupture and non-rupture plaques by comparing 3D *in vivo* MRI-based FSI models of ruptured and non-ruptured plaques.

The impact of lipid-cap thickness was quantified by investigating a total of ten (10) adjusted FSI models with varied lipid-cap thickness. All morphology information and modeling approaches were fixed except the cap thickness. The advantage of this approach is to eliminate the effect from other factors to the stress/strain behavior. It is observed that the stress increase exponentially with decreasing thickness. When the fibrous cap thickness is very thin, a slight decrease of cap thickness can induce a big increase in stress. It provides partly support for current diagnosis treating cap thickness as one of the most crucial factors for plaque risk analysis [25, 40, 57, 52]. With large-scale patient studies, it is possible to establish a gold standard of stress value to quantify the plaque rupture risk by combining mechanical analysis with morphologies diagnosis.

11.2 Limitations

This study focuses on the mechanical behaviors of atherosclerotic plaque seeking potential critical indicators for non-invasive risk analysis. In reality, plaque rupture is a multi-faceted process involving plaque composition, morphology, mechanical factors, blood conditions, chemical environment, lumen surface condition (inflammation), *etc*. Investigations from other channels are needed to obtain a more complete understanding of mechanisms governing the rupture process.

Though high-resolution *in vivo* MRI is capable of capturing plaque composition and morphology, the resolution is still limited, especially in catching thin cap thickness. MRI resolution limit certain has considerable effect on accuracy of computational models and predictions.

While the *in vivo* MRI-based FSI plaque models are filling a gap in the current literature, some model limitations should be acknowledged: a) the residual stress in the structure (opening angle) was not included since it is not measureable non-invasively under in vivo conditions; b) different tissue and plaque components may have different shrinkage and may affect the artery shrinkage; c) patient-specific material properties are not available due to the limit of current measurement technology; d) isotropic models were used for vessel material which could be improved by anisotropic models for improvements; e) Non-Newtonian effect was not included in the fluid model because it has been recognized that differences between Newtonian and Non-Newtonian flow models for large arteries are small and can be ignored [81].

12. Conclusion

12.1 Summary

In this dissertation, several novel methods were introduced to address some fundamental issues for 3D FSI plaque models based on Patient-specific *in vivo* MRI data. 3D computational FSI models were constructed for human carotid atherosclerotic plaques to perform mechanical image analysis and identify critical flow and stress/strain conditions which may be related to plaque rupture. The modeling techniques including automatic segmentation of plaque morphology, VCFM mesh generation method, determination of material properties, and shrink-stretch process were developed in this dissertation. The effects of material properties and shrink-stretch process on structure stress/strain distributions have been quantified. Two 3D computational models for rupture and non rupture plaques were reconstructed to investigate the effects from lipid-rich necrotic core on structure/flow behaviors. The results indicate that lipid nodes associated with higher stress/strain values than non-lipid nodes. The stress/strain values were found to be higher in ruptured plaque than non-ruptured case. Ten (10) adjusted FSI models were constructed to investigate and quantify the impact of lipid-cap thickness. The following results were obtained: 1) thin lipid-cap area has high stress/strain concentration; 2) the lipid-cap thickness has a negative correlation with stress and strain, respectively, and a positive relationship with flow shear stress; 3) when plaque cap is thin, a slight decrease of cap thickness cause a significance increase of stress. Therefore, high stress/strain concentrations and thin lipid-cap thickness might be critical indicators for plaque vulnerability assessment.

12.2 Conclusion

The methods developed in these dissertations for computational modeling will fill a gap in current literature and may significantly improve the accuracy and reliability of 3D FSI computational models. The observations from this research of the effect of lipid nodes and cap thickness on structure/flow behaviors will lead to a better understanding of plaque progression and rupture mechanisms. With sufficient validation, these results may lead to early prediction of possible plaque ruptures.

The proposed MRI-based 3D multi-component computational modeling process integrates mechanical factors with plaque morphologies, blood pressure and vessel mechanical properties may provide more accurate assessment and predictions for possible plaque rupture risk. The modeling process and methods could be applicable to many other similar real life biological applications.

12.3 Future Work

The research presented here is a starting step to combine computational modeling and mechanical analysis with MRI techniques, pathological analysis to assess vulnerable carotid atherosclerotic plaques. Future investigations and effort include the following:

1) Improvement of the accuracy and reliability of the FSI models, by considering the anisotropic material properties of plaque tissues, different shrinkage rate for different components, *etc*.
2) Investigation of the effects of the size of lipid core, and the effects of other non-lipid components, such as calcification, hemorrhage, ulcer, *etc*., and its cap thickness.
3) Identification of the correlations between critical flow and stress/strain conditions and plaque vulnerability, and establishing quantitative risk indicators of plaque rupture with large scale studies.

4) Quantification of the gold standards of these indicators for plaque vulnerability assessment.

With future improvements and validations from large scale patient studies, the obtained quantitative risk indicators may be useful parameters for clinical diagnosis to better assess plaque vulnerability, make predictions with better accuracy, and take actions in time to prevent the actual plaque rupture from happening.

References

1. American Heart Association. Heart Disease and Stroke Statistics – 2008 Update. Dallas, Tex. American Heart Association; 2008.

2. American Heart Association. Atherosclerosis. 2008: copyright 2006, American Heart Association, Inc.; Retrieved March 2008 from the web site: http://www.americanheart.org/presenter.jhtml?identifier=228.

3. Bathe KJ, Finite element procedures. Prentice Hall, Englewood Cliffs, New Jersey, 1996.

4. Bathe KJ, Theory and Modeling Guide, Vol I: ADINA; Vol II: ADINA-F, ADINA R&D, Inc., Watertown, MA, 2002.

5. Bathe KJ, Wilson EL, Numerical methods in finite element analysis. Prentice-Hall Inc., Englewood Cliffs, N.J., 1976.

6. Bathe KJ, ZHANG H, Wang MH, Finite element analysis of incompressible and compressible fluid flows with free surfaces and structural interactions, Comput Struct, 1995; 56(2-3):193-213.

7. Bathe M, Kamm RD, A fluid--structure interactions finite element analysis of pulsatile blood flow through a compliant stenotic artery, J Biomech Eng, 1999; 121(4):361-9.

8. Box FM, Van Der Geest RJ, Rutten MC, Reiber JH. The influence of flow, vessel diameter, and non-newtonian blood viscosity on the wall shear stress in a carotid bifurcation model for unsteady flow, Invest Radiol, 2005; 40(5):277-294.

9. Burke AP, Farb A, Malcom GT, Liang YH, Smialek JE, Virmani R, Plaque Rupture and Sudden Death Related to Exertion in Men with Coronary Artery Disease. JAMA, 1999; 281:921-926.

10. Carey GF, Oden JT, Finite Elements: Fluid Mechanics, the Texas Finite Element Series, Vol. VI, Prentice-Hall, Englewood Cliffs, New Jersey, 1986.

11. Cullen P, Baetta R, Bellosta S, Bernini F, Chinetti G, Cignarella A, Eckardstein AV, Exley A, Goddard M, Hofker M, Hurt-Camejo E, Kanters E, Kovanen P, Lorkowski S, McPheat W, Pentikäinen M, Rauterberg J, Ritchie A, Staels B, Weitkamp B, Menno de Winther for the MAFAPS Consortium, Rupture of the atherosclerotic plaque: does a good animal model exists? Arterioscler Thromb Vasc Biol, 2003; 23:535-542.

12. Davies MJ, Thomas AC, Plaque fissuring-the cause of acute myocardial infarction, sudden ischemic death, and crecendo angina. Br Heart J, 1985; 53:363-373.

13. Estes JM, Quist WC, Lo Gerfo FW, Costello P, Noninvasive characterization of plaque morphology using helical computed tomography, J Cardiothorac Surg (Torino) 1998; 39: 527-34.

14. Fayad ZA, Fuster V, Clinical iImaging of the high-risk or vulnerable atherosclerotic plaque, Circ Res, 2001; 89:305-16.

15. Falk E, Why do plaques rupture? Circulation, 1992; 86:(Supplement III): 30-42.

16. Frayne R, Steinman DA, Ethier CR, Rutt BK, Accuracy of MR phase contrast velocity measurements for unsteady flow, J Magn Reson Imaging, 1995; 5: 428-431.

17. Fung YC, In what principle governs the stress distribution in living organs (Biomechanics in China, Japan and USA. Science, Beijing, China), pp.1-13, 1983.

18. Fung Y.C. In Biomechanics: Mechanical Properties of Living Tissues, Springer-Verlag New York, Inc., New York, NY, 1993.
19. Fung YC. Biomechanics: Motion, Flow, Stress, and Growth. 2nd ed, Springer-Verlag New York, Inc., New York, NY, 1990.
20. Fung YC, Biomechanics: Mechanical Properties Living Tissues, 2nd ed, Springer-Verlag New York, Inc., New York, NY, 1993.
21. Fung YC, Liu SQ, Changes of zero stress state of rat pulmonary arteries in hypertrophy, J Appl Physiol, 1991; 70:2455-2470.
22. Fung YC, Liu SQ, Elementary mechanics of the endothelium of blood vessels. J Biomech Eng., 1993;115:1-12.
23. Fung YC, Liu SQ, Zhou JB. Remodeling of the constitutive equation while a tissue remodels itself under stress, J Biomech Eng., 1993;115(4B):453-459.
24. Fuster V, Stein B, Ambrose JA, Badimon L, Badimon JJ, Chesebro JH. Atherosclerotic plaque rupture and thrombosis, evolving concept, Circulation, 1990; 82: Supplement II: II-47--II-59.
25. Fuster V, Assessing and modifying the vulnerable atherosclerotic plaque, Futura Publishing Company, Inc., Amonk, NY., 2002.
26. Fuster V. The Vulnerable Atherosclerotic Plaque: Understanding, Identification, and Modification AHA Monograph series, Futura Publishing company, Inc, Armonk NY, 1998.
27. Gao H, Long Q, Effects of varied lipid core volume and fibrous cap thickness on stress distribution in carotid arterial plaques, J Biomech.,2008; 41(14):3053-30599;

28. Grønholdt ML, Dalager-Pedersen S, Falk E. Coronary atherosclerosis: determinants of plaque rupture. Eur Heart J., 1998; 19:Supplement C: C24-9.

29. Han HC, Fung YC. Species dependence of the zero-stress state of aorta: pig versus rat. J Biomech Eng,1991;113 (4):446-51.

30. Holzapfel GA, Sommer G, GasserCT, Regitnig P, Determination of the layer-specific mechanical properties of human coronary arteries with non-atherosclerotic intimal thickening, and related constitutive modelling, Am J Physiol Heart Circ Physiol., 2005; 289:H2048–2058.

31. Holzapfel, GA, Stadler M, Schulze-Bause CA, A layer-specific three-dimensional model for the simulation of balloon angioplasty using Magnetic Resonance Imaging and mechanical testing, Ann Biomed Eng, 2002; 30(6):753-767.

32. Huang X, Yang C, Yuan C, Liu F, Canton G, Zheng J, Woodard PK, Sicard GA, Tang D, Patient-Specific artery shrinkage and 3D zero-stress state in multi-component 3D FSI models for carotid atherosclerotic plaques based on in vivo MRI data, MCB, 2009; 6(2): 121-134.

33. Huang X, Yang C, Zheng J, Woodard PK, Tang D, Quantifying vessel material properties using MRI under pressurized condition and MRI-based FSI models for blood flow in diseased human arteries, J Biomech, 2006; 39: Supp 1, 439.

34. Huang X, Yang C, Zheng J, Woodard PK, Tang D, Quantifying vessel material properties using MRI under pressurized condition and MRI-based FSI models for blood flow in diseased human arteries. Proceedings of the 5th World Congress of Biomechanics, 595-599, 2006.

35. Huang X, Yang C, Zheng J, Woodard PK, Tang D. Automated Segmentation of Atherosclerotic Plaque Using Bayes Classifier for Multi-Contrast In Vivo and Ex Vivo MR Images. ICCES: International Conferences on Computational & Experimental Engineering & Sciences (online journal), 2007; 1(1): 29-34.

36. Kaazempur-Mofrad MR, Isasi AG, Younis HF, Chan RC, Hinton DP, Sukhova G, Lamuraglia GM, Lee RT, Kamm RD, Characterization of the Atherosclerotic Carotid Bifurcation Using MRI, Finite Element Modeling, and Histology, Ann Biomed Eng, 2004; 32 (7): 932–946.

37. Kerwin W, Hooker A, Spilker M, Vicini P, Ferguson M, Hatsukami T, Yuan C, Quantitative magnetic resonance imaging analysis of neovasculature volume in carotid atherosclerotic plaque. Circulation, 2003; 107(6):851-6.

38. Kobayashi S, Tang D, Ku DN, Development of an echographic phantom to study pathologic wall mechanics, Proceedings of International New Cardiovascular Technologies Congress (http://www.inctc.org/), 2004.

39. Kobayashi S, Tsunoda D, Fukuzawa Y, Morikawa H, Tang D, Ku DN, Flow and compression in arterial models of stenosis with lipid core, Proceedings of 2003 ASME Summer Bioengineering Conference, pp497-498, 2003,.

40. Kolodgie FD, Burke AP, Farb A, Gold HK, Yuan J, Narula J, Finn AV, Virmani R, The thin-cap fibroatheroma: a type of vulnerable plaque: the major precursor lesion to acute coronary syndromes, Curr Opin Cardiol, 2001; 16:285-292.

41. Ku DN, Kobayashi S, Mijovic B, Tang D, Compression from Dynamic Pressure Conditions in Models of Arterial Disease, Ann Biomed Eng, 1997; 25: Supplement 1.

42. Kuncheva LI, Combining Pattern Classifiers: Methods and Algorithms, J Wiley, NJ, 2004.

43. Li ZY, Howarth S, Trivedi RA, U-King-Im JM, Graves MJ, Brown A, Wang L, Gillard JH, Stress analysis of carotid plaque rupture based on in vivo high resolution MRI, J Biomech., 2006;39(14):2611-22

44. Long Q, Xu XY, Ariff B, Thom SA, Hughes AD, Stanton AV, Reconstruction of blood flow patterns in a human carotid bifurcation: a combined CFD and MRI study, J Magn Reson Imaging., 2000;11(3):299-311.

45. Lynch DR, Numerical Partial Differential Equations for Environmental Scientists and Engineers: a First Practical Course, Springer, New York, 2005.

46. Martin AJ, Gotlieb AI, Henkelman RV. Hight-resolution MR imaing of human arteries. J Magn Reson Imaging, 1995;5:93-100.

47. McDonald DA, Blood Flow in Arteries. 2nd, London: Edward Arnold, 1974.

48. Morgan GW, Kiely JP, Wave propagation in a viscous liquid contained in a flexible tube, J Acoust Soc Amer, 1954; 26: 323-28.

49. Naghavi M, Libby P, Falk E, Casscells SW, Litovsky S, Rumberger J, Badimon JJ, Stefanadis C, Moreno P, Pasterkamp G, Fayad Z, Stone PH, Waxman S, Raggi P, Madjid M, Zarrabi A, Burke A, Yuan C, Fitzgerald PJ, Siscovick DS, de Korte CL, Aikawa M, Juhani Airaksinen KE, Assmann G, Becker CR, Chesebro JH, Farb A, Galis ZS, Jackson C, Jang IK, Koenig W, Lodder RA, March K, Demirovic J, Navab M, Priori SG, Rekhter MD, Bahr R, Grundy SM, Mehran R, Colombo A, Boerwinkle E, Ballantyne C, Insull W Jr, Schwartz RS, Vogel R, Serruys PW, Hansson GK, Faxon DP, Kaul S, Drexler H, Greenland P, Muller JE, Virmani R, Ridker PM, Zipes DP, Shah PK, Willerson JT. From vulnerable plaque to vulnerable patient:

a call for new definitions and risk assessment strategies: Part I. Circulation. 2003; 108(14):1664-72.

50. National Library of Medicine. Carotid artery anatomy. 2006: Copyright 1997-2008, A.D.A.M., Inc.; Retrieved March 2008 from the website: http://www.nlm.nih.gov/medlineplus/ency/presentations/100124_1.htm.

51. Oliver TB, Lammie GA, Wright AR, Atherosclerotic plaque at the carotid bifurcation: CT angiographic appearance with histopathologic correlation. AJNR Am J Neuroradiol, 1999; 20: 897-901.

52. Redgrave JN, Gallagher P, Lovett JK, Rothwell PM, Critical cap thickness and rupture in symptomatic carotid plaques: the oxford plaque study, Stroke, 2008; 39(6):1722-9.

53. Russ JC, The Image Processing Handbook, 2nd ed, CRC Press, Inc., Boca Raton, FL, 1995.

54. Saam T, Ferguson MS, Yarnykh VL, Takaya N, Xu D, Polissar NL, Hatsukami TS, Yuan C. Quantitative evaluation of carotid plaque composition by in vivo MRI. Arterioscler Thromb Vasc Biol, 2005; 25(1):234-239.

55. Serfaty JM, Chaabane L, Tabib A, Chevallier JM, Briguet A, Douek PC, Atherosclerotic plaques: classification and characterization with T2-weighted high-spatial-resolution MR imaging-an in vitro study, Radiology, 2001; 219:403-10.

56. Shinnar M, Fallon JT, Wehrli S, Levin M, Dalmacy D, Fayad ZA, Badimon JJ, Harrington M, Harrington E, Fuster V. The diagnostic accuracy of ex vivo MRI for human atherosclerotic plaque characterization. Arterioscler Thromb Vasc Biol, 1999; 19: 2756-2761.

57. Stary HC, Chandler AB, Dinsmore MD, et al., Definitions of advanced types of atherosclerostic lesions and the histological classification of atherosclerosis. A report from

the Committee on Vascular Lesions of the Council on Arteriosclerosis, AHA, Circulation, 1995; 92:1355-1374.

58. Steinman DA. Image-based computational fluid dynamics modeling in realistic arterial geometries. Ann Biomed Eng 2002; 30(4):483-97.
59. Steinman DA, Thomas JB, Ladak HM, Milner JS, Rutt BK, Spence JD, Reconstruction of carotid bifurcation hemodynamics and wall thickness using computational fluid dynamics and MRI, Magn Reson Med, 2002; 47(1):149-59.
60. Tang D, Yang C, Huang Y, Ku DN, Wall Stress and Strain Analysis Using a 3-D Thick-Wall Model with Fluid-Structure Interactions for Blood Flow in Carotid Arteries with Stenoses, Comput Struct, 1999; 72:341-356.
61. Tang D, Yang C, Kobayashi S, Ku DN, Experiment-Based Numerical Simulation of Unsteady Viscous Flow in Stenotic Collapsible Tubes, Appl Numer Math, 2001; 36:299-320.
62. Tang D, Yang C, Kobayashi S, Ku DN, Quantification of controlling factor effects on flow and stress distribution in stenotic arteries with lipid cores, Proceedings of 2003 International Mechanical Engineering Congress & Exposition, IMECE2003-41113, 2003.
63. Tang D, Yang C, Kobayashi S, Ku DN, Effect of a lipid pool on stress/strain distributions in stenotic arteries: 3D FSI models. J. Biomechanical Engineering, 2004; 126:363-370.
64. Tang D, Yang C, Ku DN, A Boundary Iteration Method for Viscous Flow in Stenotic Collapsible Tubes Subjected to an External Pressure, Unsteady Flow, Proceedings of the Fourth U.S. National Congress on Computational Mechanics, pp. 403, 1997.
65. Tang D, Yang C, Ku DN, Flow in Stenotic Collapsible Tubes: Axisymmetric and Preliminary 3-D Results, Ann Biomed Eng, 1997; 25: Supplement 1, 1997

66. Tang, D, Yang C, Ku DN, A 3-D thin-wall model with fluid-structure interactions for blood flow in carotid arteries with symmetric and asymmetric stenoses, Comput Struct, 1999; 72:357-377.

67. Tang D, Yang C, Zheng J, Woodard PK, Saffitz JE, Petruccelli JD, Sicard GA, Yuan C, Local maximal stress hypothesis and computational plaque vulnerability index for atherosclerotic plaque assessment. Ann Biomed Eng, 2005; 33(12):1789-801.

68. Tang D, Yang C, Zheng J, Woodard PK, Saffitz JE, Sicard GA, Pilgram TK, Yuan C, Sensitivity Analysis of 3D MRI-Based Models for Atherosclerotic Plaques, Proceedings of The IASTED International Conference on Biomechanics, Editor: M. H. Hamza, ACTA Press, Anaheim, pp. 97-100, 2004.

69. Tang D, Yang C, Zheng J, Woodard PK, Saffitz JE, Sicard GA, Pilgram TK, Yuan C. Quantifying effects of plaque structure and material properties on stress distributions in human atherosclerotic plaques using 3D FSI models. J Biomech Eng, 2005; 127(7):1185-94.

70. Tang D, Yang C, Zheng J, Woodard PK, Sicard GA, Saffitz JE, and Yuan C, 3D MRI-Based Multi-Component FSI Models for Atherosclerotic Plaques a 3-D FSI model, Ann Biomed Eng, 2004; 32(7): 947-960.

71. Tang D, Yang C, Zheng J, Vito RP, Effects of stenosis asymmetry on blood flow and artery compression: a three-dimensional fluid-structure interaction model. Ann Biomed Eng, 2003; 31:1182-1193.

72. Tang D, Yang C, Walker HF, Kobayashi S, Zheng J, Ku DN, 2-D and 3-D multi-physics models for flow and nonlinear stress/strain analysis of stenotic arteries with lipid cores, Computational Fluid and Solid Mechanics, Elsevier, New York, 2003; 2: 1829-1832.

73. Vaishnav RN, Vossoughi J, Estimation of residual strains in aortic segments. In: Hall, C.W., Editor, 1983. Biomedical Engineering II. Recent Developments, Pergamon Press, New York, pp. 330–333, 1983.

74. Waksman R, Serruys, PW, Handbook of the vulnerable plaque, Taylor & Francis Group, Boca Raton, FL, 2004.

75. Womersley JR, Method for the calculation of velocity, rate of flow and viscous drag in arteries when the pressure gradient is known, J Physiol, 1955; 127:553-563.

76. Womersley JR, Oscillatory motion of a viscous liquid in a thin-walled elastic tube. I: The linear approximation for long waves. Philos Mag, 1955; 46:199-219.

77. Womersley JR, Oscillatory flow in arteries: the constrained elastic tube as a model of arterial flow and pulse transmission. Phys Med Biol, 1957; 2:178-87.

78. Womersley JR, The mathematical analysis of the arterial circulation in a state of oscillatory motion. Wright Air development Center, Technical Report WADC-TR56-614, 1957.

79. Xie JP, Liu SQ, Yang RF, Fung YC, The zero-stress state of rat veins and vena cava, J Biomech Eng, 1991; 113: 36-41.

80. Yang C, Xueying Huang, Jie Zheng, Pamela K. Woodard, and Dalin Tang. Quantifying vessel material properties using MRI under pressurized condition and MRI-based FSI mechanical analysis for human atherosclerotic plaques. Proceedings of ASME International Mechanical Engineering Congress and Exposition, 2006-13938, p.1-8, 2006.

81. Yang C, Tang D, Yuan C, Hatsukami TS, Zheng J, Woodard PK, In Vivo/Ex Vivo MRI-Based 3D Non-Newtonian FSI Models for Human Atherosclerotic Plaques Compared with Fluid/Wall-Only Models, Comput Model Eng Sci, 2007; 19(3): 233-245.

82. Younis HF, Kaazempur-Mofrad MR, Chan RC, Isasi AG, Hinton DP, Chau AH, Kim LA, Kamm RD, Hemodynamics and wall mechanics in human carotid bifurcation and its consequences for atherogenesis: investigation of inter-individual variation. Biomech Model Mechanobiol, 2004; 3(1):17-32

83. Yuan C, Hatsukami TS, Obrien KD, High-Resolution magnetic resonance imaging of normal and atherosclerotic human coronary arteries ex vivo: discrimination of plaque tissue components, J Investig Med, 2001; 49:491-499.

84. Yuan C, Kerwin WS, Ferguson MS, Polissar N, Zhang SX, Cai JM, Hatsukami TS, Contrast enhanced high resolution MRI for atherosclerotic carotid artery tissue characterization. J Magn Reson Imaging, 2002; 15:62-67.

85. Yuan C, Mitsumori LM, Beach KW, Maravilla KR, Special review Carotid atherosclerotic plaque: noninvasive MR characterization and identification of vulnerable lesions, Radiology, 2001; 221:285-99.

86. Yuan C, Mitsumori LM, Ferguson MS, Polissar NL, Echelard DE, Ortiz G, Small R, Davies JW, Kerwin WS, and Hatsukami TS. In vivo accuracy of multispectral MR imaging for identifying lipid-rich necrotic cores and intraplaque hemorrhage in advanced human carotid plaques, Circulation, 2001; 104:2051-2056.

87. Yuan C, Petty C, O’Brien KD, Hatsukami TS, Eary JF, Brown BG. In vitro and in situ magnetic resonance imaging signal features of atherosclerotic plaque-associated lipids. Arterioscler Thromb Vasc Biol, 1997; 17:1496-1503.

88. Yuan C, Tsuruda JS, Beach KN, Hayes CE, Ferguson MS, Alpers CE, Foo TK, Strandness DE, Techniques for high-resolution MR imaging of atherosclerotic plaque, J Magn Reson Imaging, 1994; 4:43-49.

89. Zhao SZ, Ariff B, Long Q, Hughes AD, Thom SA, Stanton AV, Xu XY, Inter-individual variations in wall shear stress and mechanical stress distributions at the carotid artery bifurcation of healthy humans, J Biomech, 2002; 35(10):1367-1377.